CR-sent
9-26-88

college of engineering

**THE UNIVERSITY OF TENNESSEE
KNOXVILLE**

INSTRUCTION
RESEARCH
SERVICE

*TOWARD EXCELLENCE IN
ENGINEERING EDUCATION, RESEARCH,
AND PUBLIC SERVICE!*

111793

U.S. Department of Justice
National Institute of Justice

This document has been reproduced exactly as received from the
person or organization originating it. Points of view or opinions stated
in this document are those of the authors and do not necessarily
represent the official position or policies of the National Institute of
Justice.

Permission to reproduce this copyrighted material has been
granted by
<u>   College of Engineering/University
  of Tennessee/Knoxville   </u>

to the National Criminal Justice Reference Service (NCJRS).

Further reproduction outside of the NCJRS system requires permis-
sion of the copyright owner.

ULTRASONIC DETECTION OF CONCEALED HANDGUNS

Interim Report – Phase II/2

May 1987

ULTRASONIC DETECTION OF CONCEALED HANDGUNS

Phase II/2: Proof of Principle of a Concealed Handgun Ultrasonic Detection System

Edited by:

Thomas Moriarty

University of Tennessee

310 Perkins Hall

Knoxville, TN 37996-2030

May 1987

Interim Report - Phase II/2

JANUARY 1986 - FEBRUARY 1987

ABSTRACT

In this research program the feasibility of using ultrasound to detect concealed handguns has been demonstrated (Phase I) and the development of an Ultrasonic Handgun Detection System has begun (Phase II/1).

In Phase II/2 the development of the detection system was continued.

The particular ultrasonic technique used is called the Modal Excitation Technique (MET). This technique uses ultrasound to excite the natural modes of vibration of a target object. When the target vibrates, it gives off a sound made-up of the Natural Frequencies of vibration of the target object. The set of Natural Frequencies of an object is a distinctive 'signature' of the object; this 'signature' can be used to discriminate between different types of objects.

In Phase I of this research program, the set of Natural Frequencies (the 'signature') of eight handguns and some nongun objects commonly carried about the body were experimentally determined. It was shown that the 'signature' of the handguns could be distinguished from the 'signature' of the nonguns.

In Phase II/1, the development of electronic units for transmitting and receiving airborne ultrasound relevant to handgun detection was begun and preliminary ultrasonic systems were tested.

In Phase II/2, the development of a FIeld Test Unit was continued, a Demonstration Unit was designed and built, and the biohazards of airborne ultrasound were investigated.

On the basis of the progress towards development of a Field Test Unit, the success of the Demonstration Unit, and the benign nature of the ultrasound used by the system, it is recommended that further work be done in a Phase III effort to complete the development of The Field Test Unit and begin field testing.

PREFACE

This report was prepared by the Engineering Science and Mechanics, Electrical Engineering, Audiology and Speech Pathology, and Zoology Departments, University of Tennessee, 310 Perkins Hall, Knoxville, TN 37996-2030, under Award number 83-IJ-CX-0052 for the National Institute of Justice, U.S. Department of Justice, Washington, D.C. 20531.

This report summarizes the work done between January 1986 and February 1987, Phase II/2 - Proof of Principle of a Concealed Handgun Ultrasonic Detection System.

The NIJ Program Monitor for this research program was Joseph T. Kochanski, Acting Director, CCCR.

LIST OF FIGURES

LIST OF FIGURES

LIST OF FIGURES

LIST OF FIGURES

LIST OF FIGURES

LIST OF TABLES

TABLE OF CONTENTS

0.0 INTRODUCTION

For crowd control and other situations where it is not practical to have had prior screening of all individuals at the scene, the problem of detecting concealed handguns is as yet unsolved. Even in situations where prior screening is possible, such as at airports where passengers walk through electromagnetic portals, that technology is an imperfect solution for detecting concealed handguns because it does not detect the presence of handguns but rather the presence of certain metals above a certain amount; it generates many false positives and, more importantly, some false negatives because it does not detect some mateials that are used to make handguns.

This research program is applying the Modal Excitation Technique (MET) to develop a concealed handgun detection system. For this program MET uses airborne ultrasound to excite the natural modes of vibration of handguns. All solid objects have natural modes of vibration; the frequencies at which these modes vibrate are called Natural Frequencies. When an object is excited it vibrates at its Natural Frequencies which are characteristic of the geometry and material of the object. The set of Natural Frequencies of an object is a distinctive signature of the object. A tuning fork is purposely designed to have only one dominant Natural Frequency. When the tuning fork is excited only one Natural Frequency is heard, a pure tone. A bell, on the other hand, is usually designed to have many Natural Frequencies. When the bell is excited, the sound that is heard is a combination of many Natural Frequencies (many pure tones). MET listens for the set of Natural Frequencies emitted by an excited object and from these frequencies determines whether or not the object is a handgun.

The results of the first two years of this research program: Phase I: Feasibility Study of Ultrasonic Detection of Handguns and Phase II/1: Development of Ultrasonic Handgun Detection System (Year One), are documented in ULTRASONIC DETECTION OF CONCEALED HANDGUNS, Interim Report - Phase I and II/1, March 1986.

1

This Interim Report covers Phase II/2 - Proof of Principle of Concealed Handgun Ultrasonic Detection System. This report is divided essentially into three parts: Part 1 - Field Test Unit - which discusses progress made towards developing a detection system of field test quality, Part 2 - Demonstration Unit - which discusses the design and implementation of a demonstration unit that excited and automatically detected four specific Natural Frequencies among three known handguns, and Part 3 - Biohazards of Airborne Ultrasound - which discusses the results of a literature search on the topic and the experimental results on three animal models. The final chapter of the report is 4.0 CONCLUSIONS AND RECOMMENDATIONS.

Part 1 FIELD TEST UNIT

Written By:

T. F. Moriarty[1]
J. V. Sherrill[2]

[1] Research Professor, Engineering Science and Mechanics Department, University of Tennessee, Knoxville
[2] Research Assistant Professor, Engineering Science and Mechanics Department, University of Tennessee, Knoxville

3

1.0 Development of the Field Test Unit - An Overview (Moriarty)

Two general concerns about the development and deployment of a Field Test Unit that uses ultrasound to find concealed handguns are: *Is there some fundamental physical reason why such a unit could not be built?*, and, *Even if such a unit could be built, could not the ultrasound used by the system represent a biohazard and therefore deployment of the unit would not be allowed?*

Both the preliminary work reported in our last Interim Report and the successful design and implementation of the Demonstration Unit which excited and detected discrete Natural Frequencies of three handguns in less than one second (which is the subject of Part 2 of this report)) squarely address the concern about the physical possibility of building such a system.

The results of the literature search and the experimental results on three animal models (which are the subjects of Part 3 of this report) all attest to the benign nature of the ultrasound used by the detection system.

The Phase II/2 progress towards the practical implementation of an ultrasonic concealed handgun detection system of field test quality is the subject of this part of the report.

Both the Field Test Unit and the Demonstration Unit can be thought of as comprised of ten subsystems (see Fig. 1.0-1). These ten subsystems are:

> Controller,
>
> Signal Generator,
>
> Power Amplifier,
>
> Transmitter,
>
> Detection Space,
>
> Receiver,
>
> Analog Preamplifier/Filter/Amplifier,
>
> Analog to Digital Converter/Digital Signal Processor,

4

Pattern Recognition, and

Handgun Alarm.

```
                                       ┌──────────────────┐
                                       │ HANDGUN ALARM    │
                                       └──────────────────┘
                                                 ▲
                                                 │
  ┌──────────────┐                      ┌──────────────────┐
  │ CONTROLLER   │─────────┐            │ PATTERN REC.     │
  └──────────────┘         │            └──────────────────┘
          │                │                     ▲
          ▼                │                     │
  ┌──────────────────┐     │            ┌──────────────────┐
  │ SIGNAL GENERATOR │     └────────────│ ADC/DSP          │
  └──────────────────┘                  └──────────────────┘
          │                                      ▲
          ▼                                      │
  ┌────────────────────┐              ┌──────────────────────┐
  │ POWER AMPLIFIER    │              │ PREAMP/FILTER/AMP     │
  └────────────────────┘              └──────────────────────┘
          │                                      ▲
          ▼                                      │
  ┌──────────────────┐                 ┌──────────────────┐
  │ TRANSMITTER      │                 │ RECEIVER         │
  └──────────────────┘                 └──────────────────┘
          │                                      ▲
          ▼                                      │
  ┌──────────────────────┐                       │
  │ DETECTION SPACE      │───────────────────────┘
  └──────────────────────┘
```
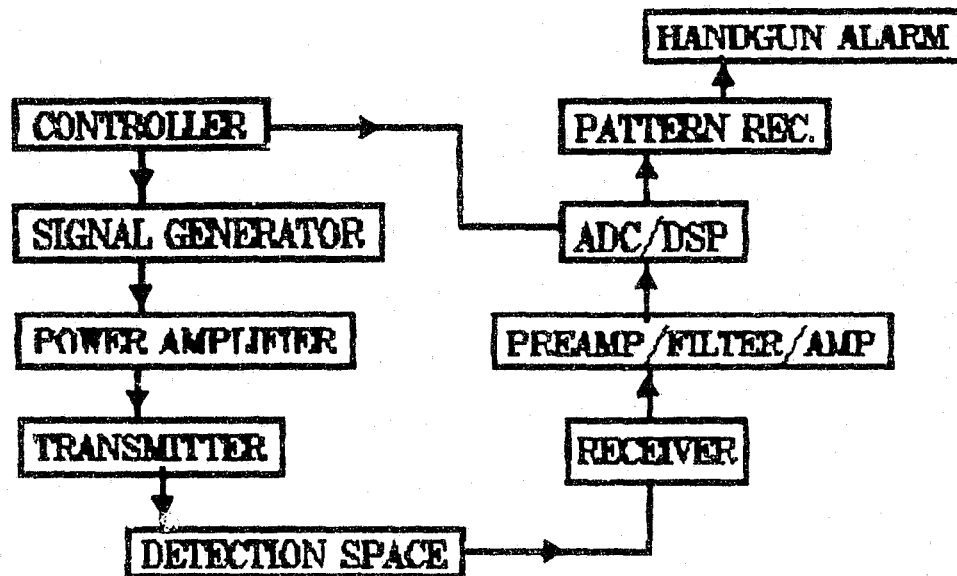
Fig. 1.0-1 Subsystems of Field Test Unit and Demonstration Unit

Chapter 1.1 – Field Test Unit Digital Electronics, describes the digital electronic subsystems in the Field Test Unit.

Two of the more important subsystems of Field Test Unit are the transducer that converts an electric signal into airborne ultrasound, the Transmitter, and the transducer that converts airborne ultrasound into an electric signal, the Receiver; Chapter 1.2 - Field Test Unit Transducers, discusses the development of these subsystems. The Power Amplifier and Preamplifier design details are strongly dependent upon the final form that the Field Test Unit transducers will take. Discussion of these subsystems is postponed to a later date.

The Handgun Alarm Subsystem design is trivial. The Handgun Alarm is connected to the Pattern Recognition Subsystem by a handgun detect signal line. When the Pattern Recognition Subsystem brings the voltage on that line high (or low, depending on the design) the Handgun Alarm activates a buzzer, a light and/or other alarm device.

This leaves one subsystem left to describe, the Detection Space. The Demonstration Unit used freestanding panels to separate the subjects being examined from the rest of the people in the room; the panels also served, to some degree, to decouple the acoustics of the Detection Space from the acoustics of the room or general vicinity as a whole. Future Field Test Units will not require a discrete subsystem to establish a detection space; the future systems will be simply aimed at the volume of interest without the need for a concrete delineation of space. For development of the first Field Test Unit; however, it was thought prudent to develop a Hallway Version of the detection system for the following reasons:

• The Hallway Version has a detection space over which significant control of the environment, including ambient sound and reflected ultrasound, can be imposed so that the detection system can be perfected first under optimum conditions, then later extended to work in less than optimum conditions.

• The Hallway Version of the detection system can be deployed to buildings in all branches of the federal government, to embassies, to airports, to convention halls, to

courts, to schools, to churches and all other class of limited access buildings where terrorism might take place, and

● Developing the Hallway Version first allows the detection system design to mature to a point where miniaturization of the design makes sense. To develop the detection system design to field test quality while trying to miniaturize the design at the same time would not be practical.

The detailed design of the Hallway is to be accomplished in Phase III: Development of Field Test Unit.

1.1 Field Test Unit Digital Electronics (Sherrill)

The digital electronic subsystems of the first Field Test Unit is based on an IBM AT compatible. The wide availability and low cost of the IBM AT compatibles, as well as the large selection of specialized boards for it, make it a logical choice for developing the digital electronic portion of the detection system. Three boards are used with the IBM AT compatible:

a specially designed digital-to-analog converter board which serves as a programmable signal generator,

a specially designed analog-to-digital converter board, and

a Definicon Systems Inc., (DSI), 780/2 board which performs the digital signal processing and pattern recognition computations.

The DSI-780/2 uses Motorola's 68020 32 bit Central Processing Unit and 68881 Floating Point Processor. Its clock speed is 16.67 MHz and it has 2 MegaBytes of Random Access Memory and uses a 32 bit version of Microsoft's Disk Operation System. This board has sufficient speed and power to perform digital signal processing and pattern recognition for the field test detection of generic handguns. The specially designed boards are described below.

The highly programmable nature of the current design for the digital electronics of the detection system make the system highly versatile which should markedly shorten development time and field test shakedown time. Once the system is operating properly in field testing, the keyboard and monitor can be unplugged, further reducing the weight and bulk of the system. Once the operation of the Hallway Version of the Detection System is perfected, the digital electronics can be redesigned to include only those features needed for normal operations; the versatile features of the current design which are needed for development and field test shakedown can be eliminated; this redesign should further reduce the cost, weight and bulk of the units that are deployed.

8

Meanwhile, the current unit can be used to develop other versions of the Detection System.

There are 3 major sections for the Digital electronics.

- The First section is the IBM PC interface. The IBM PC is responsible for the overall, non-timing critical, control of the complete detection system. A hardware/software interface was designed to link the PC with the separate detection system. This hardware consists of 96 relocatable buffered Input/Output control lines. These lines are generated by 4 INTEL 8255s (Parallel Input/Output Ports). All communications to and from the detection system are controlled by this hardware. See Figure 1.1-1.

- The Second section is the programmable signal generator used to create the transmitted airborne ultrasound. It is accurate to 1 Hz and programmable from 20 kHz to 110 kHz in 100 Hz increments. It can generate up to 512 frequencies simultaneously. Internally, it is composed of 64K of Static RAM, several address calculators, a 12 bit digital/analog converter running at 1 MHz, and the appropriate smoothing/level conversion filters. The timing of the system is controlled by a GAL20V8 (Programmable Electrically Erasable Generic Array Logic device made by LATTICE Semiconductor). See Figure 1.1-2, and 1.1-3.
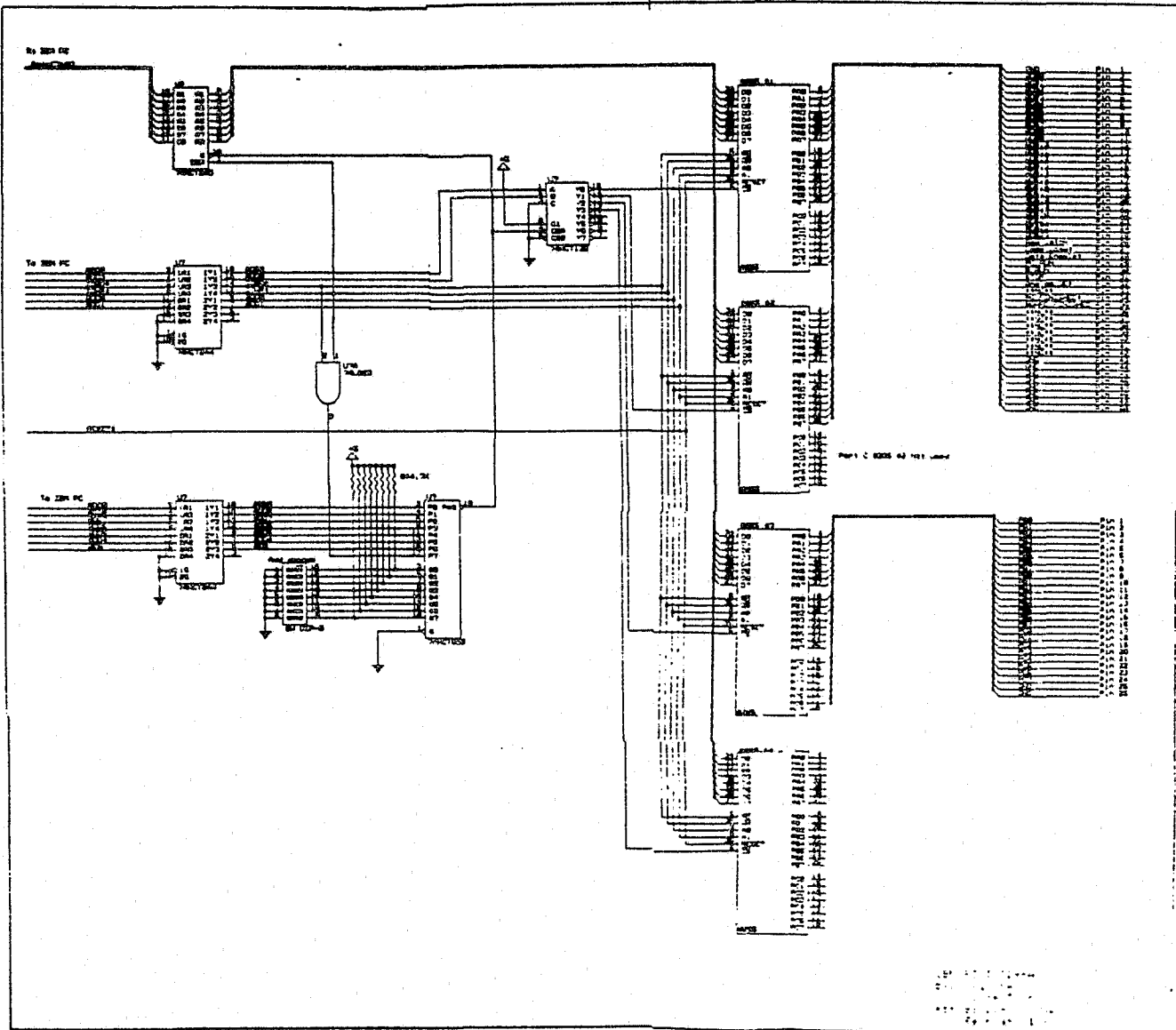
Fig. 1.1-1 IBM PC Interface

10
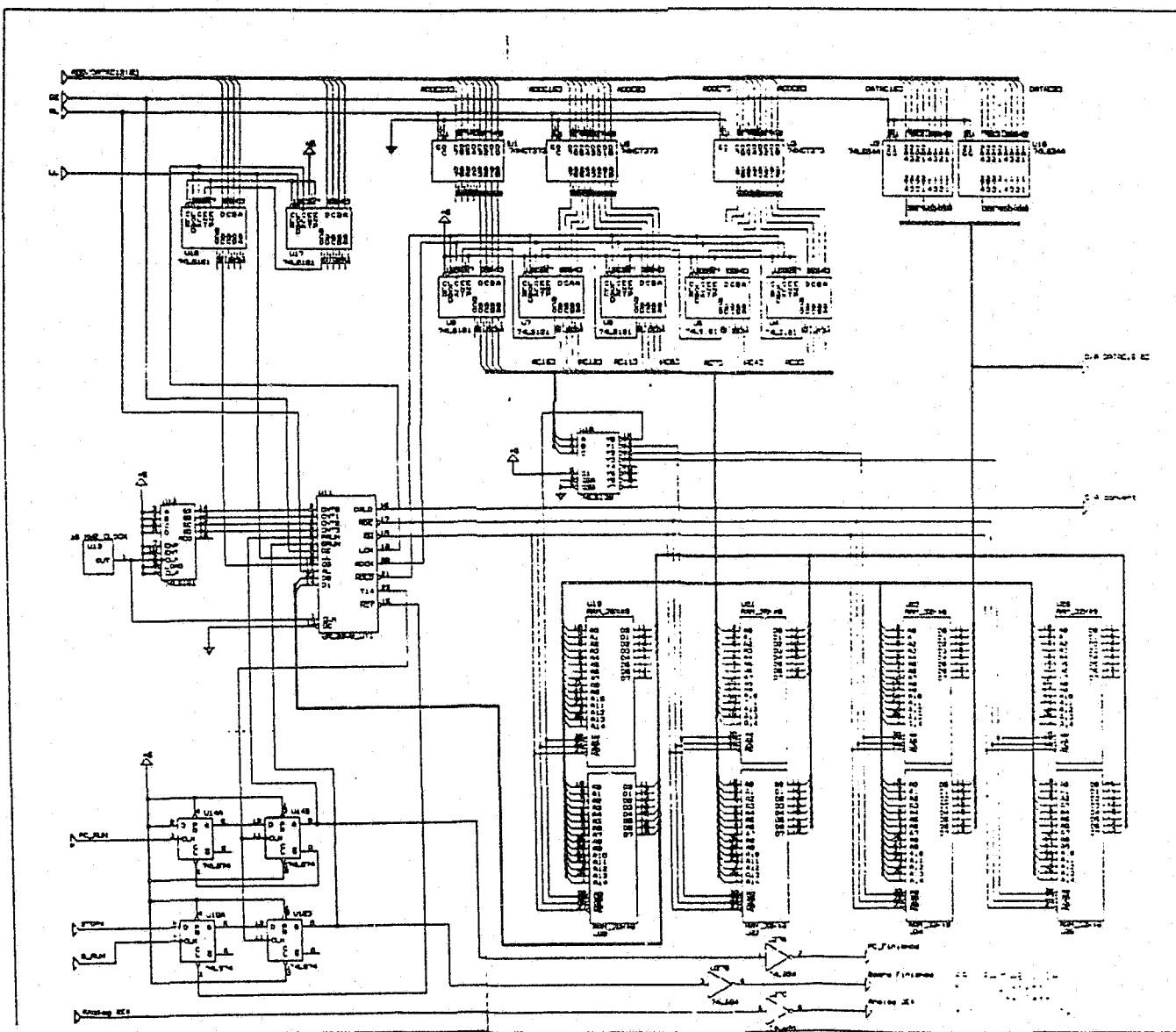
Fig. 1.1-2 Programmable Signal Generator

Fig. 1.1-3 Filter for Signal Generator

•   The Third section is the programmable Analog/Digital Converter. It is composed of 5 major parts, the Analog/Digital converter, anti-aliasing filter, timing controller, programmable delay controller, and 128K of static RAM. The 12 bit Analog/Digital converter runs at 1 MHz and stores its data in a 128K RAM buffer (used for later calculations). The Anti-Aliasing filter is used to restrict all input frequencies not in the range of interest. The delay controller is used to adjust the sample time window. The timing of the entire analog/digital converter systems is controlled by a GAL20V8. See Fig. 1.1-4.

Fig. 1.1-4 Programmable Analog/Digital Controller

14

Fig. 1.1-4 Programmable Analog/Digital Controller (Concluded)

1.2 Field Test Unit Transducers (Moriarty)

Airborne Ultrasound:

To select the appropriate technology for transmitting and receiving airborne ultrasound, it is important to understand the characteristics of the propagation of ultrasound in air for the frequency range of interest.

For propagation of a plane wave in air, the force equilibrium condition for a particle (volume element) of air in the direction perpendicular to the plane is:

$$-p, X = d\, u, tt \qquad (1)$$

where:

p is acoustic pressure,

X is coordinate in direction of propagation,

d is mass density of air,

u is displacement of air, and

t is time

If conservation of mass is combined with (1), the following differential equation for acoustic pressure results:

$$p, XX = (1/c^2)\, p, tt \qquad (2)$$

where c is the speed of sound in air.

(For more background and a discussion of the approximations incorporated in (1) and (2), see: Kinsler/Frey and others; Fundamentals of Acoustics, Third Edition, John Wiley and Sons, 1982, Chapter 5.)

The general solution to (2) is:

$$p = F_1 (t - X/c) + F_2 (t + X/c) \qquad (3)$$

where F_1 and F_2 are arbitrary functions.

For the purposes of transducer design, consider the special solution:

$$p = A \sin ((f/2n)(t - X/c)) \qquad (4)$$

where:

A is the acoustic pressure amplitude in Pascals, [Pa]

f is the frequency of the ultrasound in Hertz, [Hz]

By (1) the displacement solution corresponding to (4) is:

$$u = -A (2\pi/fdc) \quad \cos ((f/2\pi)(t - X/c)) \tag{5}$$

where u is in meters, [m].

The following terms in acoustics will now be defined in terms of the above variables.

Intensity, I, is the time averaged rate of flow of acoustic energy through a unit area normal to the direction of propagation. For plane waves:

$$I = (1/2) A^2 /dc \tag{6}$$

Intensity Level, IL, in decibels, [dB], is:

$$IL = 10 \log (I/I_0) \tag{7}$$

where I_0 is the reference intensity which, for air, is:

$$I_0 = 1.0 (-12) [W/m^2] \tag{8}$$

(A person with unimpaired hearing can just barely hear a 1000 Hertz pure tone at this intensity.)

Effective Acoustic Pressure, P_E, is:

$$P_E = A/2^{0.5} \tag{9}$$

Sound Pressure Level, SPL, in decibels, [dB], is:

$$SPL = 20 \log (P_E/P_{E_0}) \tag{10}$$

where P_{E_0} is the reference effective pressure which is equal to 2.04(-05) [Pa] for air. This pressure is often rounded off to 2.0(-05) [Pa]. Since this reference effective pressure is almost exactly equal to that corresponding to the reference intensity, essentially identical dB results are obtained when using either IL or SPL when plane waves are measured in air. For more complex sound fields IL and SPL are not identical. Since the voltage output of microphones are proportional to pressure, the acoustic

17

pressure in sound fields is readily measured; therefore, SPL is used more often to specify sound fields.

See Fig. 1.2-1 for a plot of sound pressure amplitude as a function of SPL. The equation for the curve was gotten by substituting (9) and the rounded off value for the reference effective pressure into (10) and then inverting:

$$A = 2.8284 \ 10^{((SPL - 100)/20)} \tag{11}$$

See Fig. 1.2-2 for plots of absolute displacement amplitude as a function of SPL for several frequencies of interest. These plots were obtained by noting the relation between the absolute displacement amplitude and the pressure amplitude, see (5) and (4) respectively. For the purpose of transducer design, the values for the mass density of air and the speed of sound in air were taken to be:

$$d = 1.21 \ (+00) \ [kg/m^3]$$

$$c = 3.43 \ (+02) \ [m/s]$$

which are nominal values for air at 20 degrees Celsius.

$$u = (4.2820/f) \ 10^{(SPL/20 - 7)} \tag{12}$$

Regardless of the technology used to transmit airborne ultrasound, it must be able to impart to the air the displacements corresponding to the frequencies and maximum SPL of interest. Similarly, the technology used to receive airborne ultrasound must be sensitive to the air pressures and/or displacements corresponding to the frequencies and minimum SPL of interest. These pressure/displacement requirements are important criteria for identifying appropriate technology for airborne ultrasound transducers.
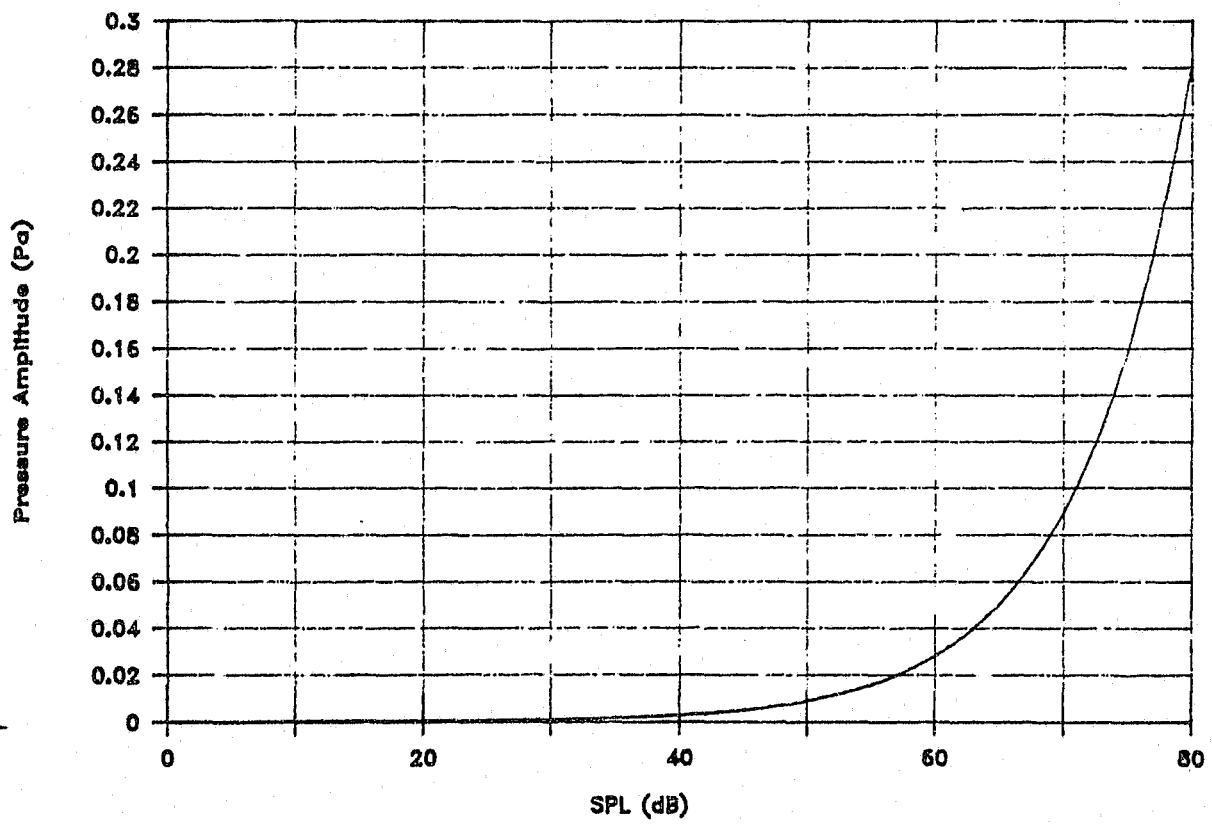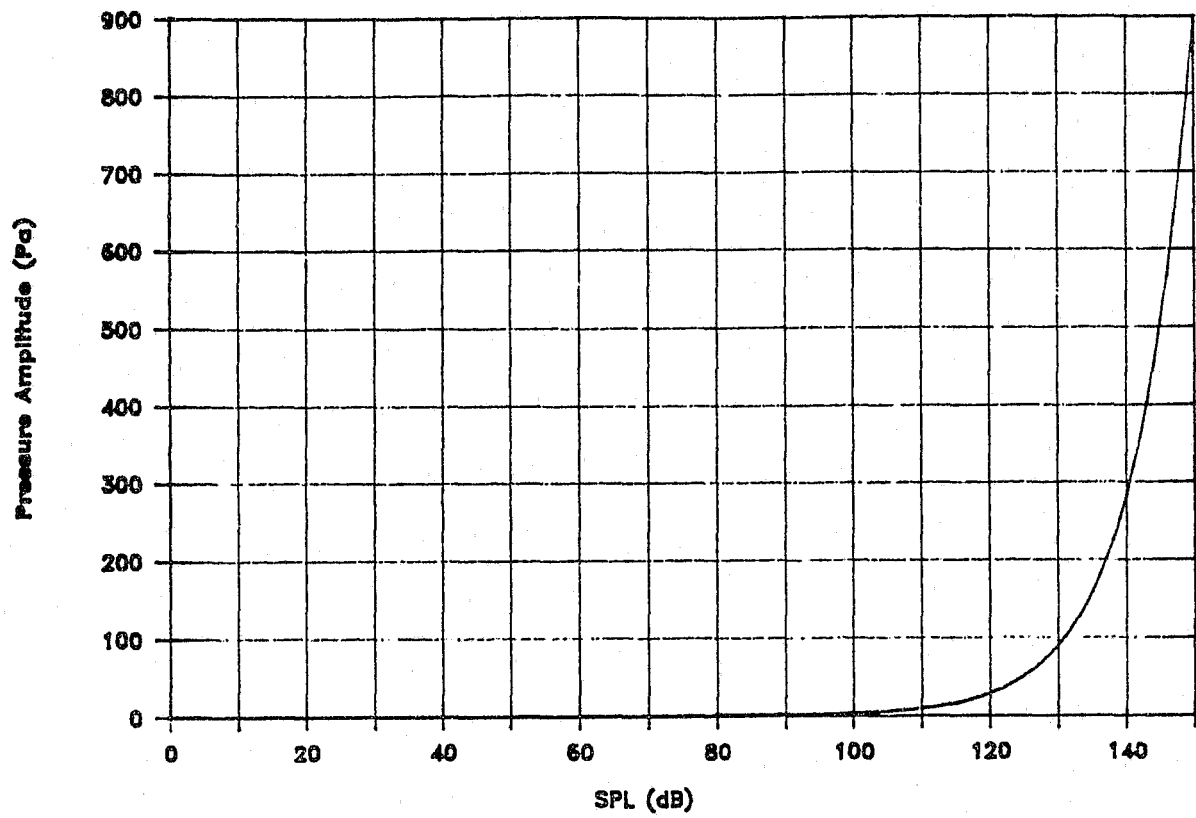
Fig. 1.2-1 Sound Pressure Amplitude Versus Sound Pressure Level
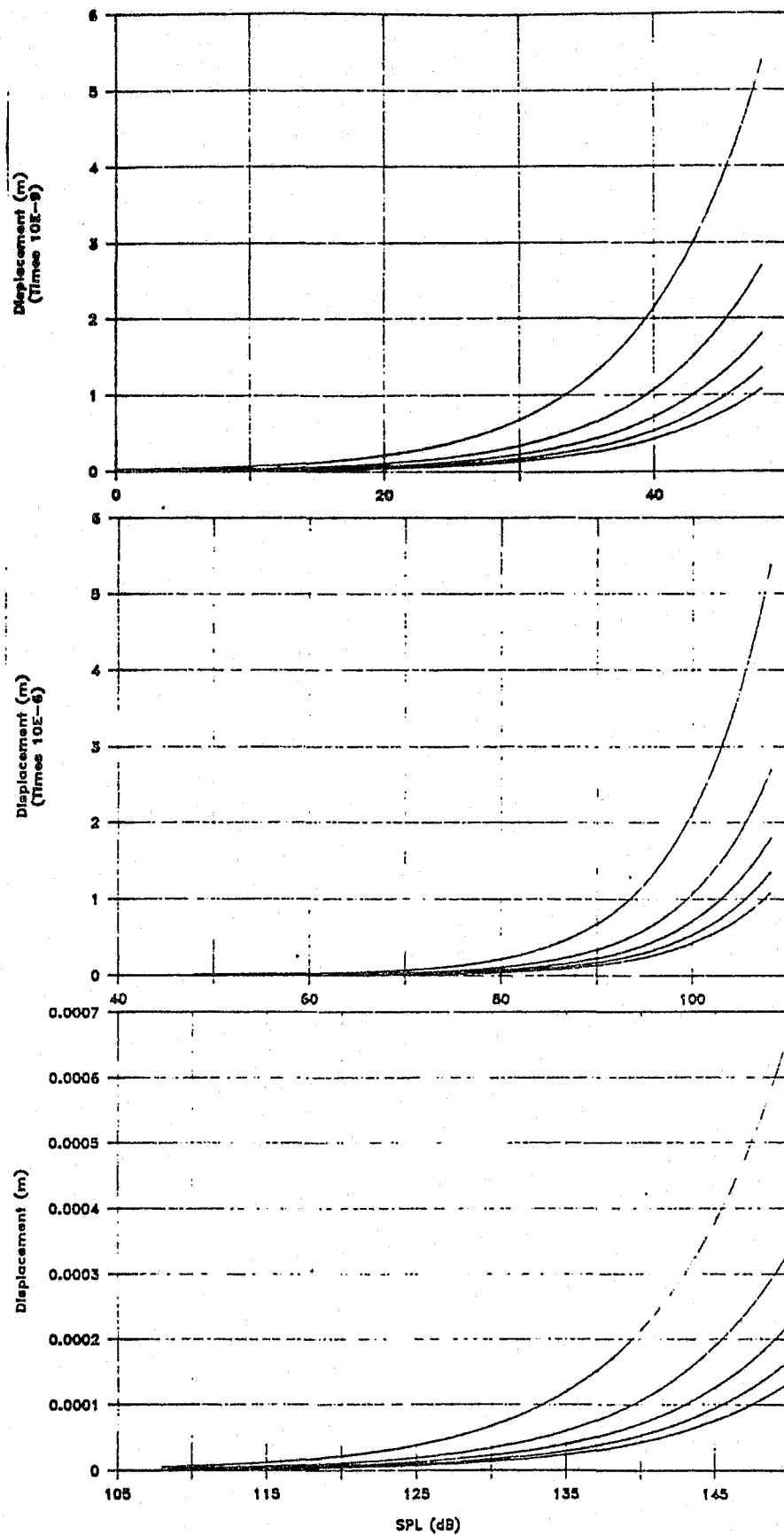
Fig. 1.2-2 Absolute Displacement Amplitude Versus Sound Pressure Level

From top to bottom in each graph, curves are for 20, 40, 60, 80, 100 kHz, respectively.

Ultrasound Transmitters:

Throughout the early phases of this project, Polaroid Solid Dielectric Ultrasonic Transducers were used to transmit ultrasound. An array of ten of these transducers was used in the Demonstration Unit described in Part Two of this report. The array generated an SPL of 120 dB at a distance of one meter from the array but for an area only 200 mm in diameter. Solid dielectric transducers have several major disadvantages which make them unusable for the Field Test Unit.

An individual Polaroid transducer cannot impart enough displacement to the air to reach the higher SPL levels by itself. Modest SPL levels can only be achieved by the superposition of outputs of arrays of these transducers; and, these modest SPL levels are in only a small volume of the detection space. The use of arrays is counter to the long range objective of a low weight, low bulk detection system.

Polaroid transducers are a capacitive load to the driving electronics whereas an ideal transducer would be a pure resistive load. This means that a special type of power amplifier has to be designed and built to efficiently drive these transducers. Part Two describes one such amplifier. The use of this type of power amplifier is also counter to the long range goal of a low weight, low bulk detection system. Further, this special amplifier requires that the frequencies that are transmitted at any one time be in relatively narrow bands; the frequency range from 25 kHz to 100 kHz is broken into fifteen bands. This represents a serious limitation on the complexity of the signal that can be transmitted by such a system.

Recognizing the limitations of the Polaroid Transducers for this application we have been exploring alternate technologies for an ultrasound transmitter. One very promising alternative is a variation on a ribbon tweeter made by Magnepan Inc., White Bear Lake, MN. The off-the-shelf version of this tweeter can be driven up to 55 kHz before there is a 3 dB decline in output; it can be driven to over 95 kHz with larger declines in output. The tweeter is a pure resistive load. The pure resistive load will

21

allow the use of off-the-shelf power amplifiers, such as a Hafler DH-500 power amplifier for development and initial field testing. Once the optimum operation of the Detection System is established and the duty cycle determined for the transmitter, a power amplifier for resistive loads specially tailored for this application can be designed, built and incorporated in the Detection System further reducing the weight and bulk of the system.

The tweeter is made of a steel channel with pairs of permanent magnets mounted on the channel in such a way that there is a 0.25 inch (6.35[mm]) gap between the magnets. An aluminum ribbon 220 mils (5.59[mm]) wide and 0.15 mils (3.81 microns) thick is suspended in the gap between the magnets. When current is sent down the ribbon in the magnetic field, a force acts on the ribbon in a direction perpendicular to both the direction of the current and the magnetic field. Variations in the current causes varitions in the force which, in turn, causes variations in the motion of the ribbon which produces ultrasound.

We are currently exploring changes of the tweeter design that will make the tweeter response flat to over 100 kHz. We are looking at alternate metals, different ribbon thickness and/or width, different magnets and/or magnet gaps.

Ultrasound Receivers:

Throughout the early phases of this project and for the Demonstration Unit, Polaroid Solid Dielectric Ultrasonic Transducers were used to receive ultrasound. This transducer is one of a family referred to as capacitor microphones. The diameter of the active area of the Polaroid Transducer is 1.45 inches (36.8 [mm]). As will be explained shortly, this diameter is much too large for it to be sensitive to ultrasound emanating from anywhere except directly in front of the transducer. For Polaroid's application of the transducer in its autoranging cameras this feature of their transducer was a plus; for our application this feature is unacceptable.

22

A capacitor microphone is essentially a rigid conducting backplane, a conducting membrane and a dielectric separating them. When the air pressure varies, the membrane deflects and changes the capacitance of the microphone. The measure of the capacitance change is a measure of the air pressure change.

Consider finding the maximum allowable diameter for a sensitive microphone with a circular membrane. Since the capacitance change is an integral over the entire area of the membrane, the diameter of the membrane must be chosen small enough so that pressure waves acting on the membrane causes deflections all of the same sign everywhere on the membrane for most instants of time. The worst case occurs at the highest frequency of interest for airborne ultrasound propagating parallel to the plane of the membrane. For the speed of sound of 343 [m/s] and the highest frequency of interest of 100 kHz, the wavelength is 3.43 [mm]. The working diameter of the membrane should be, at most, one half of the minimum wavelength of interest. Therefore, the maximum diameter of the microphone should be 1.72 [mm]. Compare that value with the 36.8 [mm] diameter of the Polaroid Transducer and you can readily see why that transducer is not acceptable for our application.

A microphone with the correct diameter also has the benefit that it will tend to filter out airborne signals obliquely hitting the membrane at frequencies higher than the maximum design frequency.

We are currently following three lines of development for obtaining sufficiently sensitive ultrasound receivers:

- using B&K microphones type 4136 and 4138 as an interim measure,
- developing a capacitor microphone more sensitive than the B&K microphones, and
- developing an optical microphone.

For more detail on the B&K microphones see:

23

Bruel & Kjaer, <u>Condenser Microphones and Microphone Preamplifiers for</u>

<u>Acoustic Measurement,</u> Data Handbook, Marlborough, MA, September, 1982.

The optical microphone uses a beam of light to monitor the minute vibrations of a thin reflective membrane. Preliminary test results are quite encouraging.

What follows are some design considerations for developing a sensitive capacitor microphone.

The microphone must not resonate (have natural frequencies) in the frequency range of interest. Since a membrane has many natural frequencies, one must make the lowest natural frequency, higher than the highest frequency of interest. From Thomson, W. T. <u>Mechanical Vibrations,</u> 2nd Ed. Prentice-Hall, Englewood Cliffs, NJ, 1962, p. 66, picking the lowest natural frequency of the membrane to be twice the highest frequency of interest guarantees that the membrane response for the highest frequency of interest will not be magnified more than 40 percent no matter how lightly damped the mic is. This magnification is significantly lower for lower frequencies of interest. For 100 kHz as the highest frequency of interest, the fundamental frequency of the membrane should be 200 kHz.

The fundamental frequency, f_F, of a circular membrane is:

$$f_F = 7.6548 \, (-01) \, (T/d)^{0.5} \, /D \qquad (1)$$

where:

T is the uniform tensile stress in the membrane,

d is the mass density of the membrane, and

D is the diameter of the membrane

Since the lowest natural frequency of the microphone is twice the highest frequency of interest, the pressure fluctuation in the frequency range of interest will be essentially a static loading on the membrane. When subjected to a static pressure, the flat circular membrane will be deflected into part of a sphere.

Let E ≡ Elastic Modulus of membrane at biaxial tension T

p ≡ strain ratio of membrane at biaxial tension T

Assume that the deformation is small so that only deflection transverse to the membrane is significant.

From force balance of a thin spherical membrane:

T_p ≡ biaxial stress due to pressure P

$$= PR/(2t) \tag{2}$$

where R is the radius of the sphere and t is the membrane thickness.

From biaxial stress-strain relation for isotropic materials:

e ≡ biaxial strain

$$= (1/E)(1 - p)T_p \tag{3}$$

From geometry of the spherically deflected membrane relative to the flat membrane:

$$e = 2(\arcsin (D/(2R))) (R/D) - 1 \tag{4}$$

Let $\quad a = \arcsin (D/(2R)) \tag{5}$

The maximum deflection, U_{MAX}, occurs at the center of the membrane:

$$U_{MAX} = R(1 - \cos(a)) \tag{6}$$

(2), (3) and (4) combine into a root finder problem for R in terms of P.

$$2(\arcsin (D/(2R))) (R/D) - 1 = (1/E)(1 - p) PR/(2t) \tag{7}$$

If the membrane of the microphone were held perpendicular to the gravitation field, the mass of the membrane would result in an equivalent pressure loading of:

$$P_{G-EG} = gdt \tag{8}$$

where:

g is the acceleration of gravity,

d is the mass density of the membrane, and

t is the thickness of the membrane.

One membrane material investigated was a Metallized Products 25 gauge Mylar (Polyester) film:

$d = 1.1153 \, (+03) \, [kg/m^3]$

$t = 7.62 \, (-06) \, [m]$

$T_{ULT} \equiv \text{Ultimate Stress} = 8.076 \, (+07) \, [Pa]$

If the biaxial stress is taken to be a half of the ultimate stress for the material:

$T = 4.0 \, (+07) \, [Pa]$

Then substituting T and d into (1) with f_F equal to 200 kHz yields a maximum membrane diameter of 7.25(-04)[m].

Part 2 DEMONSTRATION UNIT

Written By:

J. M. Rochelle*
T. V. Blalock*
R. B. Bodenheimer*
E. J. Kennedy*
D. Castillo**
A. B. Shore**
D. L. Senn**
P. Stultz**
J. W. Young**

2.0   Conceptual System Design (Rochelle)

2.1   System Controller (Bodenheimer/Stultz/Rochelle)

2.2   Digital Window Generator (Rochelle/Stultz)

2.3   Transmitter Modulator (Rochelle)

2.4   Power Amplifier (Rochelle/Shore)

2.5   Preamplifier and Main Amplifier (Blalock)

2.6   Narrowband Analog Filters (Blalock/Kennedy)

2.7   Digital Signal Processor (Bodenheimer/Senn)

2.8   Analog Fourier Filter (Rochelle)

2.9   Transmitter Pulse Shape Optimization (Rochelle/Castillo)

2.10   Experimental Vibration Studies (Rochelle)

*   Professors in Electrical Engineering, University of Tennessee, Knoxville
**   Graduate Students in Electrical Engineering, University of Tennessee, Knoxville

2.0 Conceptual System Design (Rochelle)

During Phase II/1 of this contract (1985) we demonstrated with certainty for the first time that selected lightly damped vibrations of certain unconcealed handguns could be acoustically excited with ultrasound and then detected in the visual display of our Hewlett-Packard HP3561A Dynamic Signal Analyzer. Useful detector/target ranges of up to several meters were demonstrated. Although the transmitted frequencies were well into the ultrasound region, the transmitter still emitted a noticeable and annoying audible clicking sound which at that we (Rochelle) could not explain.

Swept frequency burst and fixed frequency burst excitation were studied, but the latter was found to result in far better vibration detectability because center frequency excitation is so much more efficient for energizing a lightly damped resonance. Consequently fixed frequency excitation was selected for the present demonstration unit because we wanted to make a best effort to detect concealed handguns as specified in the Phase II/2 proposal.

Center frequency excitation of course means that the reflection and vibration signals occur at the same place in the frequency spectrum such that discrimination between the two is not possible using conventional FFT signal processing like that used in the HP3561A. Thus, a vibration cannot be reliably detected in the received data via the FFT or other frequency domain filtering approaches until after the reflections associated with the transmitted excitation pulse decay to negligible levels. For the Phase II/2 demonstration environment, the required delay time was 80 to 90 msec. Off resonance excitation could be used to slightly separate the reflection and vibration signals, but even with zoomed FFT analysis, the potential sensitivity or detectability improvement is negated by leakage due to windowing.

Windowing is inescapable, both in the transmitted signal (assuming it is not CW), and in Fourier transform processing of the received data. In the latter context, the ability of certain windows to provide significantly reduced sidelobe leakage are well

28

known and documented (as in John Young's M.S. thesis discussed elsewhere in this report). These windows can aid in reducing leakage from one frequency to another in the Fourier transform frequency spectrum, but not to the degree needed to make off-resonance excitation more sensitive than the center frequency approach using time gating to wait for reflection signal decay. Also the low sidelobe windows cause larger center lobe bandwidths and larger random noise bandwidths. Accordingly the rectangular or uniform window was adopted for received data processing in the Phase II/2 demonstration.

We (Rochelle) did, however, discover that special windowing of the transmitter pulse was effective in eliminating the aforementioned very audible click associated wit high power ultrasound transmission. Apparently, the properly windowed transmitter pulse generates significantly less acoustic energy down in the audio frequency band than does the conventional gated ultrasound burst which really corresponds to a rectangular transmitter window.

Triangular and Hanning transmitter windows were found to be about equally effective for click elimination, and both have been used in the Phase II/2 demonstration unit where they are generated digitally using EPROMs. No audible effects were noticed with these windows, even with full transmitter drive of 400 V p-p and 20 msec window width.

Optimization of transmitter pulse shape characteristics and the width in particular is the theme of Domingo Castillo's M.S. thesis which is discussed in more detail elsewhere in this report.

A block diagram of the transmitter portion of the Phase II/2 demonstration unit including the aforementioned digital window generator (labeled window) is given in Fig. 2.0-1. The ultrasound frequency source (labeled UFS) was supplied by a commercially available frequency synthesizer (Sciteq Inc. Model VDS-3) with 1 mHz resolution capability. The UFS frequencies were set digitally via BCD frequency codes supplied at
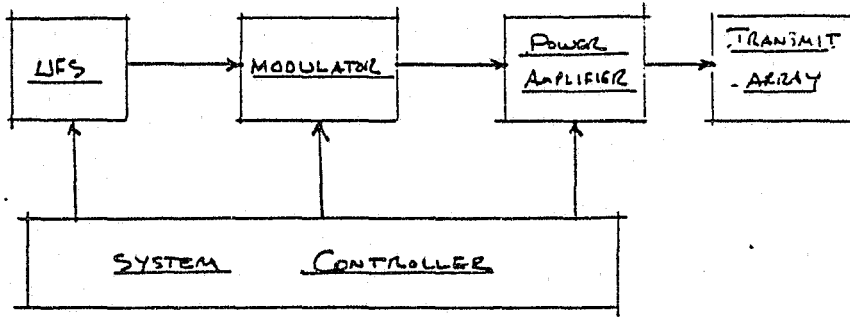
Fig. 2.0-1 Transmitter block diagram
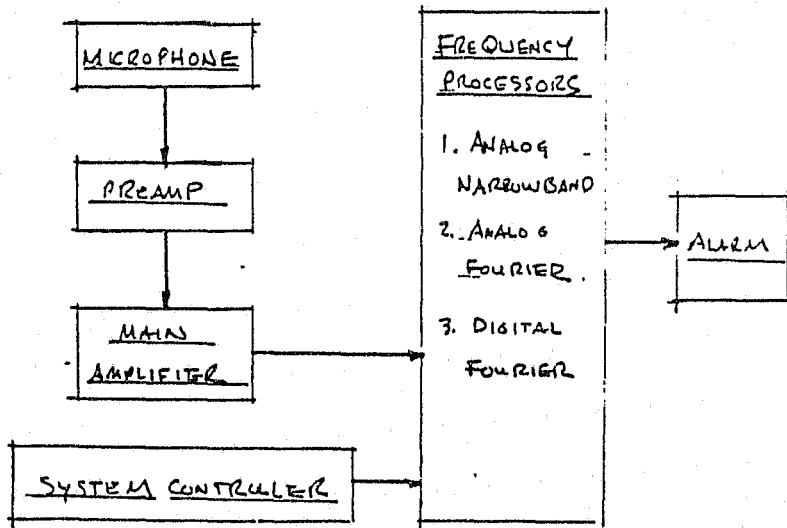
Fig. 2.0-2 Receiver block diagram

the proper time by the demonstration unit's system controller. At the same time the system controller supplied the proper band selection code to the resonant circuit switches in the power amplifier. As described later a total of four different UFS frequencies scanned sequentially were required for the Phase II/2 demonstration.

Clocking rates for the digital window generator were supplied by another Sciteq synthesizer (labeled WCS) which was also under control of the system controller. The WCS clock determined the transmitter window width, and was also designed to provide pulse to pulse phase coherence if and when the system controller might be programmed to output multiple transmitter pulses at each UFS frequency. In addition, the system controller might be programmed to output multiple transmitter pulses at each UFS frequency. In addition, the system controller supplied a logic signal, TWE, which was true only during the transmit window duration, and was used to gate on the UFS synthesizer and for gating in the transmitter modulaor circuit (labeled modulator in Fig. 2.0-1).

The transmitter modulator functioned to multiply the UFS carrier by the transmitter window to produce the windowed ultrasound pulse for input to the power amplifier and transmitter array.

As shown in Fig. 2.0-2, the receiving system for the Phase II/2 demonstration consisted mainly of (1) a low noise preamplifier with good overload recovery characteristics, (2) a main amplifier with bandpass filtering for out of band noise rejection processors including narrow band analog filters, a Fourier analog filter, and a digital Fourier transform processor unit, and (4) an alarm unit for signaling when a handgun vibration is detected.

Digital Fourier processing was clearly the method of choice because it would allow us the best chance of achieving sensitivity levels similar to those already experienced using the HP3561A analyzer. However, we were not at all sure if this processor could be ready for a September demonstration date; primarily because of delivery delays on

31

critical components. Thus, the decision to fabricate a proven narrowband filter designed by Blalock using op-amps. The noise bandwidth of these analog filters was somewhat higher than we wanted, but preliminary testing proved they offered usable detection sensitivity for unconcealed handguns at least. About this time we (Rochelle) also conceived the analog Fourier filter idea, but its design and implementation was postponed so that maximum effort could be focused on bringing together a working demonstration system by the September deadline. Ultimately, all three processors were completed and were operated in parallel during the Phase II/2 demonstration.

The digital processor and the analog Fourier filter received a logic signal (RWE) from the system controller which was true during the time slot when the main amplifier signal was to be analyzed i.e., after the reflections decay to negligible levels in the received signal. Each of the four narrowband analog filters (one for each of the four vibrations to be detected) also received an analysis trigger signal from the system controller at the appropriate time.

2.1 System Controller (Bodenheimer, Stultz, and Rochelle)

The system controller for the Phase II/2 demonstration unit was implemented with a dedicated digital hardware structure providing firmware programmability for the number of different ultrasonic frequencies to be transmitted, the precise value of each of these frequencies, the number of pulses to be transmitted for each frequency , the transmitted pulse width (window width) and repetition rate, a time delay prior to pulse transmission for setting up the power amplifier, and a time delay to allow for reflections to die out. An elementary transmit-receive timing diagram is shown in Fig. 2.1-1. The beginning of the transmit interval is signaled by a line called transmit window enable, TWE, and the beginning of th processing interval is signaled by a ine called recieve window enable, RWE.
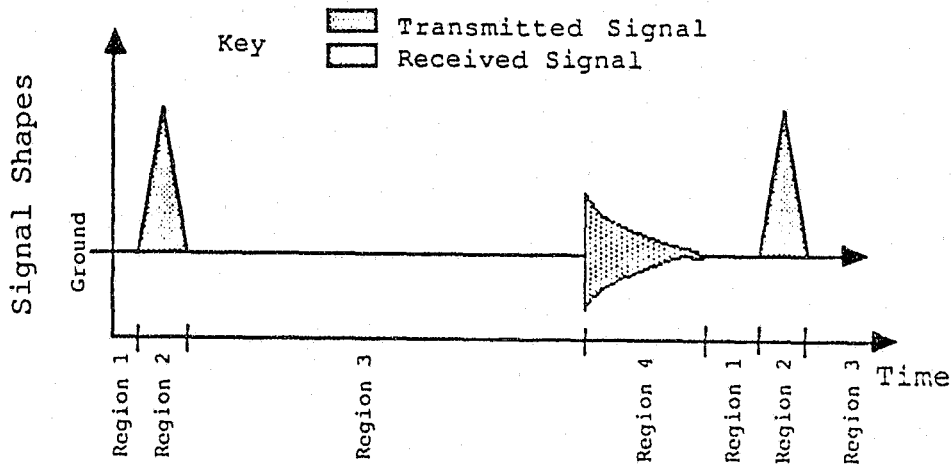
Fig. 2.1-1   Transmitted and received signal shown as they are controlled by the system controller.

A block diagram of the controller is shown in Fig. 2.1-2. The central controller steps the controller through the required steps, and also clocks out the codes and commands required by the other subsystems. The window clock synthesizer, WCS, serves as a clock for the digital window generator, and is controlled by the window control code generator, WCGG, just as the ultrasonic frequency synthesizer, UFS, is controlled by the transmitted control code generator, TCCG.

33
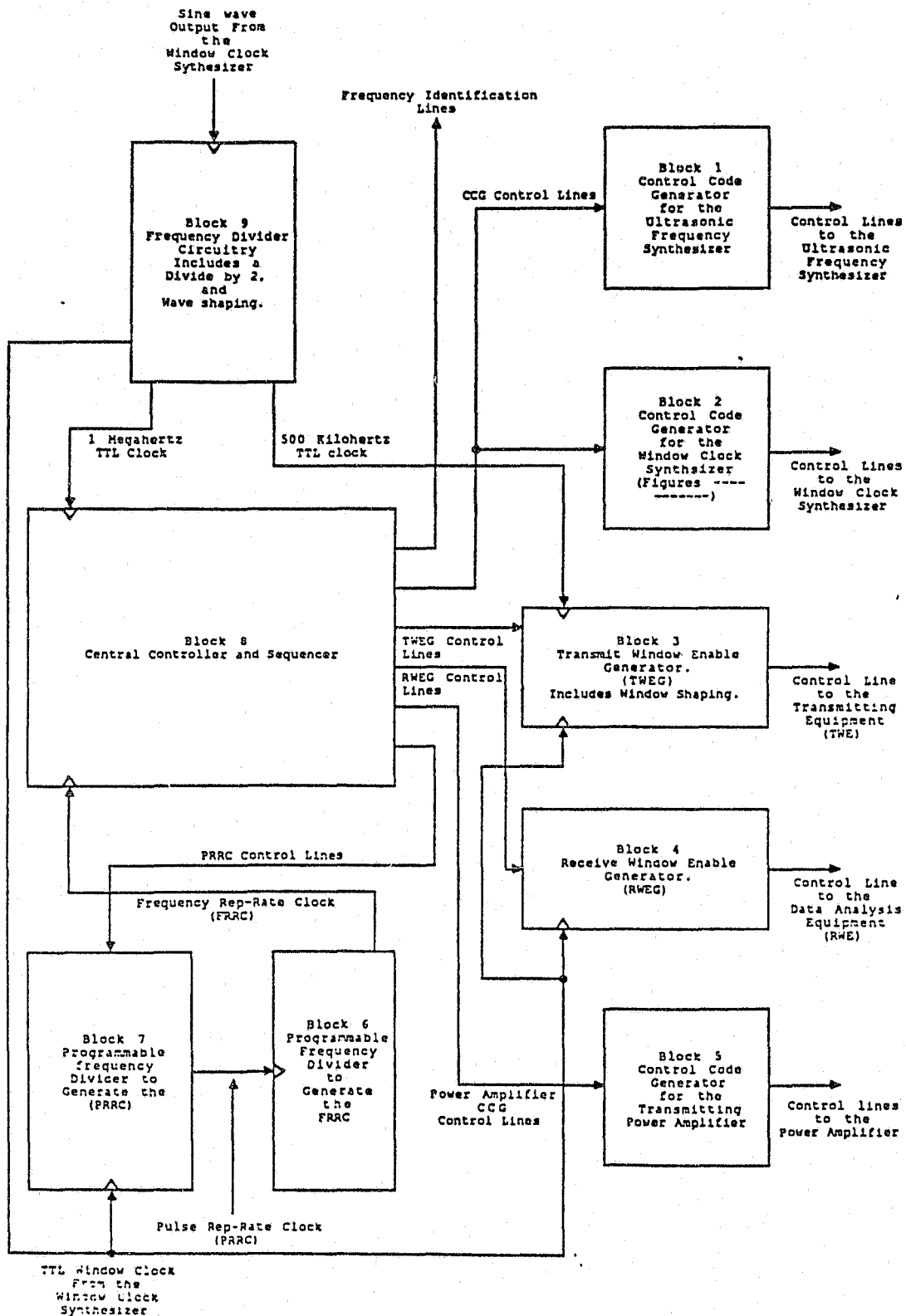
Fig. 2.1-2 Block diagram of system controller.

34
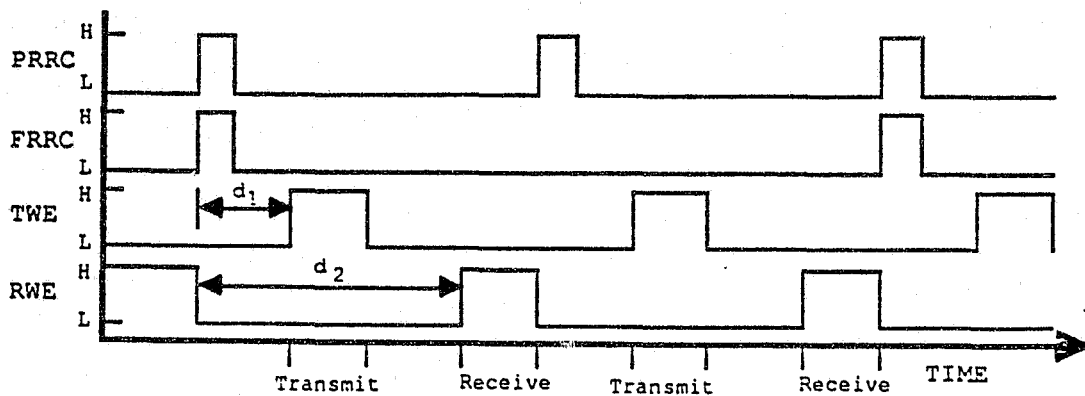
Fig. 2.1-3   Timing diagram showing clock relationships for k=2.

Fig. 2.1-3 illustrates how the various system controller clocks relate to the transmit/receive process. Note that PRRC is the base transmit pulse repetition rate, and FRRC is the rate at which the different UFS frequencies are scanned. These two rates are related through the integer, k, which represents the number of pulses transmitted per frequency. Normally k=1 was programmed to maximize the total scan rate, and minimize the handgun detection response time. TWE starts after a delay d1 from the rising edge of PRRC. This delay (0.1 msec) is included as a setup time for the power amplifier and a shutdown time for the analog filters. RWE is delayed by amount d2 (90 msec) to wait for reflections to decay before beginning to process the received signal.

The controller was built using a high speed CMOS logic family and TMS2764 EPROMs on wire-wrapped cards.

The system controller design and performance will be documented in detail in Perry Stultz's forthcoming M.S. thesis.

35

2.2 Digital Window Generator (Rochelle and Stultz)

The digital window generator, which was programmed for rectangular, triangular, or Hanning transmitter window functions, primarily consisted of an addressing counter, a 4096x12 bit EPROM, a high speed 12 bit DAC, and an analog amplifier for final scaling and offset adjust as shown in Fig. 2.2-1. A particular window function was sequentially stored in the EPROM and clocked out into the DAC each time a transmitter pulse was to be generated. The clocking rate was derived from the window clock synthesizer (WCS) which was programmed from the system controller to provide a rate as required to achieve the desired nominal width and to maintain an exact integral number of UFS cycles within the window.
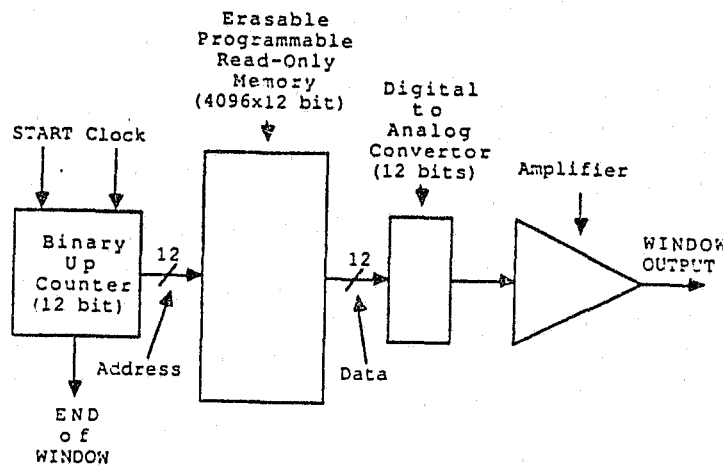
Fig. 2.2-1 Digital window generator block diagram.

The digital window generator will be fully documented in Perry Stultz's forthcoming M.S. thesis.

36

2.3 Transmitter Modulator (Rochelle)

The modulator is a very straightforward design which uses a high performance analog multiplier integrated circuit to multiply the UFS ultrasonic carrier frequency by the output of the digital window generator as shown in Fig. 2.3-1. The multiplier's output and its UFS input were ac coupled, op-amp buffered, and isolated with CMOS controlled analog switches at all times except during the TWE transmit interval to guard against any superfluous signal coupling through the modulator into the power amplifier input. The internally trimmed transconductance multiplier was sufficiently linear to maintain good output waveform symmetry with negligible unintentional distortion. The modulator did not contribute significantly to the output random noise level of the power amplifier.
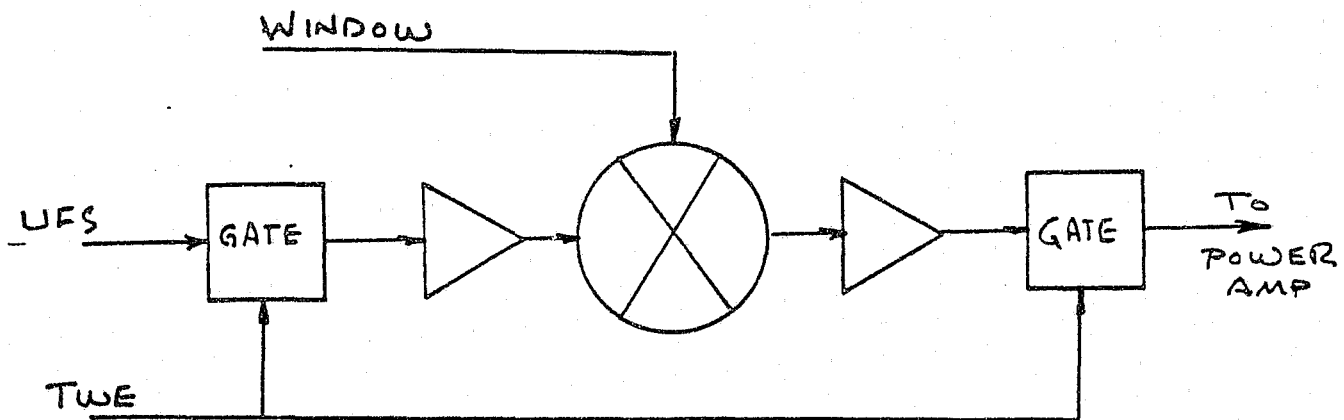
Fig. 2.3-1 Transmitter modulator block diagram.

2.4 Power Amplifier (Rochelle and Shore)

Principal issues considered in designing the high efficiency transmitter power amplifier were (1) use of a step-up transformer between the output stage and the transducer load, (2) selection of suitable output and output driver stage configurations, (3) use of switched resonance methods to cover the full 20-100 kHz band with minimum power dissipation in the amplifier and its supporting power supplies, and (4) use of negative feedback to minimize output signal distortion and stabilize power amp gain. Item (3) is crucially important in the context of any kind of portable handgun detection system.

Transformer step-up between the amplifier and transducer array was used primarily because it allows lower dc supply voltages, lower p-p voltage swing requirements in the output stage and its drivers, and lower signal levels in the switched resonator paths which are optimally located on the transformer's primary side. The latter means lower inductance values can be used for the resonating branches. Initially the transformer design goal was to provide 2000 V p-p at the array, but this was scaled back to 400 V p-p upon the discovery that the Polaroid transducer SPL level saturates quickly when driven beyond that point. A drive level of 400 V p-p was ultimately adopted for the Phase II/2 demonstration test.

Care was taken to keep the transformer operation in a linear region because it was not included in the amplifier's overall feedback loop.

The three topologies considered for the output stage were (1) complementary common source, (2) push-pull common source, and (3) complementary common drain. The disadvantage of the common source designs is the complexity of their driver circuit. Both common source circuits require the driver circuit to provide current for the full input capacitance of the power device since gain is required and no reduction of the capacitances by bootstrapping is possible. The complementary circuit requires the driver circuit to develop signals referenced to each of the power supplies. The push-pull

circuit requires inversion of the signal for one of the power transistors and a special transformer, both of which are complications.

The complementary common drain circuit has the advantage of simple, low-power driver circuits since the gate-drain capacitance is negligible (near unity gate-source voltage gain), and the voltage between the gate and source is nearly constant. The drive signals for the power transistors are identical except for a dc offset; this also simplifies the driver circuitry. The disadvantages to the complementary common drain topology are: (1) the drive signal must be larger in magnitude than the output signal, and (2) capacitive loading may cause oscillation. The first disadvantage is not a great difficulty, but the second one could be. Modeling by SPICE produced inconclusive result, but experimental work with the output stage indicated that the oscillation problem could be solved.

A complementary gate driver circuit was used to provide the low output impedance necessary to adequately charge and discharge the gate input capacitance of the MOSFETs used in the output stage described above while maintaining single pole roll-off within the negative feedback loop. Unbypassed emitter resistors were used to suppress thermal runaway and to increase the gate driver input impedance. The bias point of a diode has a negative forward voltage versus temperature coefficient. As the temperature rises in the device during operation, the bias voltage required to support a given current decreases. Consequently, more current is allowed to pass through the device; this causes more heat which causes further increases in current. If this increase is not checked, the devices will overheat until they are destroyed. This positive thermal feedback effect is known as "thermal runaway." In order to prevent thermal runaway, the emitter resistors were chosen large enough so that an increase in the current through the resistors increases the voltage across the resistors at least as much as the change in temperature decreased the bias voltage.

39

The 5 nF transmitter array capacitance requires relatively large volt-ampere average energy levels (125 var when driven at 400 V p-p and 100 kHz), especially at the high end of our operating frequency band. To supply these high var levels directly from the power amplifier's output stage would result in hundreds of watts power loss requiring large heat sinks and bulky dc power supplies. Since the electrostatic transducers were known to have practically zero power factor, we felt the high var requirements could be supplied by switched resonant networks such that the vars demanded directly from the output stage would be minimized along with the power amplifier's total size and weight.

The two configurations possible for the resonant inductors and associated switches are series and parallel. The parallel circuit (Fig. 2.4-1) impedance increases toward infinity as resonance is approached with losses in the wiring and inductance core as well as stray inductance and capacitance limiting the impedance to some finite value. The series circuit's impedance attempts to approach zero reactance at resonance. At resonance, the impedance is real, not reactive; consequently, the amplifier can more efficiently drive the load at resonance.
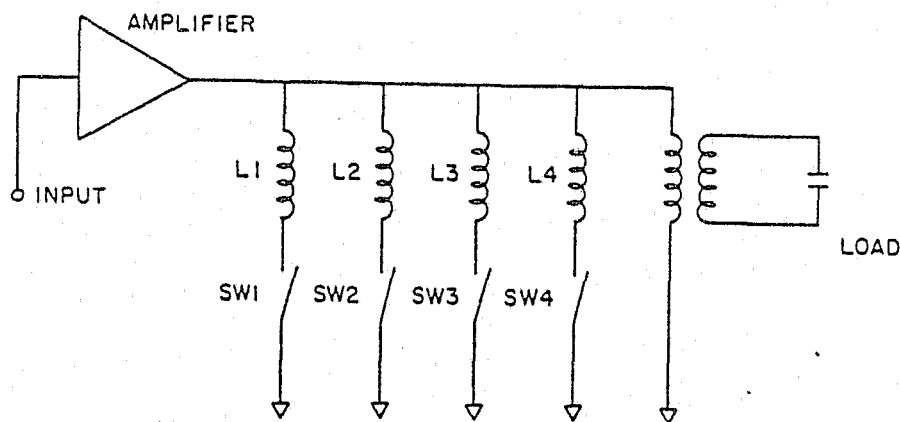
Fig. 2.4-1 Parallel resonance arrangement.

The maximum available output power into resistive loads is the maximum product of the output voltage times the output current available at that voltage. Given a maximum output voltage and current rating, there is a minimum large signal impedance

which can be assigned to the output stage. For loads below this minimum impedance, the maximum current is reached before the maximum voltage; and thus, the power delivered to the load is less than the maximum. Similarly, for load impedances above the optimum, the maximum voltage is achieved prior to the current peaking; consequently, the output power is less than the maximum available. Given an output power level, reducing the voltage across the output devices or the current through them increases the efficiency of the output stage since less power will be lost as heat in the output devices. Essentially, this means that increasing the load impedance, as long as the power level remains constant, tends to improve the efficiency of the output stage as it nears resonance. On the other hand, the series configuration's impedance drops as its impedance becomes real; consequently, the voltage across the transistors in the output stage would increase and the transistors would be forced to dissipate more power near resonance.

Furthermore, with the series inductors, the full load current would circulate through the output stage of the amplifier; this would cause much heat and tends to defeat the purpose of having the energy storage. By using the parallel configuration, the large resonant circulating current flows through the inductors and the transformer, not the output transistors. Another disadvantage to the series configuration is that the loop transmission will vary significantly as the frequency approaches the resonant frequency if shunt feedback is used at the amplifier's output. This is because there is voltage division between the output impedance of the output stage and the input impedance of the effective load, the inductor/transformer combination. For the series configuration, as the frequency approaches resonance, the input impedance of the effective load drops, consequently, so would the magnitude of the loop transmission. This effect would probably require a sophisticated compensation system in the feedback. Based on these observations, the parallel inductor configuration was chosen.

One concern about using the resonant load circuit was the transient response of the resonant tank. SPICE analysis of parallel and series resonant circuits indicated that parallel resonance was advantageous in this respect as well. The use of a low impedance driver circuit with feedback connected to the junction of the power transistors and the resonant tank allowed good control of the start-up and stopping transients as well as good control of the steady-state output voltage.
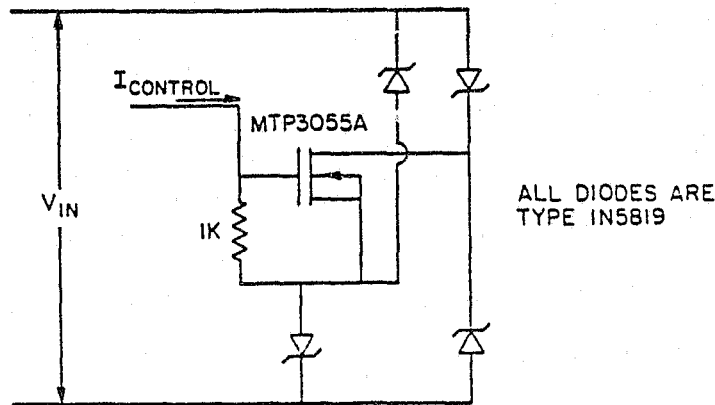
Fig. 2.4-2 Basic resonant inductor switch circuit.

The single MOSFET transistor switch in a bridge circuit (see Fig. 2.4-2) was chosen to switch the inductors in and out of the circuit. Reed relays (cold-switched) were not considered because of questionable long term reliability when used at the relatively high switching rates required for the present application. In order to allow the source terminal to float as necessary when the switch is "off," the control voltage was changed to a control current by adding a 1 kohm resistor. By using a current instead of a voltage control, floating supplies or other means of providing a floating voltage source were avoided. The 1 kohm resistor allows a current of 15 mA to fully turn the switch on. This value was chosen because an LED was to be included in series with the control current to indicate when the switch is on and between 10 and 15 V are required to fully turn the MOSFET on.

42

The switches are controlled by a digital code from the demonstration unit's system controller which selects the proper combination of parallel inductors for the particular frequency being transmitted.

Negative feedback was considered necessary to improve stability, linearity, and simplify the biasing of the amplifier. Considerations in the design of the amplifier and feedback network were stability, step response, adequate loop transmission to reduce distortion, adequate gain to limit input signal to a low level, and the speeds of the various stages in the amplifier. Although the input is always a sine wave, it is amplitude modulated. In the case of a rectangular modulating signal, the output should show no signs of overshoot or ringing; i.e., good step response. Although good step response and stability can be achieved with a variety of configurations; the simplest, and hence the most desirable approach is with dominant pole roll-off of the loop gain. This was achieved by careful design of the op-amp stage, voltage gain stage, current gain stage, and feedback netwrk which are identified in the block diagram of Fig. 2.4-3.

The power amplifier design and performance is completely described in Alex Shore's M.S. Thesis: <u>A Highly Efficient Amplifier for Driving A Capacitive Load</u>, December, 1986.

43
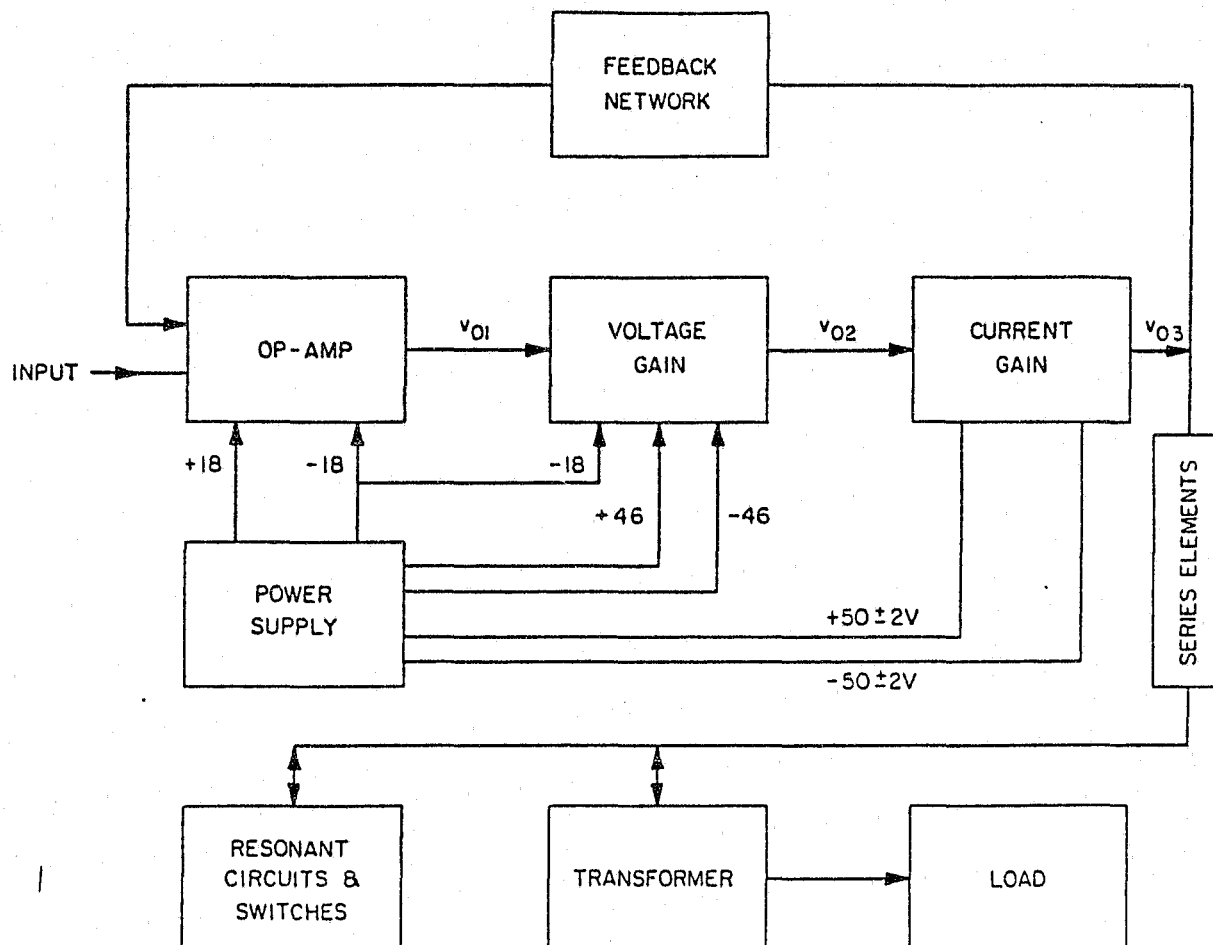
Fig. 2.4-3 Power amplifier block diagram.

2.5   Preamplifier and Main Amplifier (Blalock)

The completed research and development work in analog electronics in 1986 resulted in several sub-systems for the Demonstration Unit (DU) displayed at NIJ in September, 1986. The sub-systems to be discussed in this chapter are the preamplifier and main amplifier. An analog detector for the Demonstration Unit is discussed in the next chapter.

Preamplifier

The preamplifier consists of a low noise input section followed by a wideband voltage gain section. The equivalent input noise voltage spectrum of the input section is about 1 nV/Hz$^{\frac{1}{2}}$, the voltage gain is 103 V/V, the bandwidth extends from 41 Hz to 5.8 MHz for a 400 pF microphone input transducer, and the output signal slew rate is 12.3 V/microsec. The wideband gain section has a gain of 10 V/V output with bandwidth extending from 528 Hz to 9 MHz, and a gain of 100 V/V output with a bandwidth extending from about 1056 Hz to 6 MHz. Thus, wideband outputs are available with gains of x103, x1,030, or x10,300 V/V.

The detailed circuit diagram of the preamplifier was published on pages 66 and 72 of the Interim Report – Phase I and II/1, March, 1986.

Main Amplifier

The main amplifier was designed to (1) provide all additional voltage gain necessary to raise the received ultrasonic signal to a level suitable for processing by the detection circuits, (2) limit the system bandwidth to a range needed only by the received signals so that noise input to the detection circuits is minimized, and (3) limit the dynamic range of signals transmitted to the detectors. The main amplifier voltage gain is continuously adjustable from 375 to 1876 V/V over a 3 dB bandwidth extending from 25.5 kHz to 93.7 kHz. The frequency slopes outside the band pass region are controlled by 9-pole high-pass and 8-pole low-pass filters. The limiting of signal amplitude is accomplished by p-n junction clamping resulting in a logarithmic amplitude for

45

overloading signals. The amplifier output is linear to a sinusoidal peak value of about 4 volts; the heavily overloaded output is 6.5 V peak.

The circuit details of the main amplifier are shown in Fig. 2.5-1. The first stage is a variable gain wideband amplifier using one section of the dual LF353 Op-Amp chip. The voltage gain can be varied from unity to +5.12 V/V. The input circuit provides one of the 9 high-pass poles.

The second stage is a two-pole RC active high-pass filter using a constant gain (1.605 V/V) Op Amp circuit. This stage uses the second section of the LF353.

The third, fourth and fifth stages are identical and provide two high-pass poles and two low-pass poles. The two high-pass poles are provided by the input coupling network and by the 1.78k-0.15 microF network connected to the Op-Amp negative input terminal. The low-pass poles are realized in a second-order constant gain (G=10.78 V/V) RC active filter design using the wideband (GB=100 MHz) HA2627 Op-Amp. The high gain-bandwidth product is necessary to sustain the high gain with minimum distortion (make spurious harmonics negligible). The diodes connected to the positive input teminal of the Op-Amp produce a controlled logarithmic response in overload to avoid saturation of the Op-Amp. Our research indicates that logarithmic overloading minimizes the generation of harmonics and sum-and-difference signals that could generate false detector outputs.

Any high-frequency spurious signals generated in the controlled overloading stages are attenuated by the last stage of the main amplifier. This stage is a second order RC active low-pass filter with unity widband and low-frequency gain; therefore, the stage cannot be saturated with the signal from stage five.
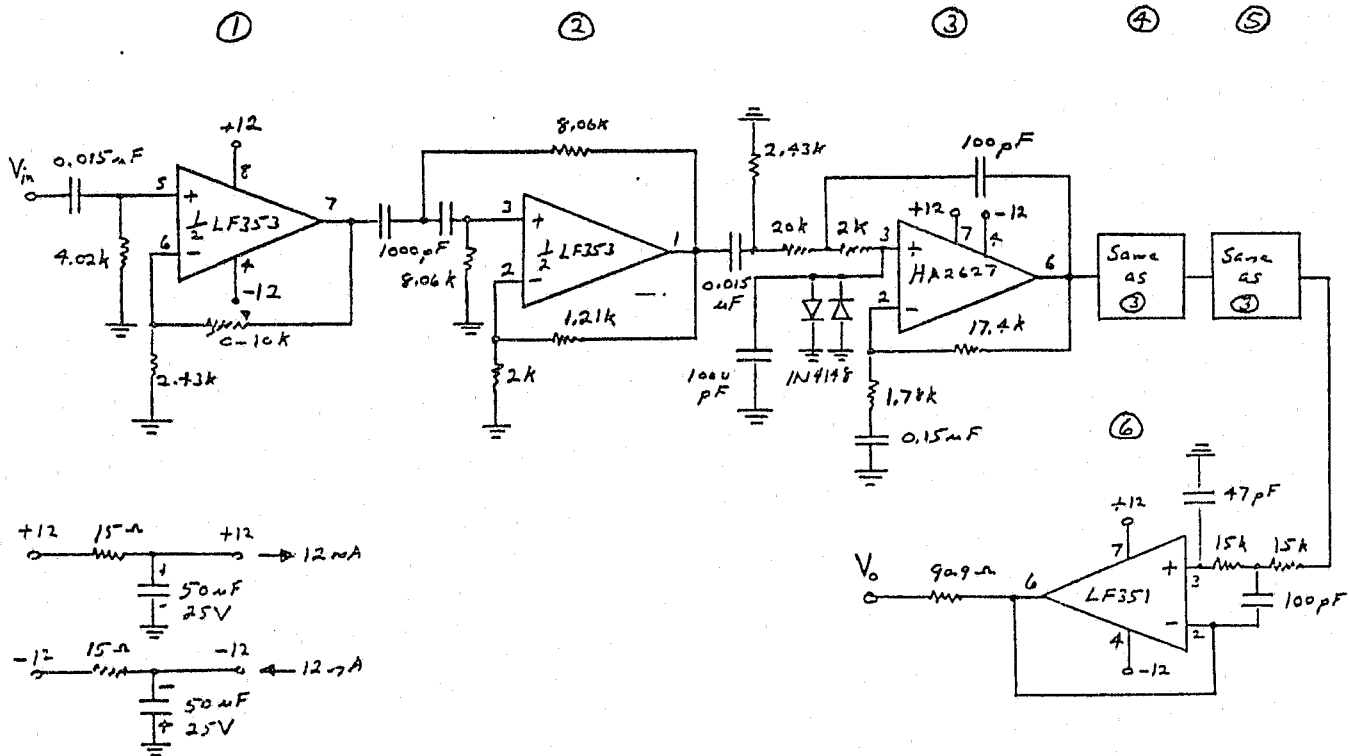
Fig. 2.5-1. Circuit Diagram of the Main Amplifier.

47

2.6   Narrowband Analog Filters (Blalock and Kennedy)

Analog Detector (Blalock)

The analog detector starts analysis of the main amplifier output signal at a time commanded by a TTL pulse from the control unit. The analysis time is set by an adjustable-period monostable multivibrator chip in the detector. The monostable chip controls the transmission time of a CMOS analog switch in the signal path. The switch output, which is a time sample (burst) of the amplified receiver signal, is next fed through a very narrow band filter (Q typically 100) and then into an active full-wave rectifier. The average value of the rectifier output voltage is acquired with a gated integrator with integration time determined by a TTL pulse from time control unit. The output stage of the detector is a voltage discriminator with adjustable threshold. The discriminator delivers a TTL alarm pulse to the Annunciator (Handgun Alarm) when the interator output voltage exceeds the threshold value.

The analog detector developed for the demonstration unit has 4 channels, each as described above. The narrow-band filter in each channel is tuned to a specific vibration frequency so that the detector could be set to interrogate the receiver signal for up to 4 different targets or up to 4 different vibration resonances for a single target. The detection is presently set to respond to a single resonance for two different targets and two resonances for a third target.

The circuit details of the analog detector is shown in Fig. 2.6-1. The detector has two channels processing input signals S_1 and S_2. The input gate is a four-section CMOS HI-201HS-5 analog switch controlled by TTL inputs from the 4528B CMOS dual monostable multivibrator. Two sections of the analog switch are used in each channel and are connected in the series-parallel configuration (one section in series with the signal path, another section connected between the signal path and ground). The data analysis times (switch is transmitting) for the two channels are controlled by the 500k potentiometer circuits in the monostable multivibrator network. Coarse adjustments of
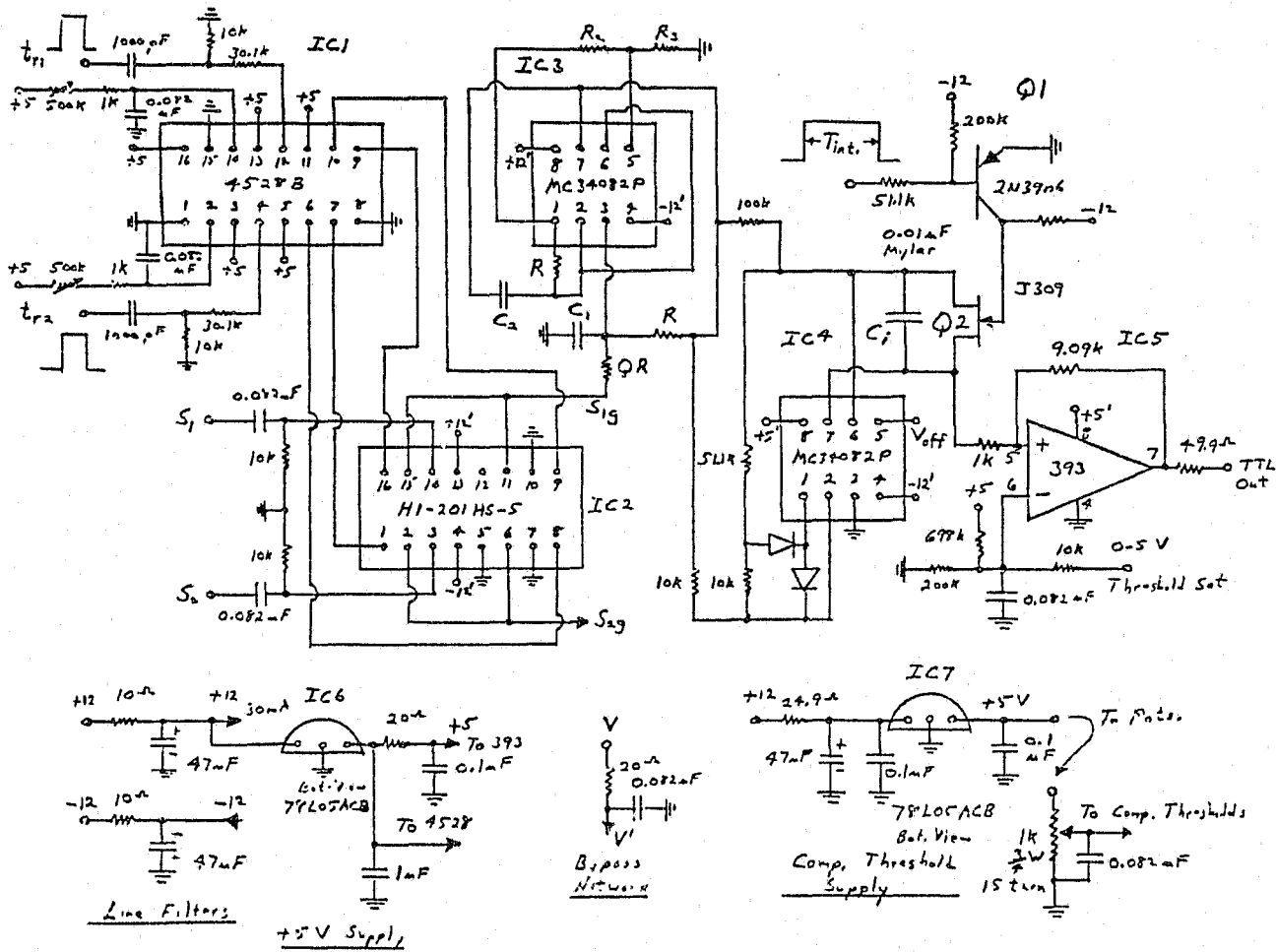
Fig. 2.6-1 Circuit Diagram of the Analog Detector.

49

the time can be accomplished by replacing the 0.082 microF capacitors with other capacitors of different values. The analysis times for the circuit shown in Fig. 2.6-1 can be varied from 90 micros to 14.5 ms. The analysis times are initiated by the leading (positive going) edge of the TTL control pulses to t_{r1} and t_{r2}.

The outputs of the analog switches are the gated signals S_{1g} and S_{2g} each of which are fed into a high Q bandpass filter; only the channel 1 filter is shown in Fig. 2.6-1. The high Q filter is a very novel design discussed in the chapter of this part authored by Dr. E. J. Kennedy. Stable Q values over 300 have been achieved using low TC metal film resistors for R, R_2 and R_3 and selected NPO capacitors for C_1 and C_2. The Q set in the Fig. 2.6-2 design was about 100. The two Op-Amps (MC34082P) used in the filter implementation were in a dual package (IC3), had J-FET input stages and were fully compensated internally with a 8 MHz gain-bandwidth product and slew rate of 25 V/microsec.

Another MC34082P dual Op-Amp chip (IC4) was used to implement a combination absolute-value, gated integrator circuit. The input signal burst is, therefore, full-wave rectified and then integrated on the capacitor C_i. The integration process is under the control of the T_{int} pulse into the base of Q1 which drives the J-FET switch Q2. When Q2 is saturated, the capacitor C_i is held in the discharge mode with the integrator output (pin 7, IC4) near zero volts dc. A small $\pm V_{off}$ applied to pin 5 of IC4 is used to set the integrator output to zero for no signal input. The value of V_{off} must be experimentally determined for each channel and is usually obtained with a simple voltage divider connected to one of the power supply lines.

The interator output feeds a comparator connected in a Schmitt-trigger configuration (IC5). When a positive-going signal crosses the trigger threshold, the comparator output (pin 7) switches high ($\approx 5V$). The trigger threshold in the DU is set remotely by the potentiometer in the IC7 circuit.

50

Most of the power line inputs to the IC chips are bypassed by the simple RC network in Fig. 2.6-1. This bypassing is necessary to eliminate inadvertent feedback among the IC chips through the power lines.

Analog Filters (Kennedy)

The first filter is the high-Q bandpass design used by the analog detector (see Fig. 2.6-1) in the Demonstration Unit.

The circuit of the high-Q bandpass (BP) filter uses two Op-Amps (actually, a dual MC34082 device was used) as indicated in Fig. 2.6-2. The design theory is contained in Chapter 6, Section 6.4.2 of the author's text* on operational amplifiers. The circuit is particularly useful for high-Q applications, since only one resistor (R_1) need be changed to vary the Q. Changing R_1 has no effect on the BP center frequency w_0. The circuit will operate effectively for a Q as large as 300. If resistors R_2 and R_5 are equal, while capacitors C_1 and C_2 are equal, and if Resistor R_3 is equal to resistor R_4 the transfer function for the circuit of Fig. 2.6-2 is:

$$\frac{V_0}{V_1} = \frac{S\left(\frac{2w_0}{Q}\right)}{S^2 + S\left(\frac{w_0}{Q}\right) + w_0^2} \tag{1}$$

where

$$R_3 = R_4 = R, C_1 = C_2 = C, R_1 = QR, \text{ and } w_0 = 1/RC$$

For the filter used in the analog detector, Q is about 100, while center frequencies varied from 35 kHz to 55 kHz, dependent upon the particular weapon signature frequency being amplified.

---

*E.J. Kennedy, Operational Amplifier Circuits, Theory and Applications, Holt, Rinehart, and Winston, New York (In press; publication September 1987).

$C_2 = C$

$R_1 = QR$

$R_4 = R$

$R_2 = R_5$

R_5

$C_1 = C$

v_I

v_0

$R_3 = R$
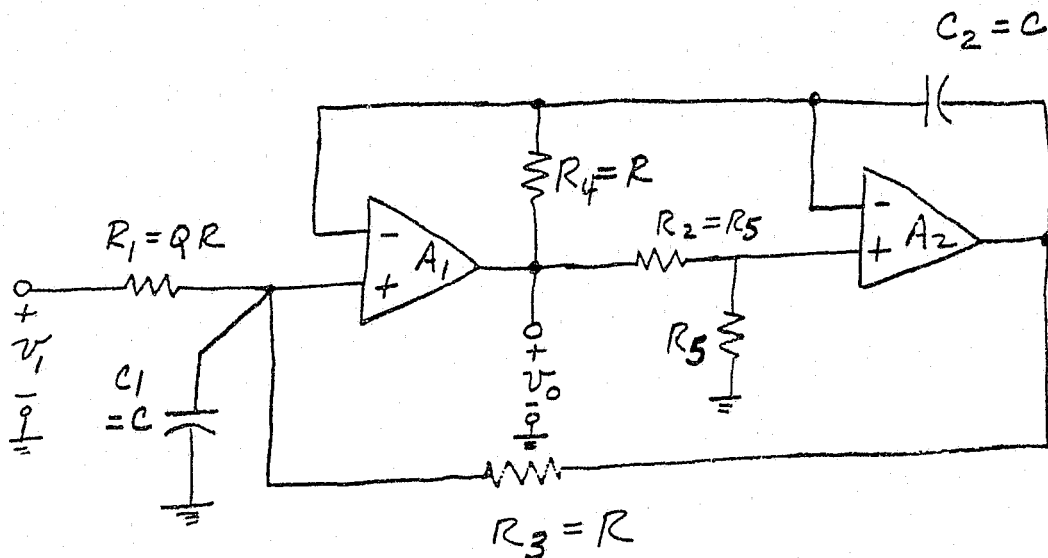
A_1-A_2 = MC34082
All power supplies are either ±12V, or ±15V
All resistors are ±1%, MF
All capacitors are matched, NPO, ceramic

Fig. 2.6-2 High Q bandpass filter.

The second filter developed for the project was a state-variable (SV) filter covering the frequency range from 10-100 kHz. The circuit is similar to that shown in Problem 6.38 in the aforementioned textbook. The circuit is shown in Fig. 2.6-3. Although much more involved than the BP filter of Fig. 2.6-2, the SV filter has the added feature of offering simultaneous outputs for all basic filter functions; the low-pass (LP), high-pass (HP), band-pass (BP), and even band-reject (BR). In the circuit of Fig. 2.6-3, a four Op-Amp filter is combined with a dual operational transconductance amplifier, thereby obtaining a shift in the center (or, cutoff) frequency as a function of the input dc control voltage [f_0 set in Fig. 2.6-3]. Thus, the center frequency w_0 can track the input control voltage signal; i.e., for -10V f_0 set <-1V we have 100 kHz f_0>10 kHz. The voltage-input to frequency-output change is controlled by a dual operational-transconductance-amplifier (OTA), A and B of Fig. 2.6-3, the NE5517 integrated circuit. The Op-Amps A$_{1A}$-$_{2A}$, A$_{1B}$-$_{2B}$ in the figure are obtained using the dual MC34082 Op-Amp.

52

The **Q** of this filter circuit is set by resistor R_7 in Fig. 2.6-3. Due to 3 Op-Amps now inside the feedback loop, a practical limit on the maximum **Q** for the circuit is >50.

In actual use, the primary use of the tracking filter would be probably as an aid in removing unwanted interference signals from the signal input at the main amplifier.
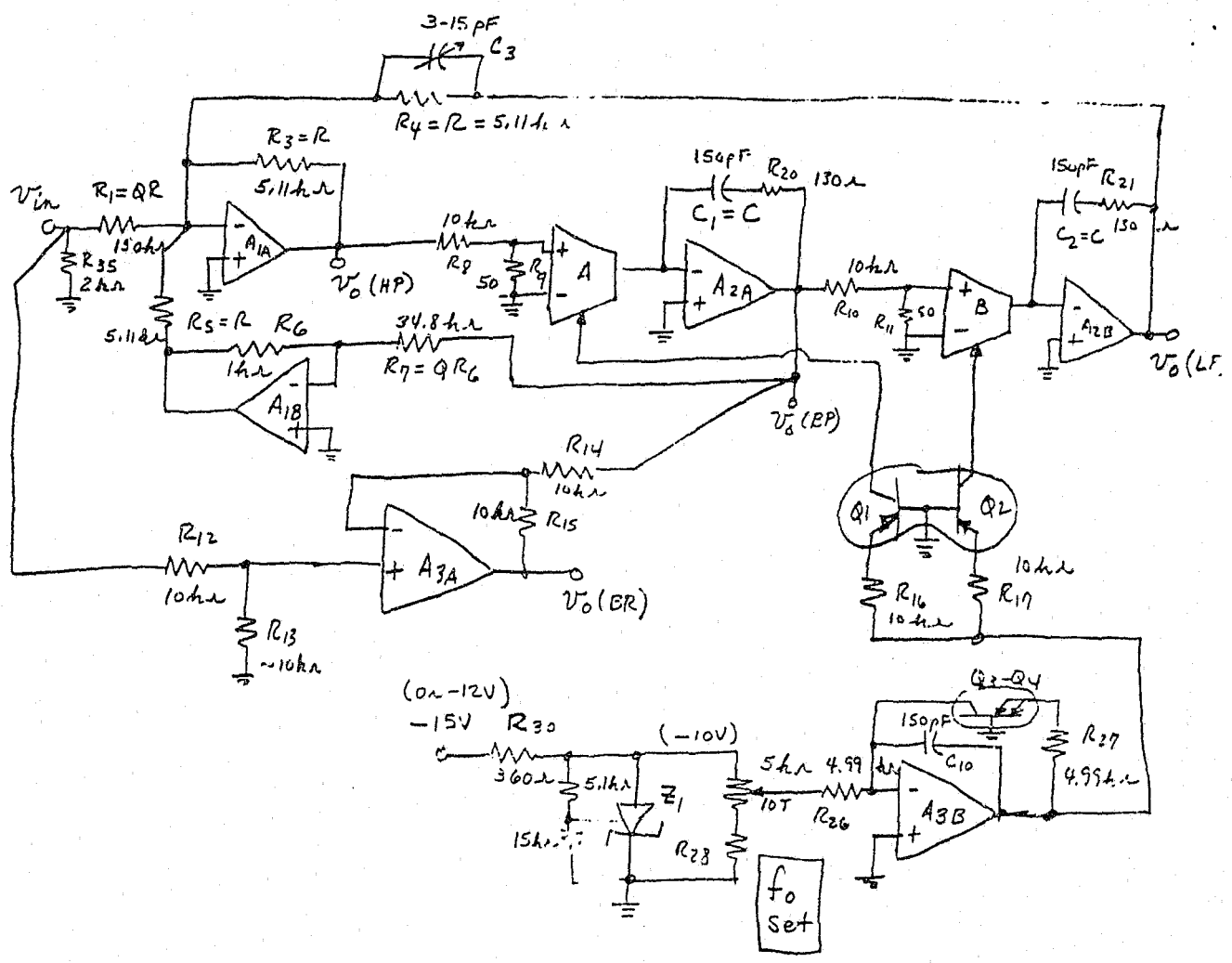
A$_1$-A$_3$ = MC34082
Q$_1$ - Q$_4$ = AD821
All resistors ±1%, MF
All capacitors are matched, NPO, ceramics
Power Supplies are ±15V (or ±12V)
Z$_1$ = TLC431

Fig. 2.6-3 State variable filter.

2.7 Digital Signal Processor (Bodenheimer, Senn and Young)

In 1986, the effort in Digital Signal Processing (DSP) resulted in achievements in three areas:

Task 1. An investigation related to the optimization of a window function for transient data was completed.

Task 2. The development of DSP hardware and software for identifying a target from a limited number of spectral points was completed.

Task 3. The design and implementation of a controller for controlling the Demonstration Unit was completed.

Subsystems resulting from the efforts in Task 2 and Task 3 were incorporated in the unit demonstrated at NIJ in the Fall of 1986.

In this chapter Task 1 and Task 2 are described. Task 3 is described in chapter 2.1.

Task 1 (Young and Bodenheimer)

The following summary describes the research to identify an optimum window function. For a more complete description of this research see the reference, *Young, John W., "Digital Windowing of Transient Signals For Fourier Spectrum Enhancement," Master of Engineering Thesis, The University of Tennessee, Knoxville, Tennessee, March, 1987. (Robert E. Bodenheimer, Major Professor)*

In order to be able to determine the vibration modes present in a target, the discrete Fourier transform is being used to transform the time signal into its frequency spectrum. The information in the Fourier transform can be enhanced by first windowing the received signal. Several common windows have been investigated in order to determine how they effect the Fourier transform of the received signal and two other windowing functions have been developed in an attempt to further enhance the Fourier transform. Most of the work has been with known window functions and with the Rayleigh distribution and a modified Rayleigh window. The Fourier spectrum of damped data and the effects of the different windows on the spectrum have been investigated in

detail. The investigation has involved the spread of the spectrum due to the different windows as well as the side lobe levels. Part of the investigation was to determine the resolution of the DFT so that the minimum frequency spacing of two frequency components in a returned signal that can be resolved could be determined. Also noise has been added to the damped data to determine the effects of the windows on noisy data and to determine if the exponentially damped windows improve the signal to noise ratio of the damped data.

Over 200 window variations have been developed in the search of the ideal window function. Each window was developed to provide features that are desirable for different types of input functions and for extracting different types of information from the Fourier transform. All windows have a Fourier transform that consists of a main lobe at the origin and side lobes at both sides. The rectangular window produces the smallest main lobe at the expense of large side lobes (see Fig. 2.7-1). As seen from Fig. 2.7-2, the triangular window has smaller side lobes, but a wider main lobe than the rectangular window. The width of the main lobe is responsible for a broadening, or "smearing" of the features of the DFT. Therefore, the main lobe is largely responsible for the broadening of the resolution of the DFT, while the side lobes give rise to ripples in the transformation. Thus, there is a trade-off between the width of the transition region and the magnitude of the side lobes. Both cause distortion in the DFT.

The Hanning, Hamming and Blackman windows are common windowing functions used with digital data acquisition. Each represent a trade-off in the three main window characteristics -- resolution degradation due to the main lobe, leakage due to the near side lobes, and leakage due to the far side lobes. The window functions for the three windows are given below.

VALUE
2000.

1666.

1333.

1000.

666.7

333.3

0.0
0.0   1.500   3.200   4.800   6.400
   .8000   2.100   4.000   5.600
        TIME   X10⁻¹

DB
100.0

83.34

66.67

50.00

33.33

16.66

0.0
0.0   12.50   25.00   37.50   50.00
   6.250   18.75   31.25   43.75
   FREQ
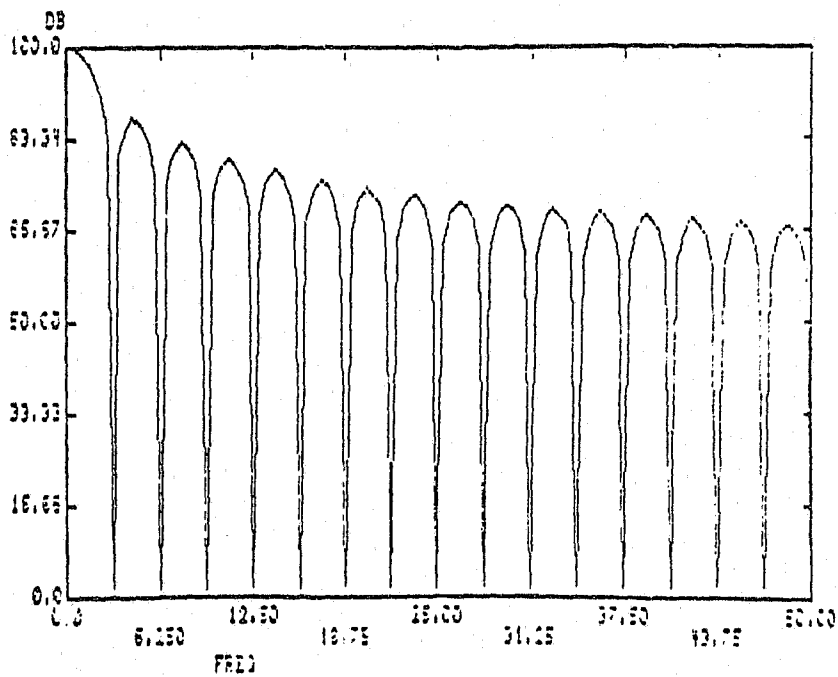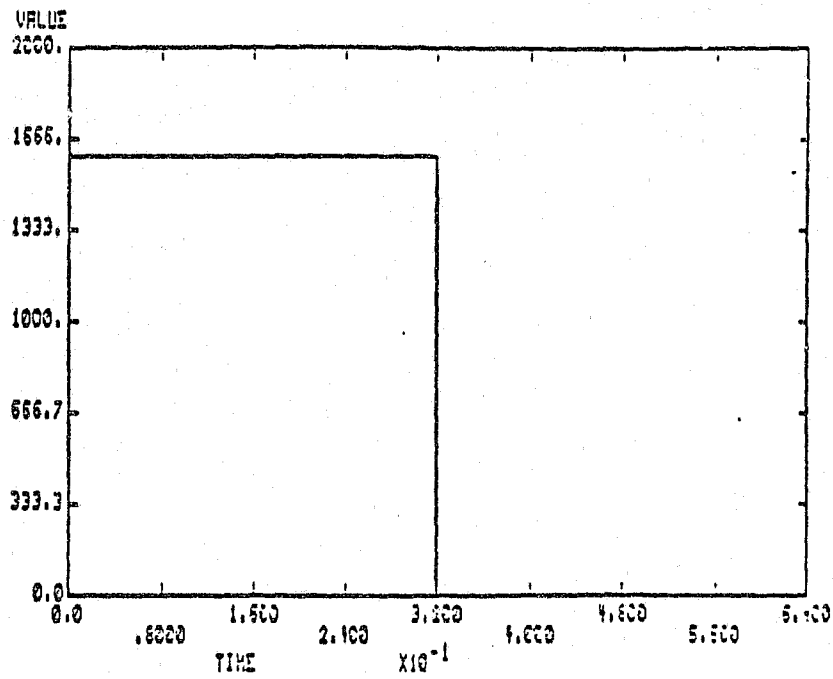
Fig. 2.7-1 Rectangular pulse of duration T and the Fourier transform of the pulse.

56
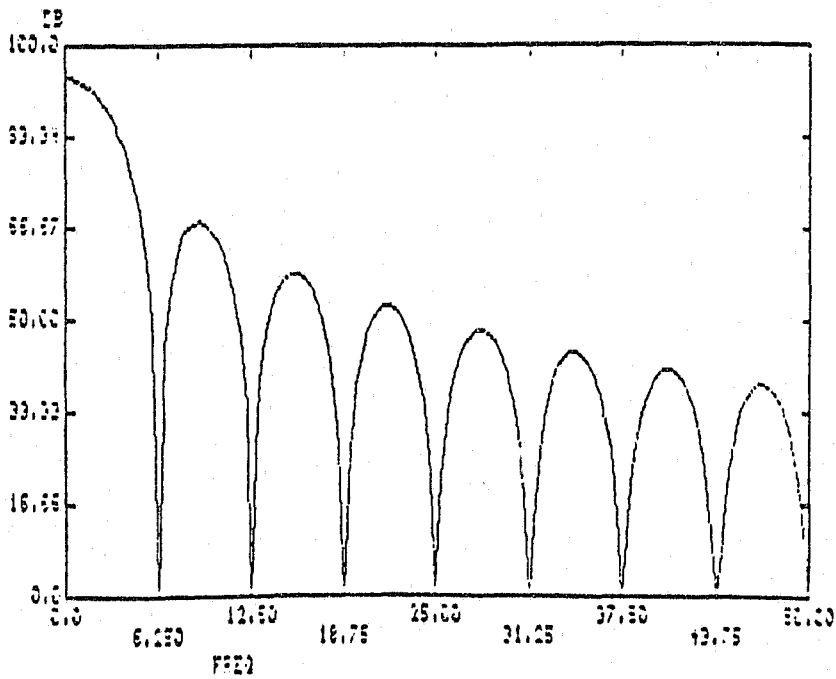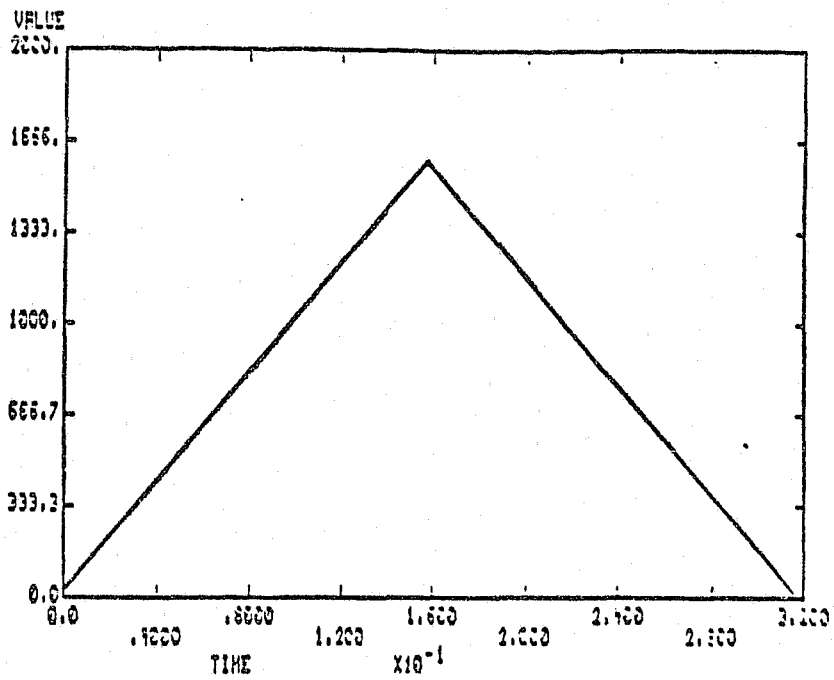
Fig. 2.7-2 Triangular window with its Fourier Transform.

57

Hanning: $(0 <= n <= N - 1)$

   $w(n) = 1/2 [1 - \cos(2 * \pi * n) / (N - 1)]$

Hamming: $(0 <= n <= N - 1)$

   $w(n) = 0.54 - 0.46 \cos (2 * \pi * n) / (N - 1)$

Blackman: $(0 <= n <= N - 1)$

   $w(n) = 0.42 - 0.5 \cos (2 * \pi * n) / (N - 1)$

   $+ 0.08 \cos (4 * \pi * n) / (N - 1)$

where n is the nth point in the window, and N is the total number of points. The windows and their transforms are shown in Figs. 2.7-3, 2.7-4 and 2.7-5. As a comparison of the windows the 3 dB bandwidth of the main lobe, peak ripple value of the side lobes, and the asymptotic decay rate of the side lobe envelope are tabulated in Table 2.7-1 for each of the window functions previously discussed.

As can be seen from Table 2.7-1, the rectangular window does have the narrowest main lobe and the larges side lobes with only a 6 dB/octave rolloff. The triangular window offers some improvement over the rectangular window in reduction of the side lobes in terms of absolute reduction (down 13 more db) and in terms of rolloff (12 db/octave versus 6 db/octave). However, the main lobe is approximately 50% wider. The Hanning window produces a still lower side lobe level (-32 db) than the triangular window and offers a greater side lobe rolloff rate (18 db/octave) at the expense of a slightly wider main lobe (12.8%). Finally, the Hamming (see Fig. 2.7-4) and Blackman (see Fig. 2.7-5) windows offer additional variations in the trade-offs between the width of the main lobe, side lobe magnitude and side lobe rolloff. Since one cannot define an optimum window for all digital signal acquisition applications, the window should be selected on the basis of which window produces the best results for a given application.
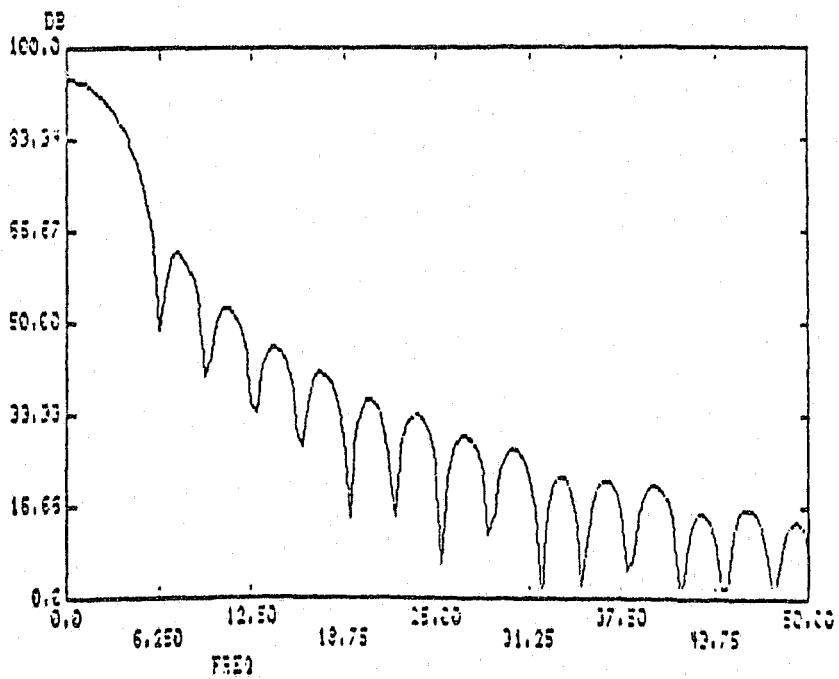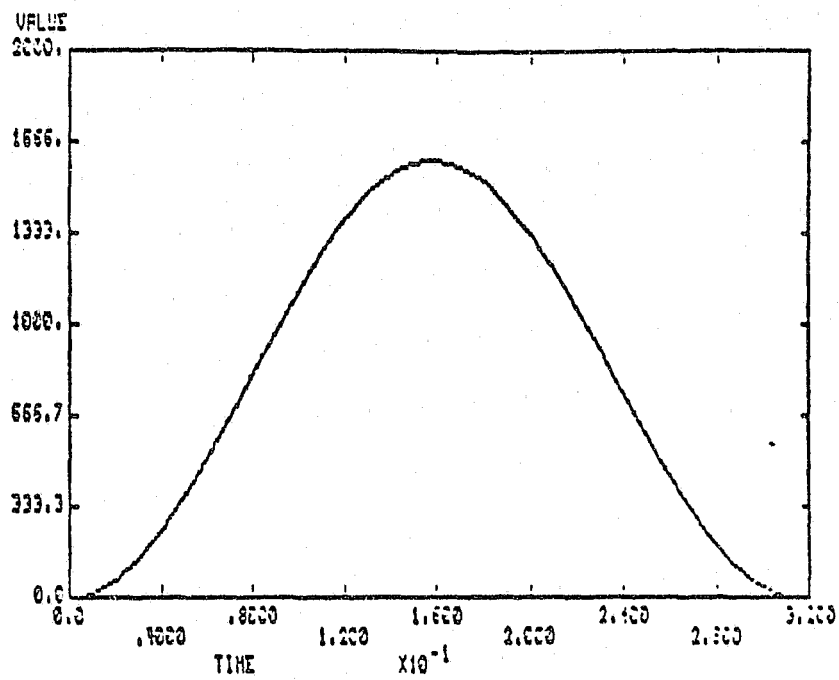
Fig. 2.7-3 The Hanning window along with its Fourier transform.
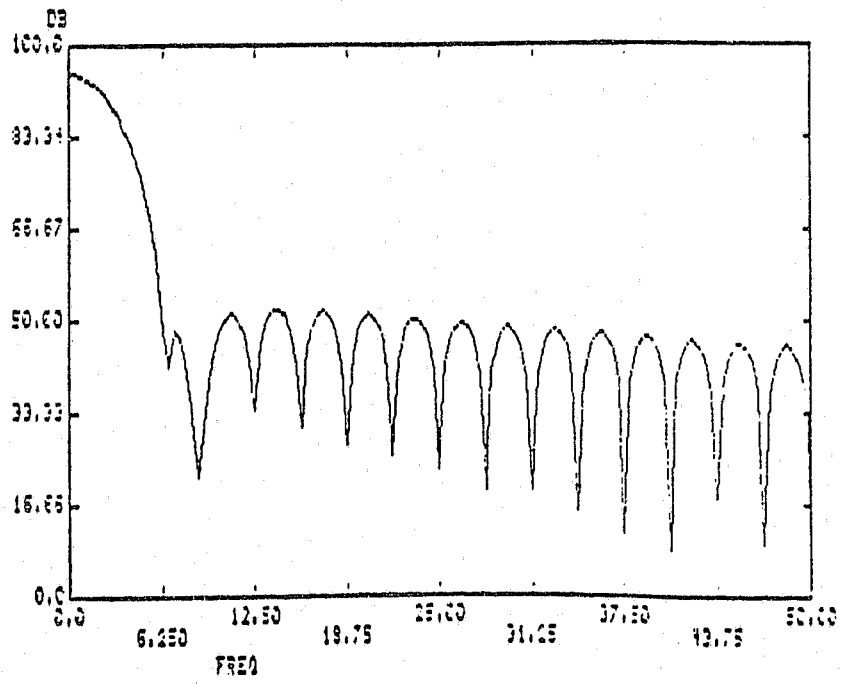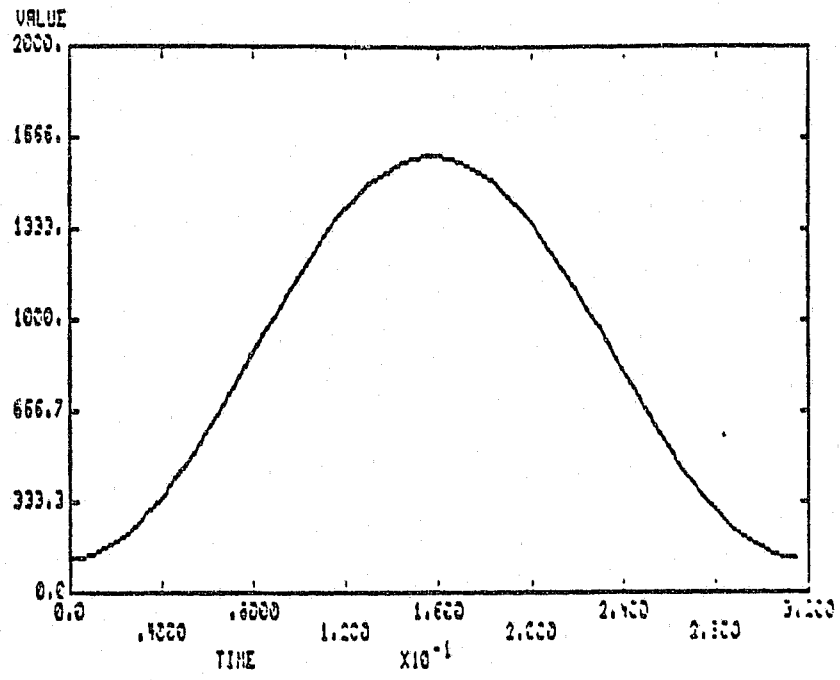
Fig. 2.7-4 The Hamming window along with its Fourier transform.

VALUE
2000.

1666.

1333.

1000.

666.7

333.3

0.0

TIME   X10⁻¹

DB
100.0

83.34

66.67

50.00

33.33

16.66

0.0

FREQ
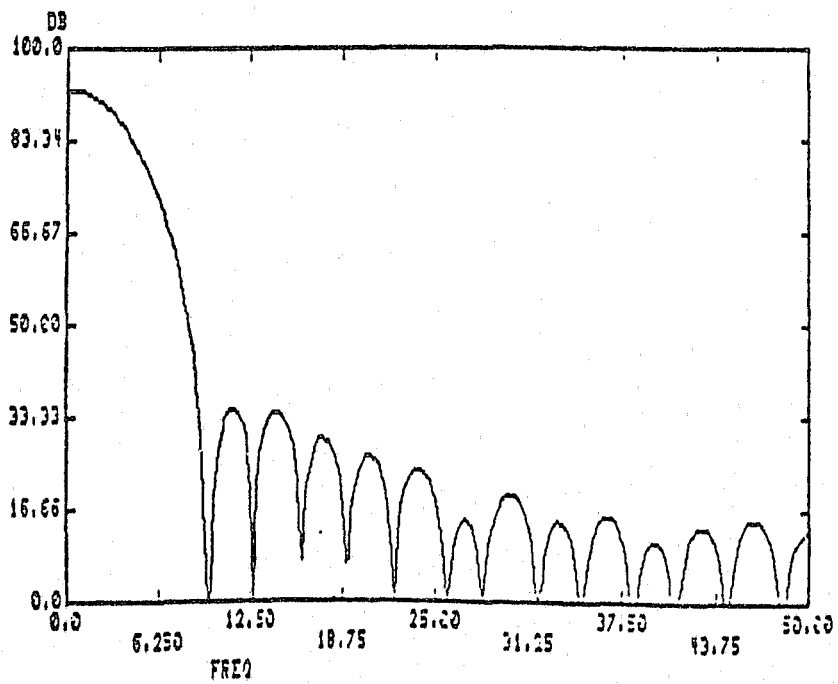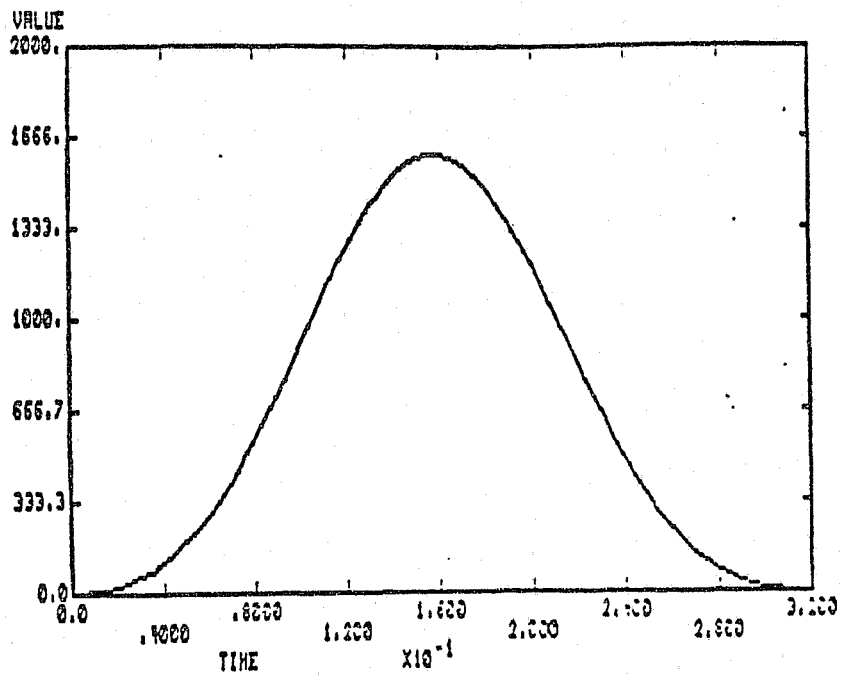
Fig. 2.7-5 The Blackman window along with its Fourier transform.

Window Function	3 dB Bandwidth	Peak Ripple	Asymptotic Decay
Rectangular (Box-car)	0.85 1/T	-13 dB	6 dB/oct.
Bartlett (Triangular)	1.25 1/T	-26 dB	12 dB/oct.
Hanning (Raised-cosine)	1.40 1/T	-32 dB	18 dB/oct.
Hamming	1.30 1/T	-43 dB	6 dB/oct.
Blackman	1.68 1/T	-58 dB	18 dB/oct.

Note: T is the length of the time window.

Table 2.7-1 Characteristics of some common symmetric windows.

All the windows presented thus far have been symmetric windows. That is, all of the windows exactly match if folded about their center point. These windows were designed to reduce the leakage effects of data that is present throughout the time window. However, many data signals are transient in nature and die out before the end of the time window. In addition, if the input data has a large damping constant, many of the symmetric windows greatly reduce the amount of data and therefore energy that is available to analyze as shown in Fig. 2.7-6. Furthermore, if the signal is in the presence of noise, not only is much of the input signal blocked, but much of the noise is allowed to pass when the signal-to-noise ratio is very low. To decrease the effects of noise on transient data, non-symmetric windows offer an advantage over symmetric windows.

A common window used for transient data is the exponential window shown in Fig. 2.7-7. The exponential window allows most of the data to pass at the begining of the time window, but blocks the signal at the end of the time window. However, the exponential window allows for a possibly large transition to be present if the input signal does not have zero amplitude at the beginning of the time window. That is, a large transition may be produced when the input signal is assumed to be periodic by the DFT as shown in Fig. 2.7-8. Therefore, exponentially damped windows were developed which have an initial value of zero, exponentially increase and then exponentially decrease

such that most of a transient input is allowed to pass the window while any noise that was present at the end of the time window is blocked. One such window which has the same form as the Rayleigh distribution is expressed by the equation:

$$w(n) = (n - 1) * \exp(-1 * A * (n - B))$$ (1)

where A is the damping constant and B is an offset value.

The Rayliegh window along with its Fourier transform is shown in Fig. 2.7-9.

A second exponential window was developed from the Rayliegh window such that the slope of the window near the beginning of the time window is zero and then increased in an exponential manner as the Rayliegh window. This window along with its transform is shown in Fig. 2.7-10 and will be referred to as the modified Rayliegh window. The modified Rayliegh window is expressed by the equation:
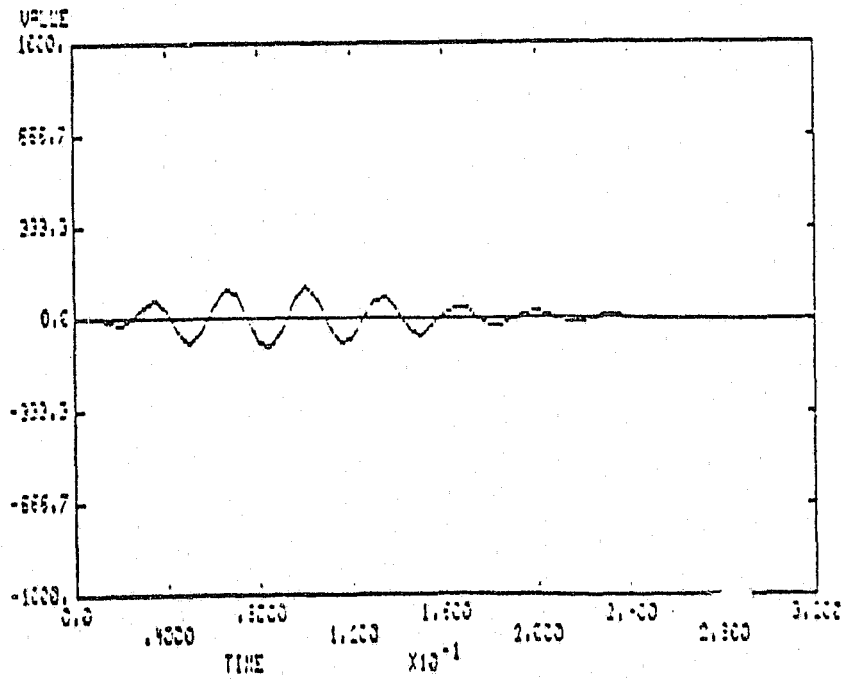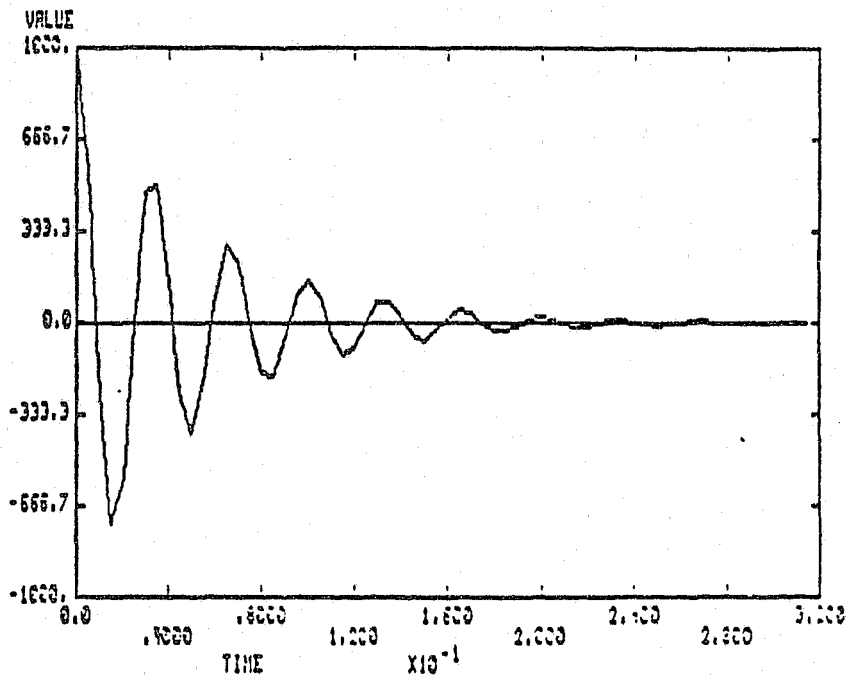
Fig. 2.7-6   Result of using a Hanning window on transient data.

[f(t) = 1000 cos(30t + 90) e^{-3t}].

64
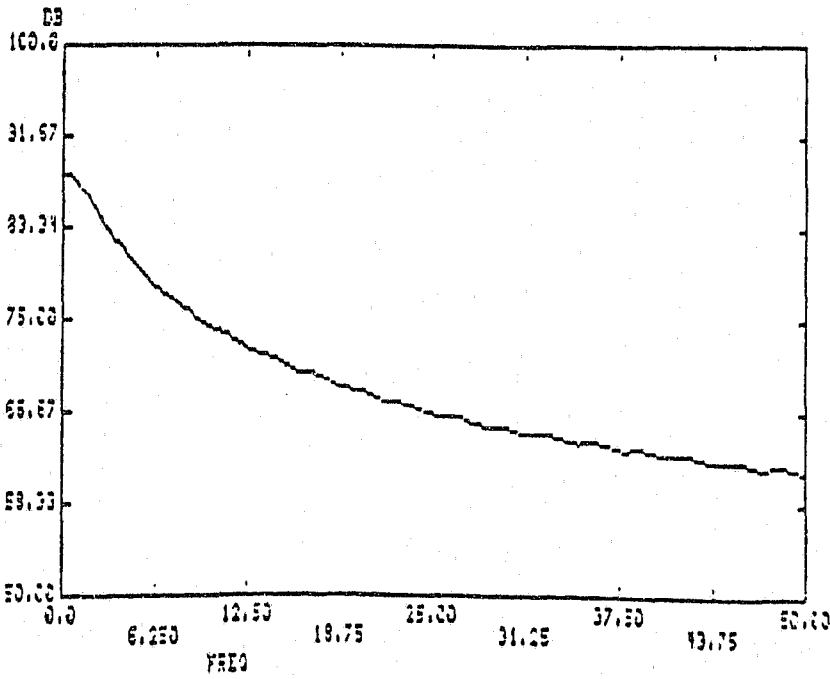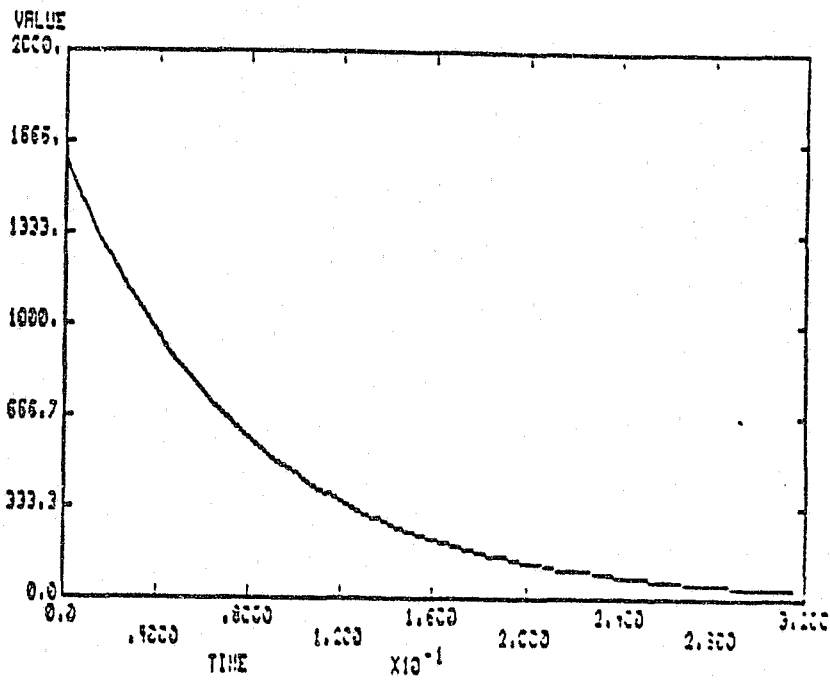
Fig. 2.7-7   Exponential window along with its Fourier transform.
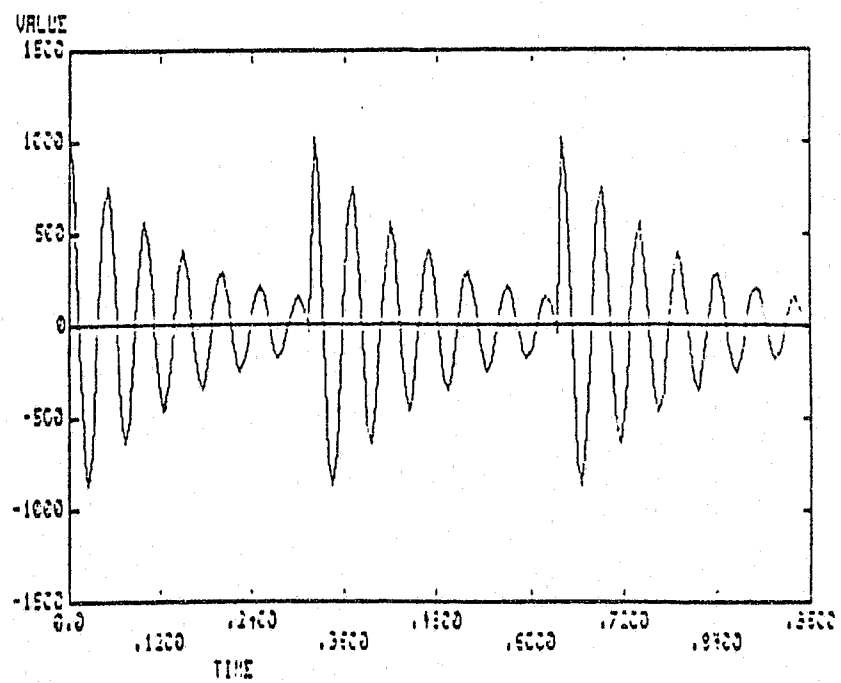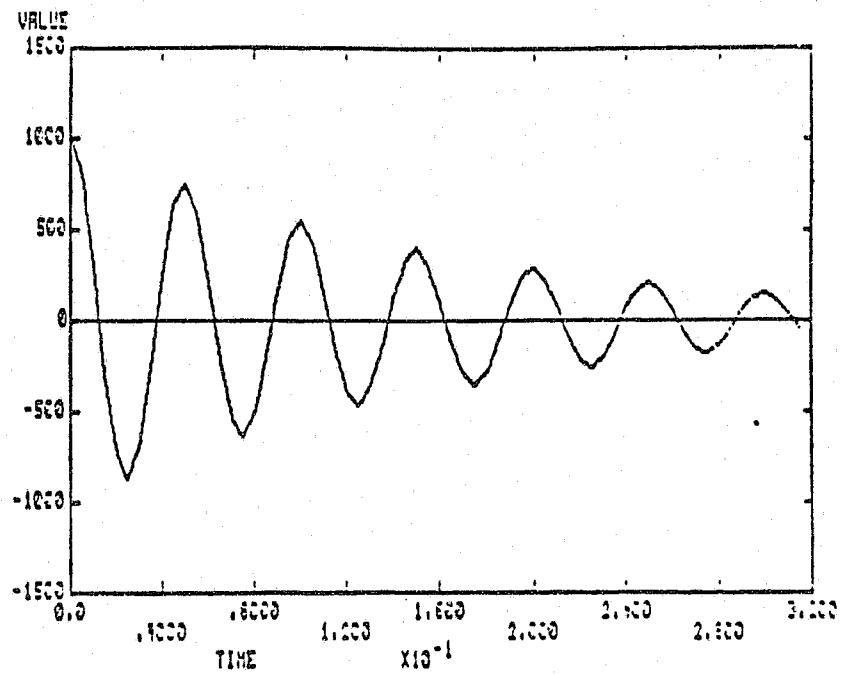
Fig. 2.7-8   Periodically extended damp sine wave with a 90 degree phase shift.
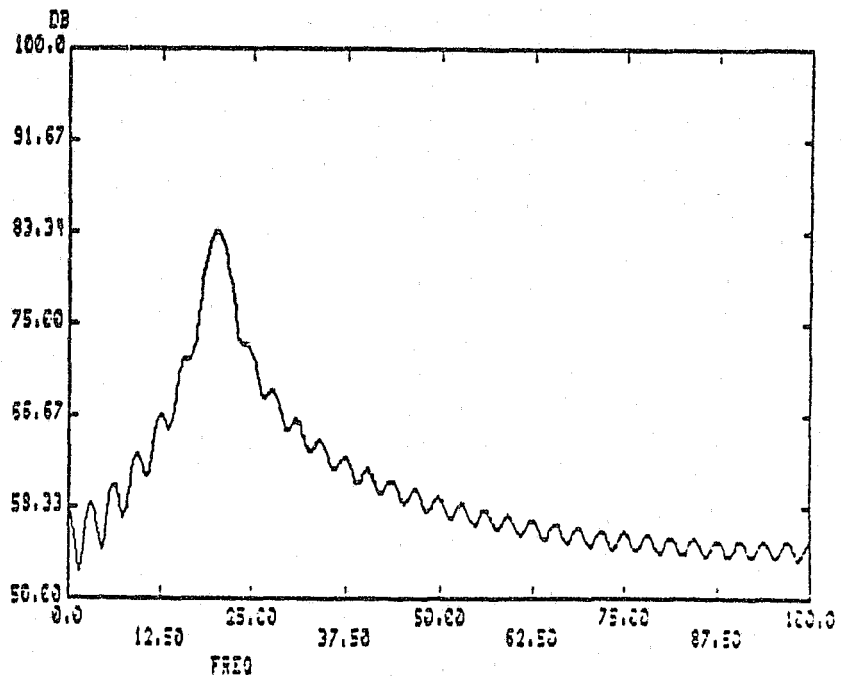
Fig. 2.7-8   Periodically extended damp sine wave with a 90 degree phase shift

(Concluded)
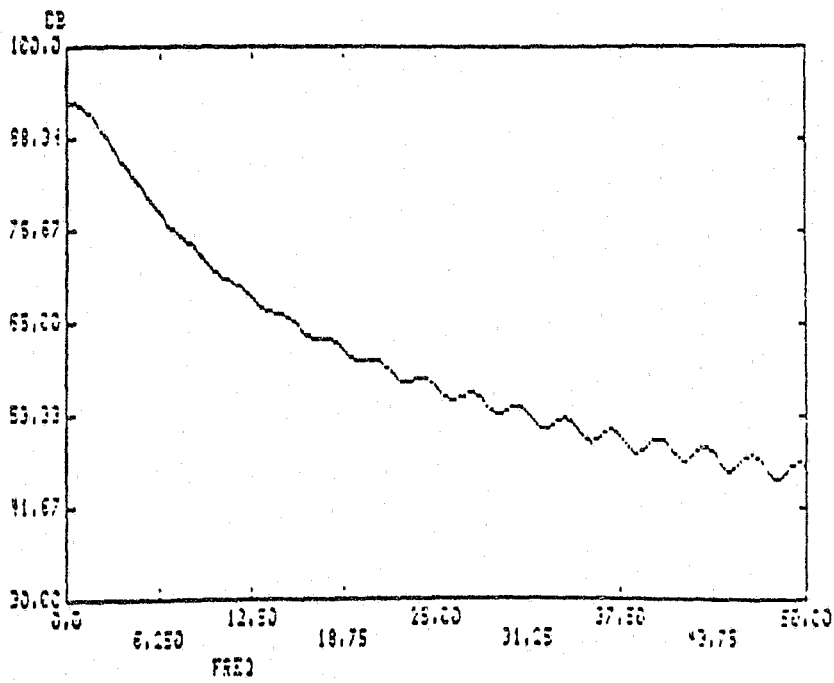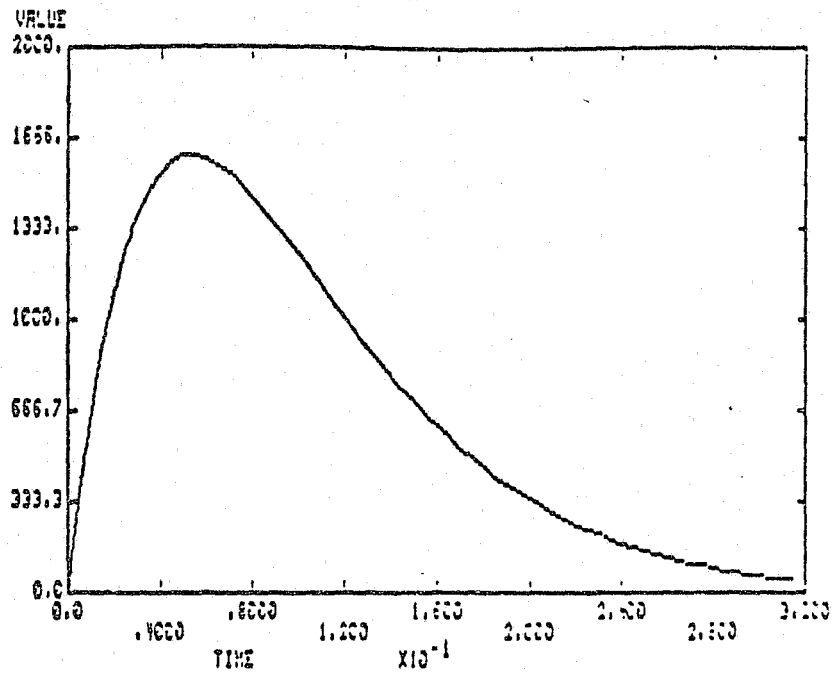
Fig. 2.7-9 Rayliegh window with its Fourier transform.

(A = 0.00015, B = -300).
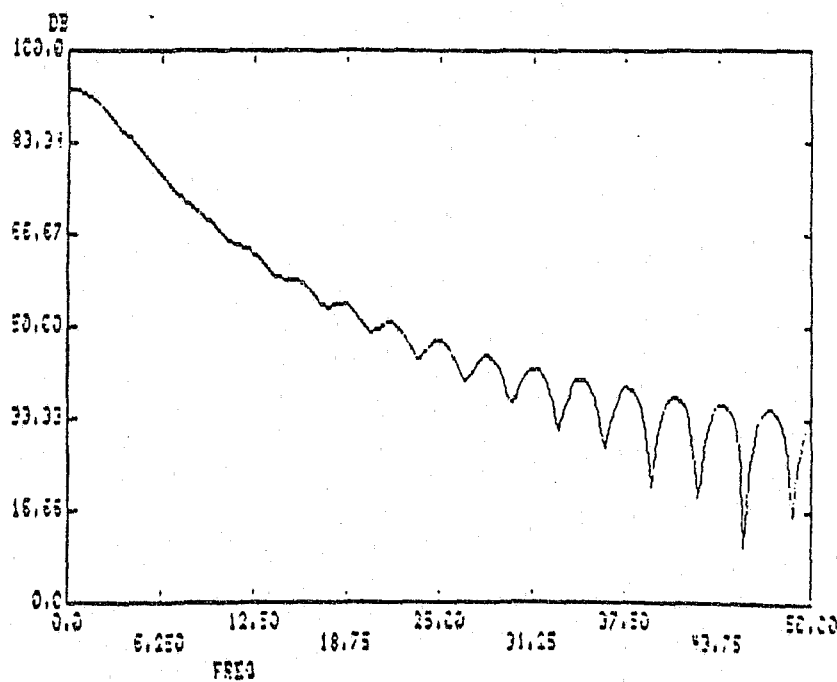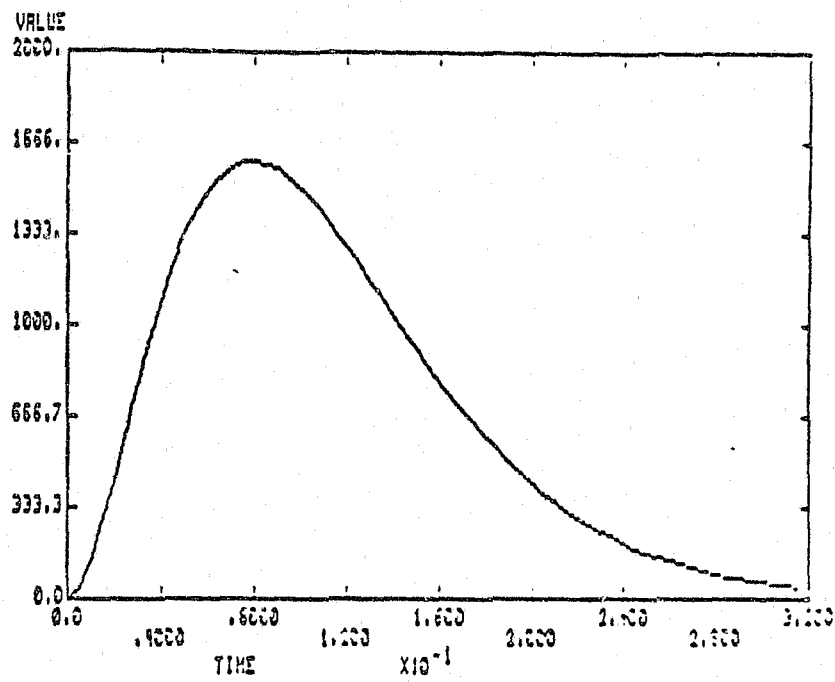
Fig. 2.7-10 Modified Rayliegh window with its Fourier transform.

(A = 0.0002,   B = -300).

$$w(n) = (n - 1) * \exp(-1 * A * (n - B))\qquad\qquad (2)$$

where A is again the damping constant and B is an offset.

The exponential windows (i.e., the Rayliegh and Modified Rayliegh) tend to have greater main lobes in the DFT due to the limiting of the time record by the windows. That is, the windows limit the time records to a greater extend than the symmetric windows which causes the frequency spectrum to spread-out. In addition, the exponential windows do not truncate the Fourier coefficients at the beginning of the time record as smoothly as many of the symmetric windows to reduce the side lobes in the transform.

In the presence of noise, the exponential windows allow more of the signal to pass at the beginning of the time window and block-out the noise when the signal has damped-out. The symmetric windows give the same weight to data at the beginning of the time record as to data at the end. With exponentially damped data, the input signal may only be distinguishable from the noise at the beginning of the time record. Thus, the symmetric windows do not effectively attenuate the noise at the end of a time record when the data signal is highly damped. The exponential windows allow more of the signal to pass at the beginning of the time record and attenuate the noise at the end of the time window in order to decrease the effects of the noise in the DFT.

From observing the effects of symmetric windows on damped data, the resultant waveform data used in the DFT calculation has much less amplitude than when using an exponential window (especially when the data is heavily damped). Since the input data loses a lot of its amplitude, noise affects the DFT to a much greater extent. When not in the presence of noise, the exponential windows allow for a DFT of greater magnitude, but less frequency resolution. The side lobes of the exponential windows are greater than those of most of the symmetric windows.

The Fourier transforms of the exponential window with different damping constants was also investigated. A very lightly damped exponential has very much the

same frequency characteristics as a rectangular window (see Fig. 2.7-11). As the damping constant is increased, the frequency response spreads out over a larger range of frequencies. The exponential window has side lobes much like the rectangular window which are present until the exponential window becomes critically damped (i.e., the window just goes to zero at the end of the time window). For a critically damped exponential window, the frequency response of the window has spread to a point that the side lobes are "buried" and are not visible in the transform as shown in Fig. 2.7-12. As the damping constant is increased past the critically damped point, the frequency response of the window continues to spread out (without rippling) (see Fig. 2.7-13). Taking the damping constant increasingly larger causes the exponential to look more and more like an impulse in the time domain which corresponds to a flat frequency spectrum.

In order to show the effects of different windows on transient data, several wave forms were "captured" by the HP-3561A Dynamic Signal Analyzer. The damped sinusoidal data was generated by observing the resonance frequencies of a 3/4 inch long cylinder (inside diameter = 1/4 inch, outside diameter = 1/2 inch). The cylinder was excited by dropping bee-bees on it, and the resonance frequencies were determined using a Polaroid ultrasonic transducer to convert the sound waves produced by the vibrating cylinder to an electric signal. The HP-3561A signal analyzer was used to sample the electric signals and to store the signals in memory. The wave forms were then read out of the analyzer's memory using a Texas Instrument Business-Pro computer. Finally, the signals were windowed with several different windows, and the discrete Fourier transforms of the wave forms were calculated. The wave forms were windowed using software called Interactive Laboratory System Simulation (ILS-IEEE).
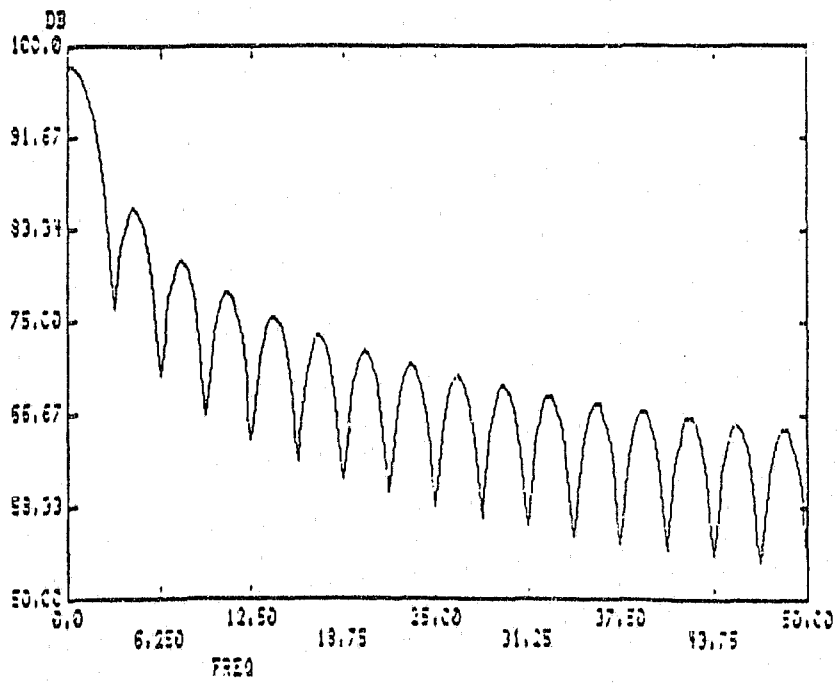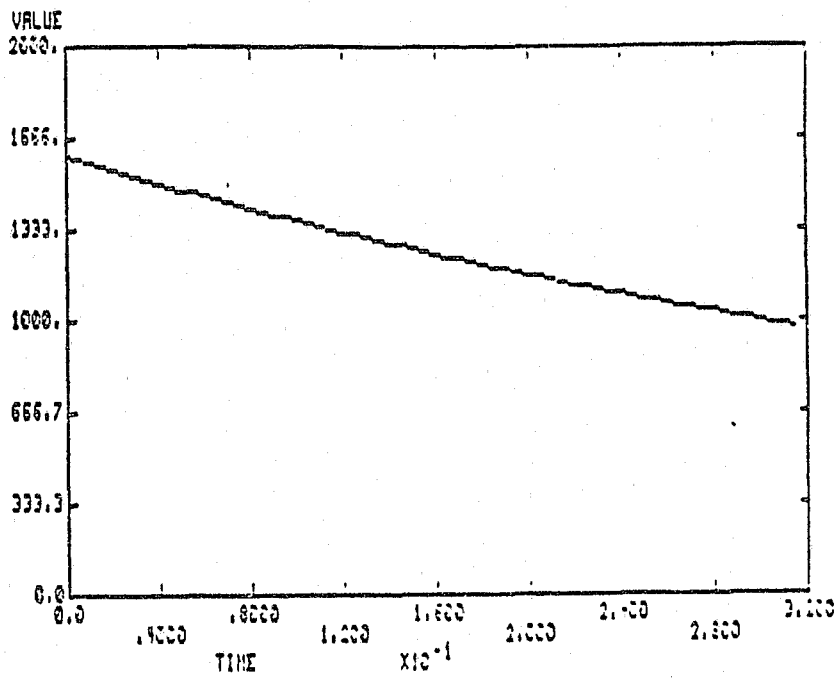
Fig. 2.7-11 Lightly damped exponential window with its Fourier transform.
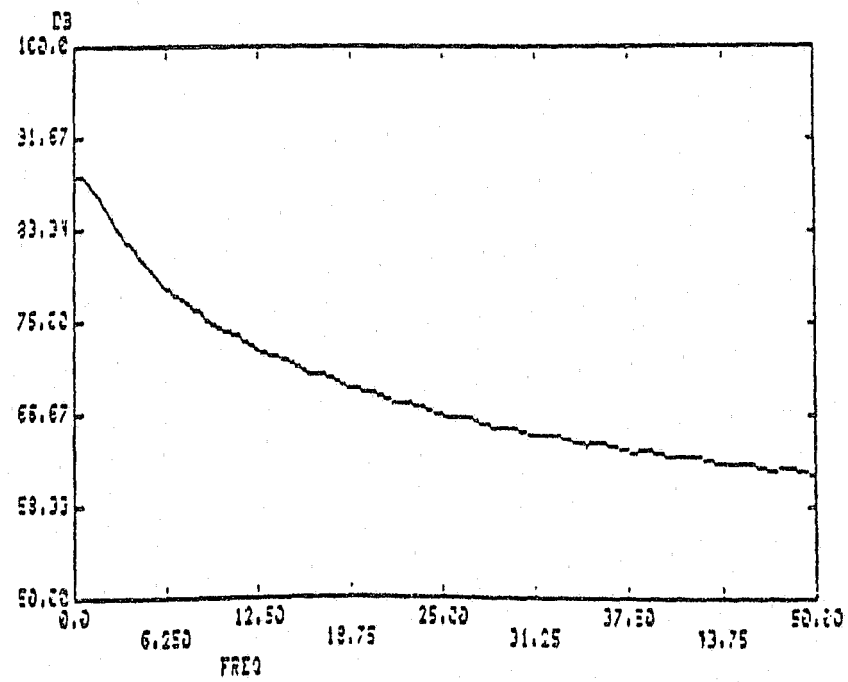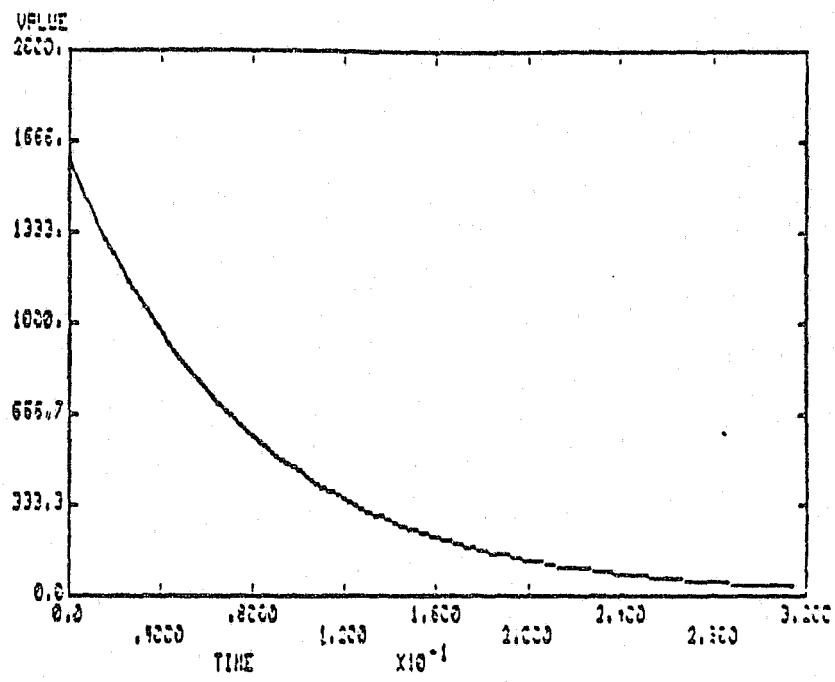
Fig. 2.7-12 Critically damped exponential window with its Fourier transform.
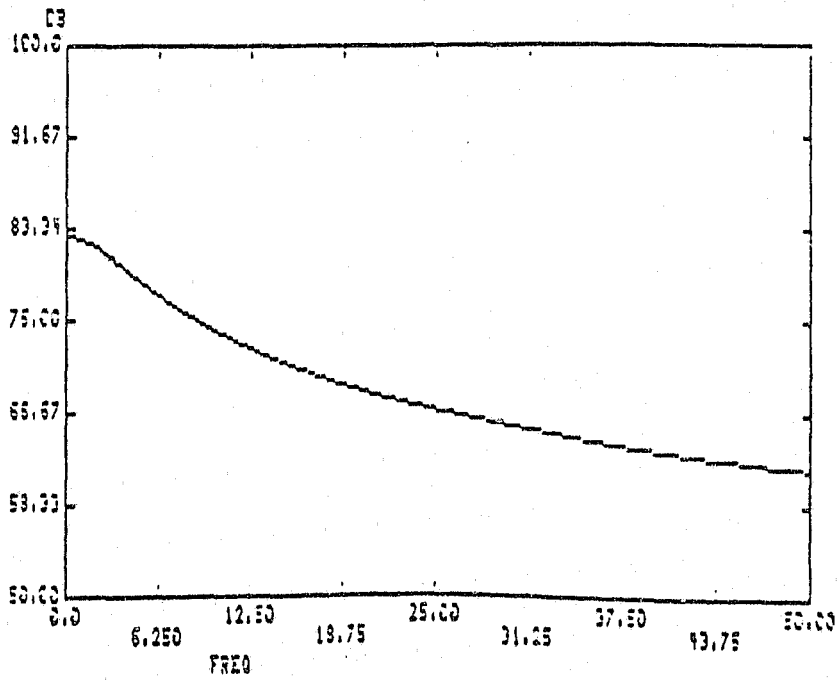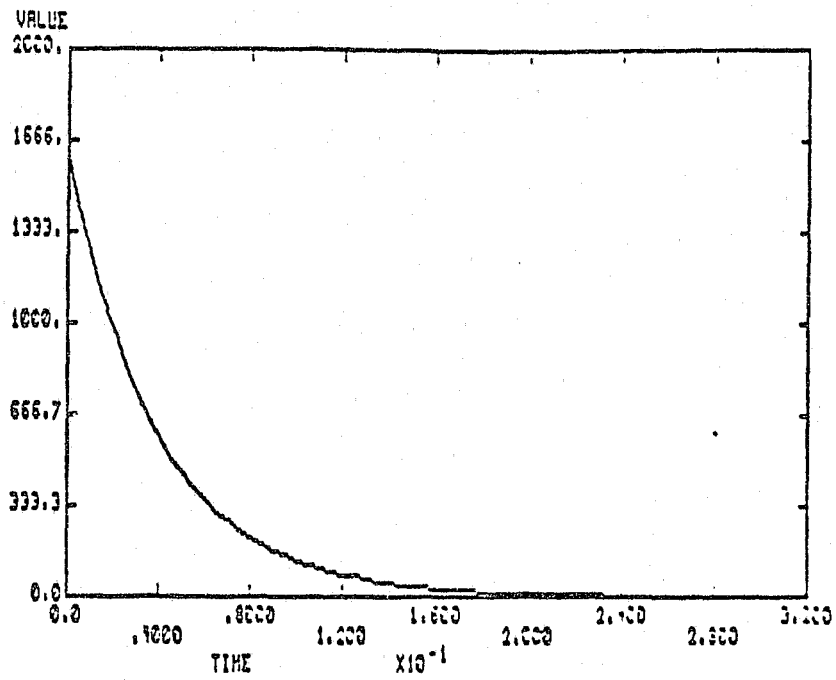
Fig. 2.7-13   Heavily damped exponential window with its Fourier transform.

A typical signal obtained from the excitation of the cylinder is shown in Fig. 2.7-14. As can be seen from this figure, the vibration modes of the cylinder are highly damped. Also, from the discrete Fourier transform, the two main resonance frequencies of the cylinder are at 38.75 kHz and at 91.00 kHz. However, since this data has been windowed using the rectangular window (recall that observing a signal for a finite amount of time corresponds to windowing the data with a rectangular pulse equal to the time that the signal is observed), the effects of leakage may be significant in the discrete Fourier transform, and the transform may not give an accurate picture of all the resonance frequencies present in the cylinder. In order to reduce the leakage effects of the rectangular window, the data was windowed with the triangular window as shown in FIg. 2.7-15. As can be seen from the Fourier transform of the triangular windowed data, the leakage effects in the frequency spectrum have been reduced (especially around the frequency component at 38.75 kHz). By windowing the signal with the triangular window, an additional frequency component at 37.0 kHz can be seen much clearer due to the reduction of the leakage from the 38.75 kHz component. Note, however, that the magnitude of the main frequency components is reduced by approximately 5 dB while the signal to noise ratio remains virtually unchanged with a slight improvement using the triangular window..

The most common window used in digital signal acquisition is the Hanning window due to its balance in the trade-offs of main lobe width and magnitude of the side lobes of the window function. The input signal of Fig. 2.7-14 was windowed using the Hanning window and the time wave form and the resultant discrete Fourier transform are shown in Fig. 2.7-16. The Hanning window has much the same effects as the triangular window in the reduction of leakage, but the Hanning window has a narrower main lobe so the Fourier transform shows slightly better resolution of the frequency components. The finer resolution of the Fourier transform can again be seen by noticing the greater
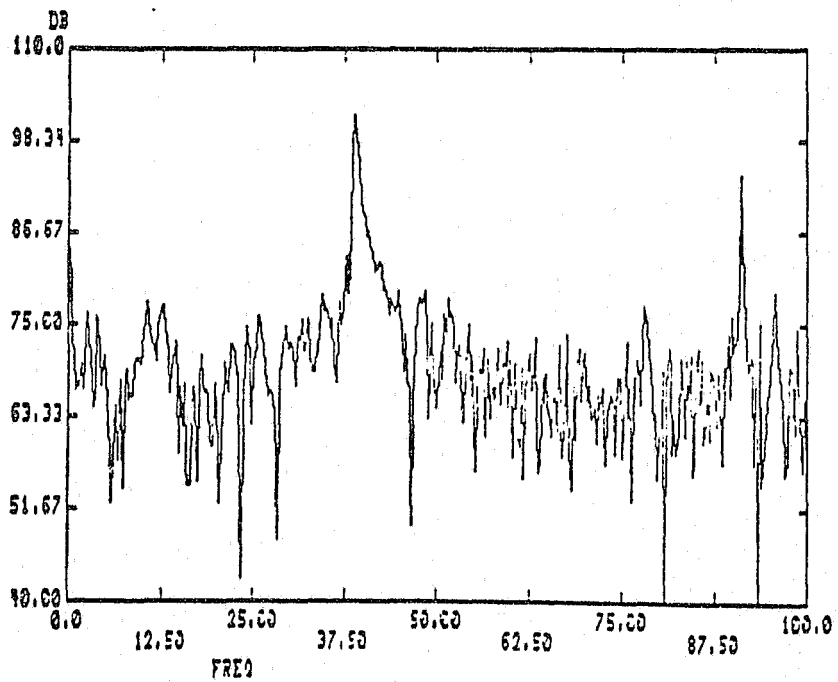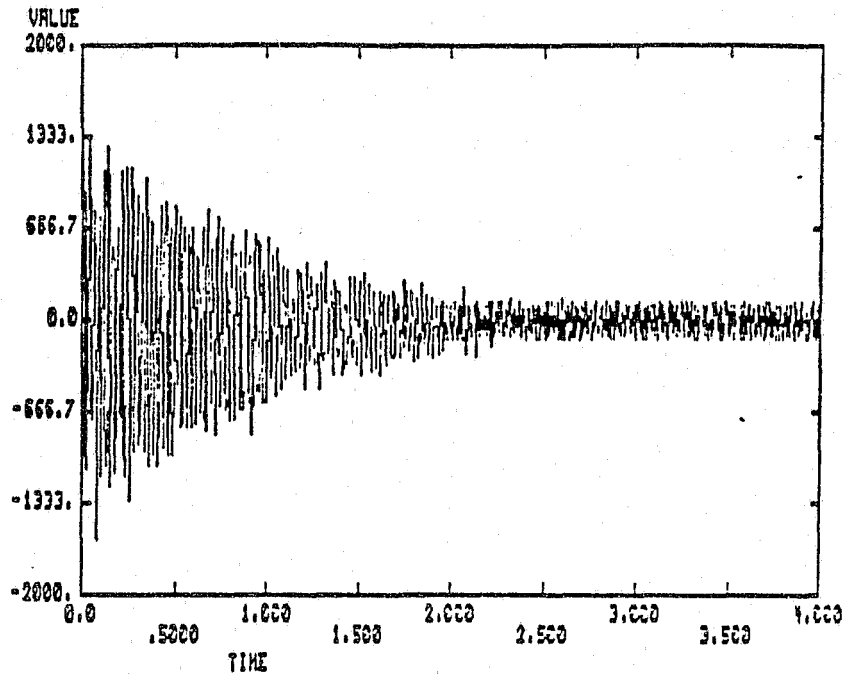
Fig. 2.7-14 Received signal from excitation of the cylinder and the discrete Fourier transform of the signal (time is in milli-seconds and frequency is in kilohertz).

76
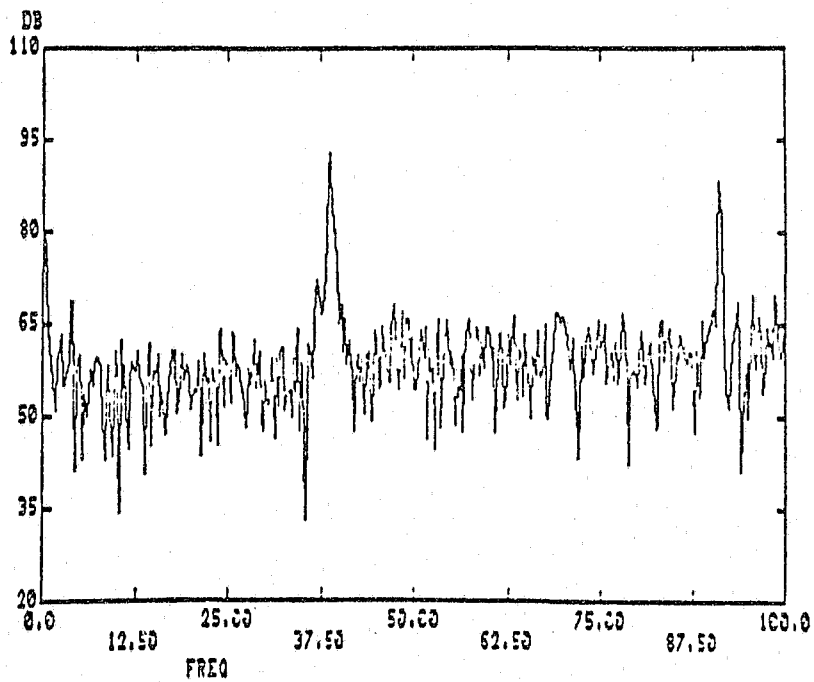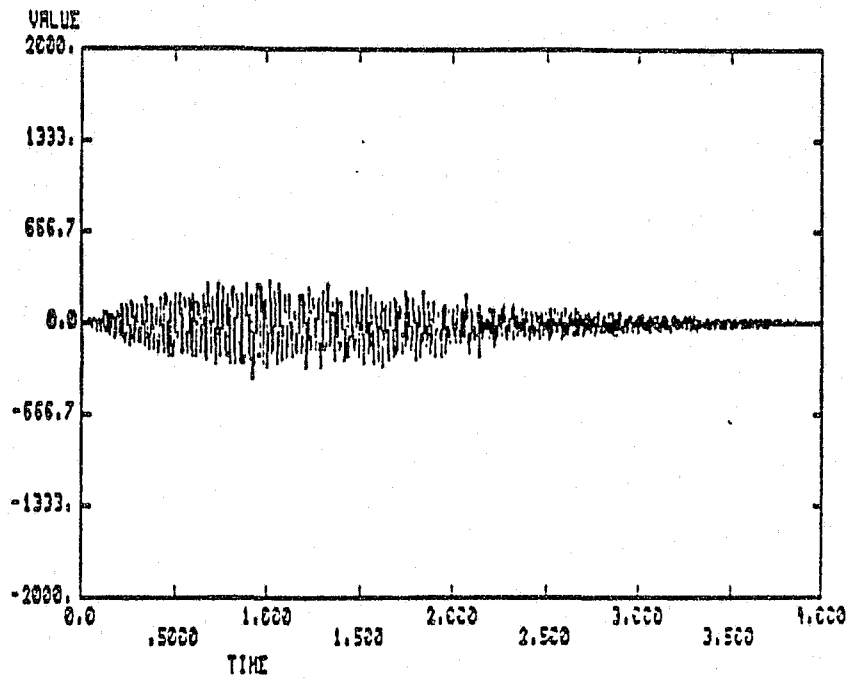
Fig. 2.7-15 Time trace and discrete Fourier transform of the received signal of Fig. 2.7-14 multiplied by a triangular window [time (ms), frequency (kHz)].

77
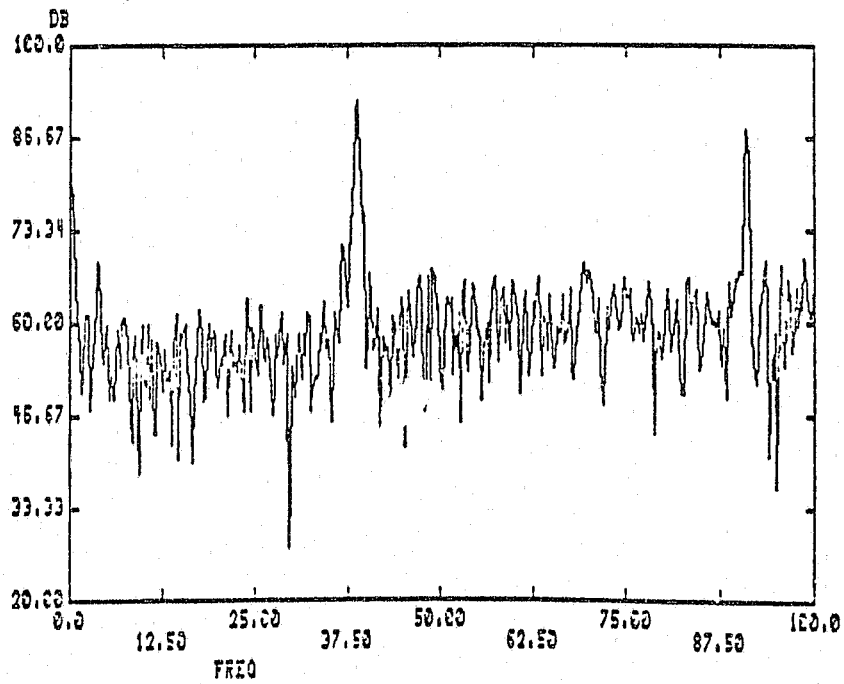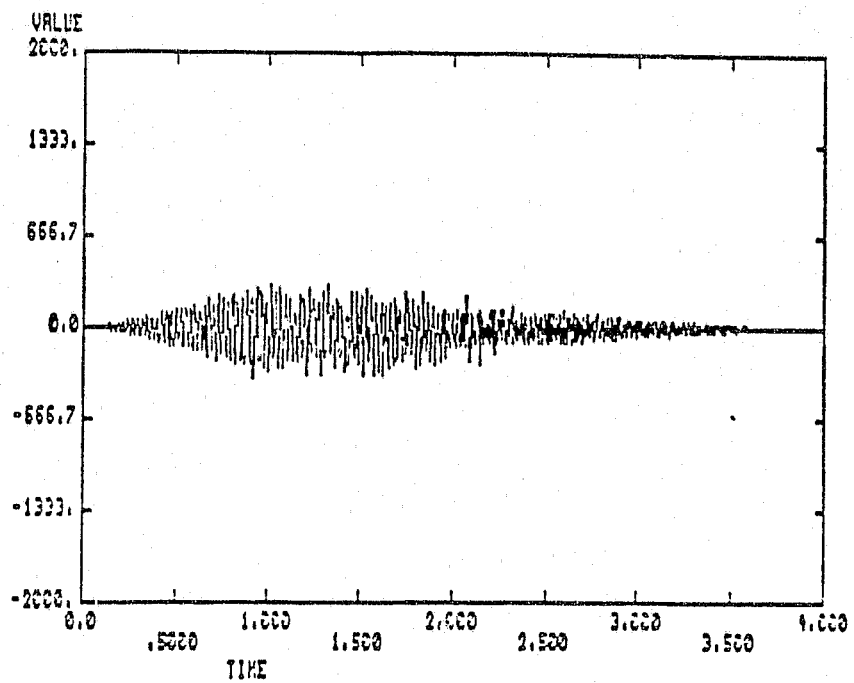
Fig. 2.7-16 Time trace and discrete Fourier transform of the recieved signal of Fig. 2.7-14 multiplied by a Hanning window [time (ms), frequency (kHz)].

separation of the two frequency components around 37.0 kHz. Again the signal to noise ratio is virtually unchanged.

As a final example of windowing transient data with symmetric windows, the wave form of Fig. 2.7-14 was windowed with the Hamming window as shown in Fig. 2.7-17. The discrete Fourier transform of the windowed data shows much the same characteristics as the triangular and Hanning windows. The Hamming window does show a slight decrease in the resolution in the Fourier transform compared to the Hanning window as expected from the Hamming windows wider main lobe. The Hamming window has much the same characteristics as the triangular window as can be seen by comparing the Fourier transforms of Figs. 2.7-15 and 2.7-17.

The input signal was then analyzed using the critically damped exponential window. Figure 2.7-18 shows the input signal of Fig. 2.7-14 windowed by a critically damped exponential window and the resultant discrete Fourier transform. The exponential window significantly reduces the resolution in the Fourier transform due to the wide main lobe and high side lobe levels of the exponential window. As can be seen from the Fourier transform of the exponential windowed signal, the frequency component at 37.0 kHz is "buried" in the main lobe of the frequency component at 38.75 kHz. However, the magnitude of the frequency component at 38.75 kHz is approximately 3.75 dB greater than the same component in the Hanning window. On the other hand, the magnitude of the frequency component at 91.0 kHz is approximately 3.3 dB down in the exponential windowed signal from the Hanning windowed signal. The reason that the magnitude of the 91.0 kHz frequency component decreased is due to the time constant of this frequency component. Referring back to Fig. 2.7-14, the frequency spread of the 91.0 kHz component is less than the frequency spread of the 38.75 kHz component. The greater spread of the 38.75 kHz frequency suggest that this
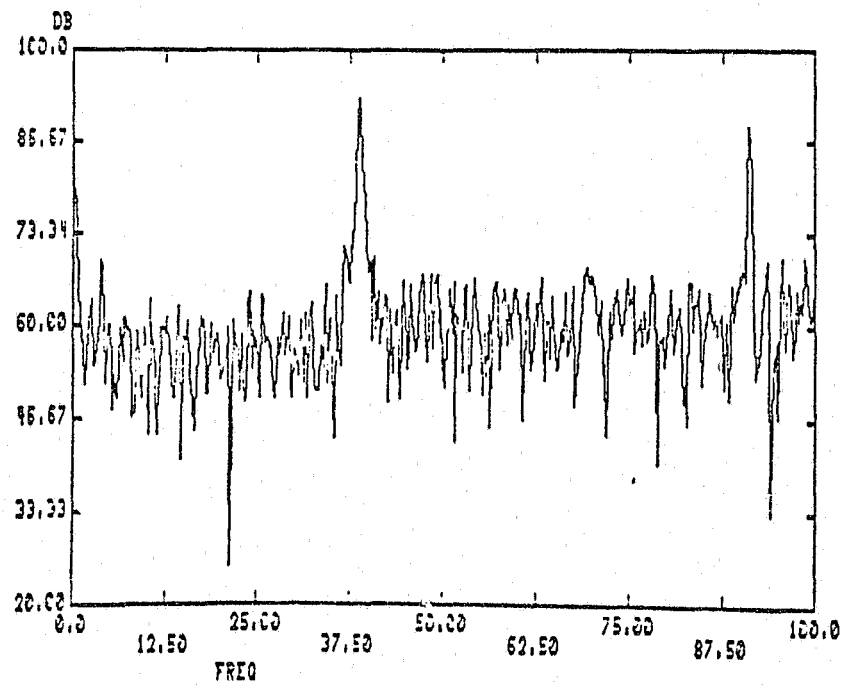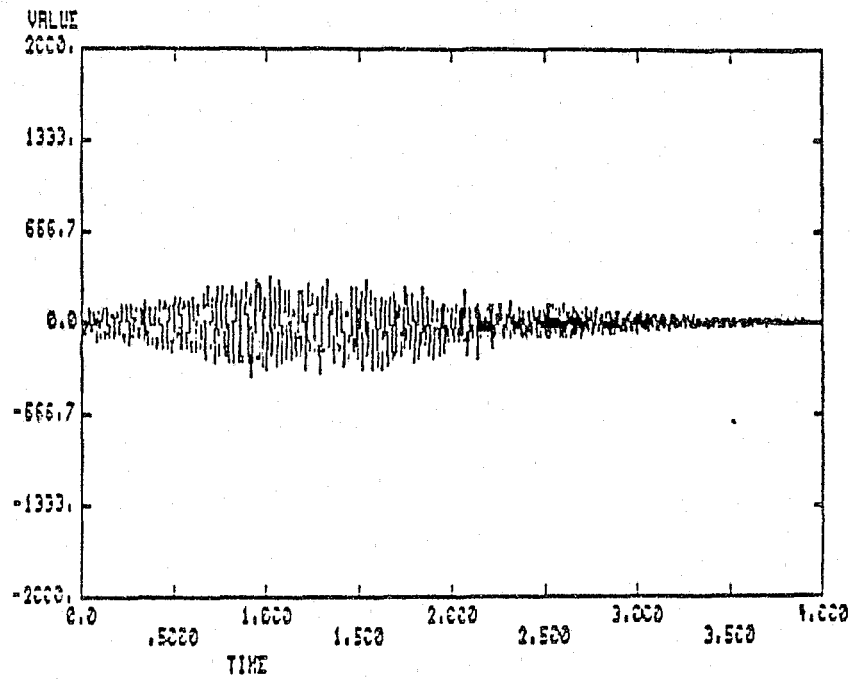
Fig. 2.7-17 Time trace and discrete Fourier transform of the received signal of Fig. 2.7-14 multiplied by a Hamming window [time (ms), frequency (kHz)].
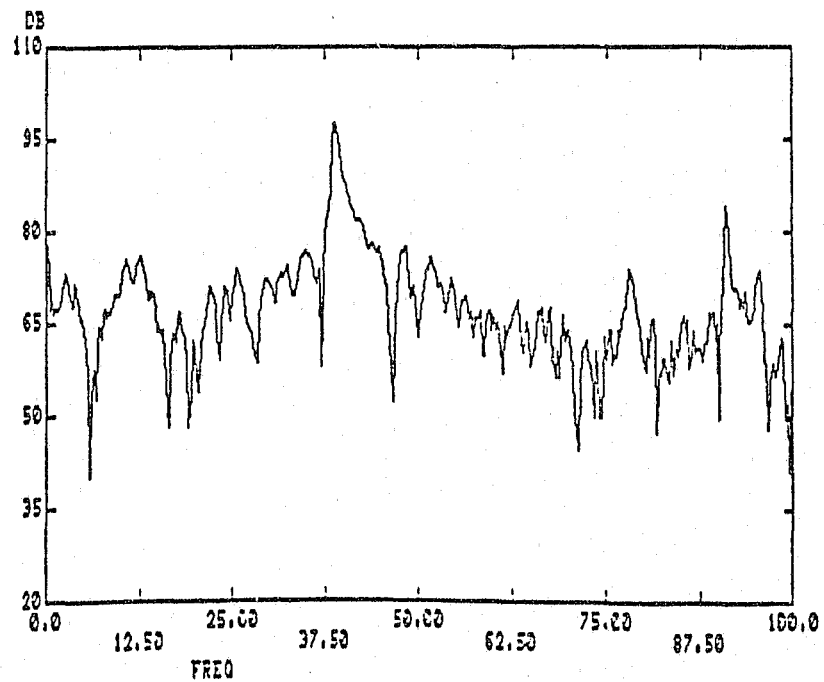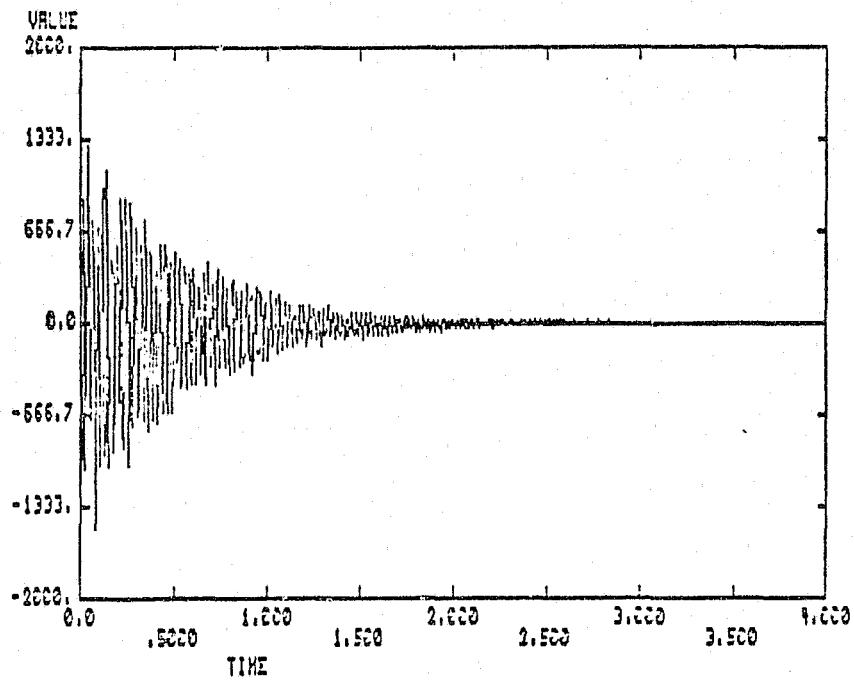
Fig. 2.7-18 Time trace and discrete Fourier transform of the received signal of Fig. 2.7-14 multiplied by a critically damped exponential window [time (ms), frequency (kHz)].

component has a smaller time constant than the 91.0 kHz frequency. Therefore, the exponential window actually decreases the amount of the 91.0 kHz frequency signal that is allowed to pass through the exponential window. On the other hand, several frequency components that were apparent in the rectangular windowed signal and are not noticeable when the symmetric windows are used appear when the exponential window is applied to the received signal.

As an example of the different effects of the symmetric windows versus the exponential window, consider the frequency components at 10.75 kHz and 10.50 kHz. These frequencies can be easily seen in the Fourier transform of both the rectangular and exponential window, but cannot be seen in the transforms of any of the symmetric windows As can be seen from the Fourier transform of Fig. 2.7-14, the frequency components at 10.75 kHz and 12.50 kHz are spread out in the frequency spectrum suggesting that these frequencies are highly damped. Since these frequencies are highly damped, the symmetric windows do not allow much of the signal at these frequencies to pass while the exponential window allows almost all of the signal to pass the windowing process thus allowing these frequencies to have a greater magnitude in the frequency spectrum. However, the frequency resolution is greatly decreased when the exponential window is used due to the wide main lobe of the exponential window's frequency transform. The wide main lobe gives the Fourier transform of the received signal a smooth effect since the main lobe of each of the frequency components of the signal are spread over a range of frequencies.

Next, the Rayliegh and modified Rayliegh windows were used to window the received signal. The Fourier transforms of both of these windows are very similar as can be seen in Figs. 2.7-19 and 2.7-20. The frequency resolution of these windows is
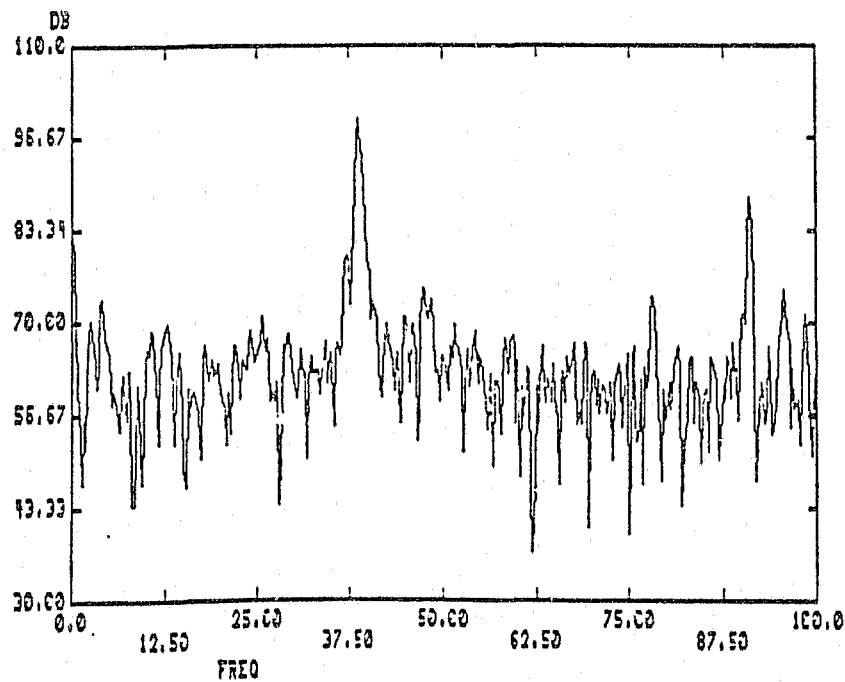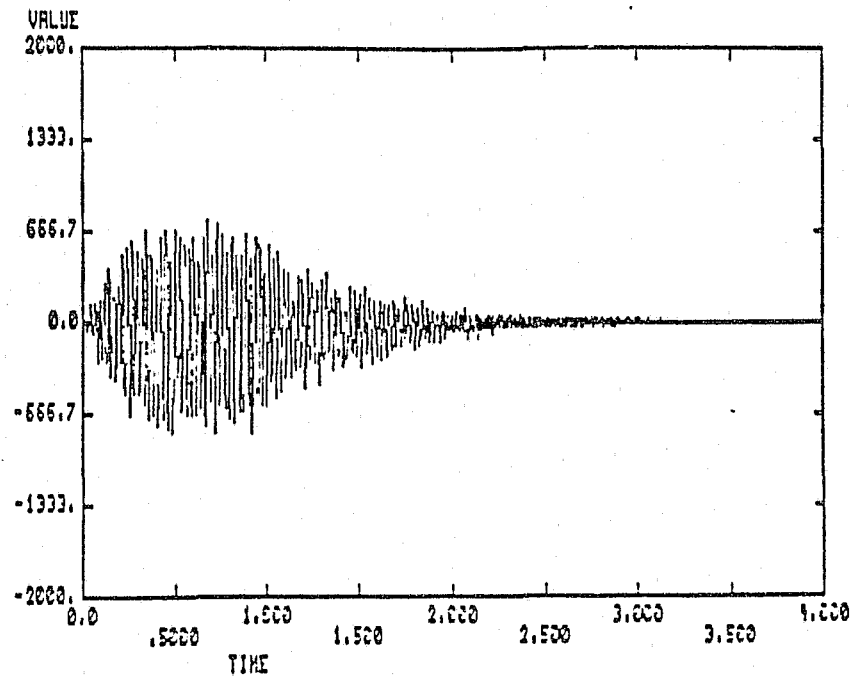
Fig. 2.7-19 Time trace and discrete Fourier transform of the received signal of Fig. 2.7-14 multiplied by a Rayliegh window [time (ms), frequency (kHz)].
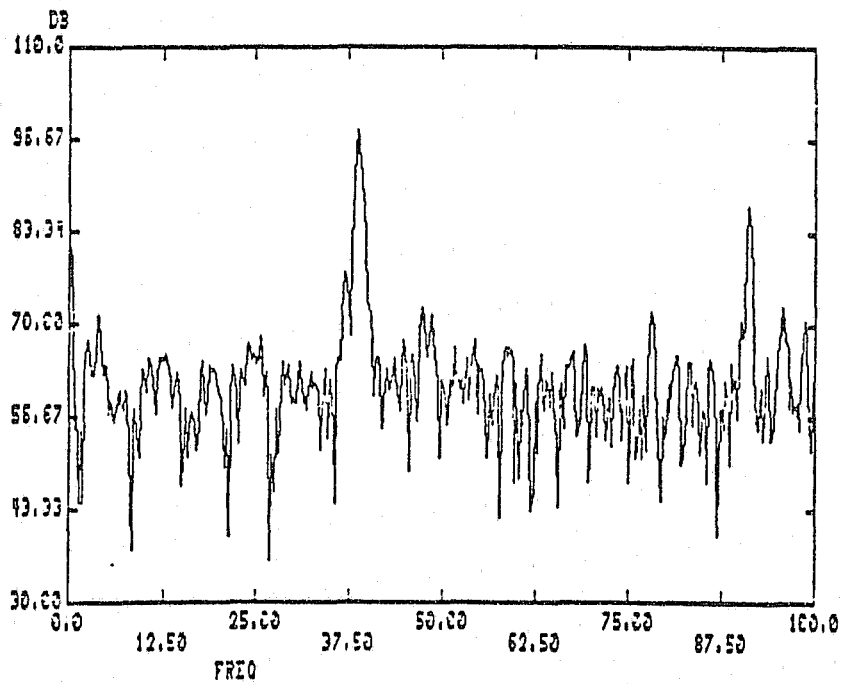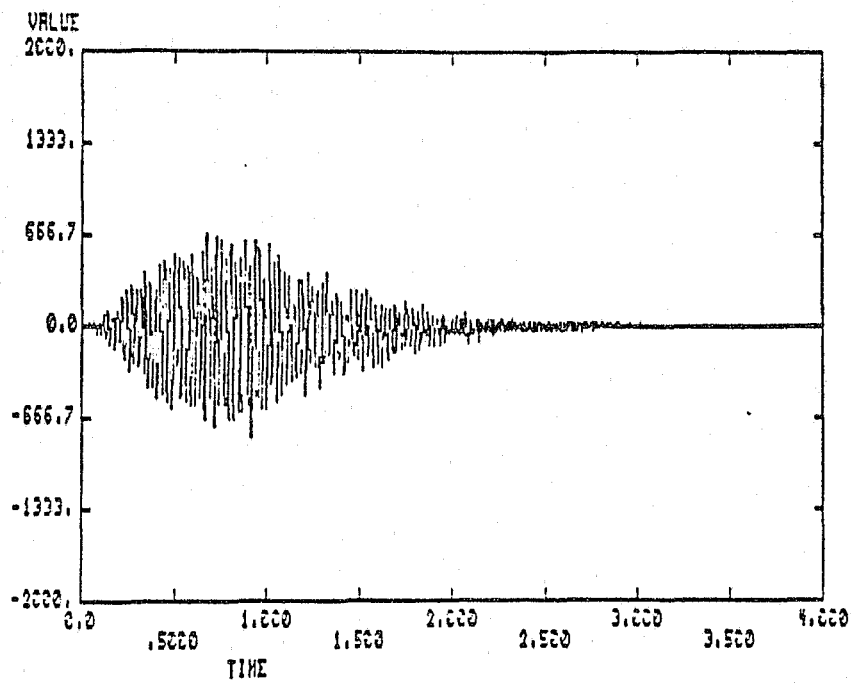
Fig. 2.7-20 Time trace and discrete Fourier transform of the received signal of Fig. 2.7-14 multiplied by a modified Rayliegh window [time (ms), frequency (kHz)].

84

considerably improved from the exponential window. The Fourier transforms of the Rayliegh and modified Rayliegh windows do not have as great a smoothing effect as the exponential window. Also notice the frequency components are better separated and the frequency at 37.0 kHz is again noticeable in both the Fourier transforms using the Rayliegh and modified Rayliegh windows. The Modified Rayliegh window has slightly better resolution than the Rayliegh window, but both transforms show approximately the same frequency components present in the received signal. The only variation in the two transforms appears at the frequencies at 10.75 kHz and 12.50 kHz. Since these frequencies are highly damped as previously determined, the modified Rayliegh window blocks much of these components through the windowing process and the magnitude of these frequencies is slightly less (3 db) in the Modified Rayliegh window's transform compared to the Rayliegh window's transform. Also of interest is the frequency component at 78.0 kHz which can be seen when the received signal is windowed with the rectangular window (see Fig. 2.7-14) and in all three of the exponential windowed signals (that is, critically damped exponential, Rayliegh and Modified Rayliegh windows) but is not clearly present in any of the symmetric windows. Again, since this frequency component is relatively spread when the rectangular window is used, this component has a small time constant and decays rapidly. Therefore, the symmetric windows do not allow much of the signal at this frequency to pass and the frequency component at 78.0 kHz does not appear in the transforms of the symmetric windows.

Since the critically damped exponential window is very effective in separating the signal from the noise, differently damped exponential windows were used to window damped data with and without added noise. In the absence of noise the lightly damped exponential window has the best frequency response as expected (that is, the narrowest frequency spread, greatest amplitude of the input frequency and greatest attenuation of frequencies away from the input frequency). As the damping was increased, the main

lobe of the input frequency spread to adjacent frequencies and there is less resolution in the frequency spectrum.

When adding noise to damped data, the higher damped exponential windows show better noise rejection than the lighter damped exponential windows. The lightly damped exponential windows still have the same characteristics (that is, narrow main lobe, greater main lobe amplitude and greater attenuation of adjacent frequencies), but allow noise to pass after the input signal has damped to a small amplitude compared to the noise. Therefore, the lightly damped window allows the input signal (damped sine wave with noise) to pass with only light attenuation even when the signal to noise ratio has decreased significantly compared to the beginning of the time window. As the damping constant is increased, the exponential window attenuates the input data to a greater extent when the signal to noise ratio decreases at the end of the time window. Therefore, the frequency spectrum shows a greater signal to noise ratio at the expense of a greater main lobe spread. As the damping constant is continually increased, however, the noise rejection effect of the exponential window is overtaken by the spreading effects of the highly damped exponential. Therefore, there is an optimum damping constant for a given damped input signal. (As the exponential is increased, the noise in the frequency spectrum is smoothed due to the leakage characteristics of the higher damped exponential windows). The best window appears to be a window that matches the general shape of the input data (i.e., the same damping constant of an exponential window as the damped input data) for the maximum noise rejection and best spectral estimation.

In experimenting with damped sine wave data, the results show that the best window is one that has the same characteristics as the input data (that is, the same general shape). Without noise added to the input data, the Hanning window gives a Fourier spectrum with the least leakage while the Rayliegh and modified Rayliegh windows produce transforms that have slightly more spread than the rectangular

86

window. The exponential window's spectrum has the greatest spread as expected. The greater the damping constant used in either the exponential, Rayliegh, or modified Rayliegh windows, the greater the spread in the Fourier transform.

For higher damped signals especially in the presence of noise, the signal blocking effects of the symmetric windows becomes more significant and the ability to detect the resonance frequencies of the signal decreases. Therefore, the critically damped exponential, Rayliegh and modified Rayliegh windows are needed to separate the signal from the noise. In the presence of noise, the exponential window has the best spectrum for exponentially damped data using the Fourier Transform. The Hanning window attenuates the data at the beginning and the end of the time window, thus blocking much of the input signal at the beginning of the time window while allowing the noise to pass in the middle of the time window when the signal-to-noise ratio of the input data is less. The Rayligh and modified Rayliegh windows have the same type of effect on the input data, but to a lesser extent than the symmetric windows. Therefore, the Rayliegh and modified Rayliegh windows show improvement over the Hanning window. The exponential window, however, allows all the input signal to pass at the beginning of the time window when the signal to noise ratio is greatest and attenuates the data to a greater extent as the signal to noise ratio decreases. Therefore, even though the exponential window has the greatest spread in the Fourier transform, it also has the best noise rejection characteristics for exponentially damped data.

Task 2 (Senn and Bodenheimer)

The following is a description of the digital subsystem for target identification and is an adaptation of Chapter III of the Reference, *Senn, David L., "Automated Classification of Objects Through Ultrasound Signature Analysis," Master of Engineering Thesis, The University of Tennessee, Knoxville, Tennessee, March 1987 (Robert E. Bodenheimer, Major Professor).*

87

Hardware

Basic requirements imposed on the hardware are to sample at a 200 kHz rate, store the 1024 samples from the sampling process, compute four lines of the DFT, and classify the input. In order to achieve real time processing, the system must be able to make the computation and decision within the time it takes to stimulate the target and wait for the echos to die out. The amount of delay required is dependent on the environment which the system operates in. A typical delay allowed for the echos is 85 ms.

Several design alternatives are available. Among the choices are:

1. an off the shelf microcomputer system,

2. a mini-computer system;

3. a single board microprocessor system;

4. or a bit-slice design.

The path of least resistance would lead to a microcomputer or mini-computer with add-on circuitry to handle the high speed sampling. Unfortunately, project requirements prohibited the use of a micro/mini-computer system.

A bit-slice design would certainly provide a solution. However, this project does not have a bit-slice development system. Additionally, the development time with circuit design, board layout, construction, firmware coding, and debugging would most likely have exceeded the time allowed.

Thus, some type of microprocessor based design was required. Within the past few years several special purpose microprocessors, designed specifically for digital signal processing applications, have entered the market. The capabilities of such a processor indicates a high probability of success. In place of a full microprocessor development system, an evaluation board provides limited development capability. In addition, an evaluation board can be used in the recognition subsystem, greatly reducing circuit

design and development time. This approach provides an economical solution, with a proven design which is factory assembled and tested.

The TMS32010, a single-chip, 16/32 bit microprocessor manufactured by Texas Instruments, provides such a solution. This processor includes special instructions for signal processing applications and is capable of executing five million instructions per second. A modified Harvard architecture is employed. This architecture uses separate program and data memory, but unlike a true Harvard architecture, allows transfers between data and program spaces. Separating the program and data memory speeds execution by allowing an overlap in instruction fetch and execution. The data memory consists of 144 16-bit RAM locations on chip, and program memory consists of up to 4K of external memory. Additionally, the chip offers a 16-bit hardware multiplier, allowing multiplication in one cycle, and auto-increment/decrement of registers for indirect addressing of sequential data memory locations.

Fig. 2.7-21 shows the major components of the recognition subsystem. The Texas Instruments TMS32010 Digital Signal Processor Evaluation Module (EVM) provides support for the TMS32010 processor. This support includes a full 4K program memory RAM, an on-board assembler, monitor program, terminal and host computer interfaces, target board inteface, and an EPROM programmer. The target board interface provides a connector which is pin-for-pin compatible with the TMS32010 chip. These features greatly facilitate program generation and debugging.

The Texas Instruments Analog Interface Board (AIB) serves as the target board for the EVM and provides an on-board 12-bit Analog-to-Digital Converter (ADC), 12-bit Digital-to-Analog Converter (DAC), extended memory interfaces, and 16-bit external ADC and DAC interfaces. The on-board ADC operates at a 40 kHz rate maximum necessitating the use of an external ADC. An ANalog Device HAS-1204 12-bit ADC was connected to the external ADC interface on the AIB as shown in Fig. 2.7-22. This
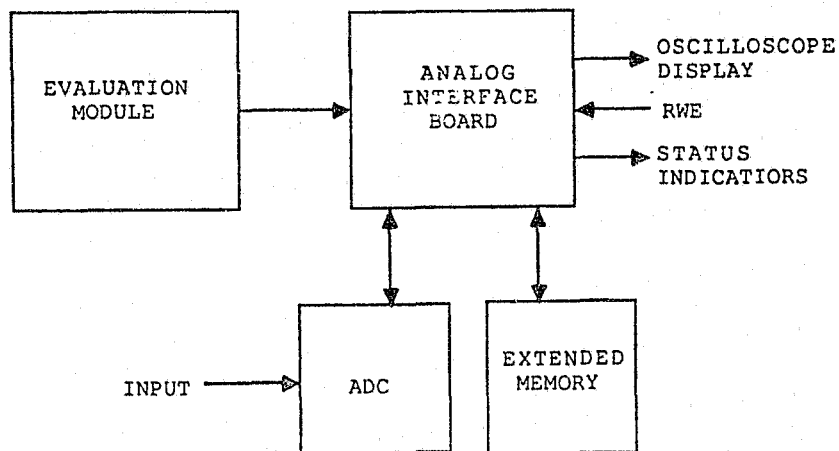
Fig. 2.7-21 Recognition Subsystem Block Diagram.
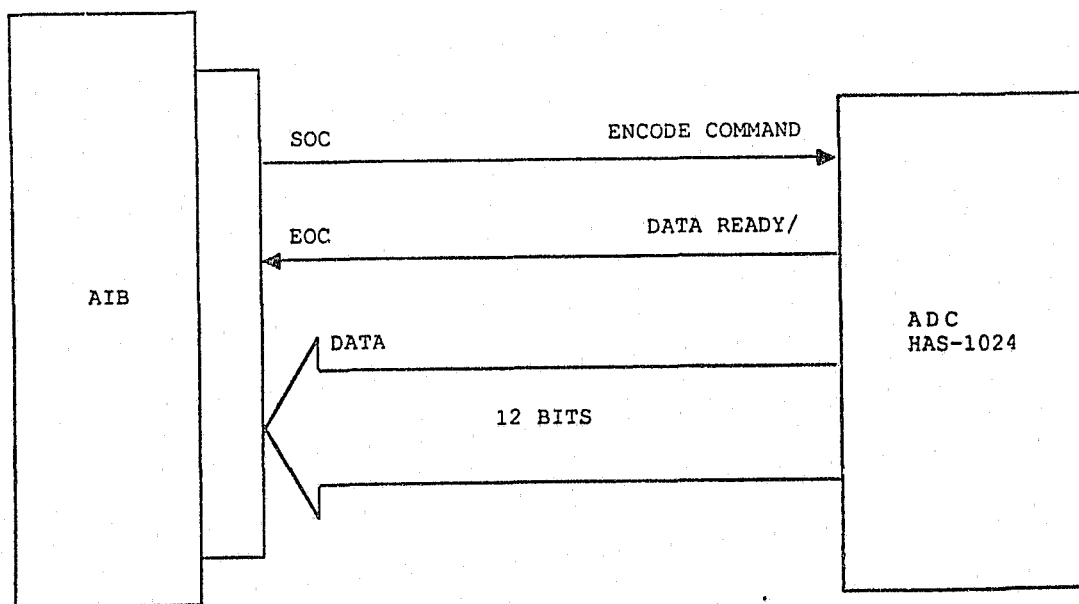
Fig. 2.7-22 AIB to ADC Interface.

90

ADC is capable of operating at sampling rates up to 500 kHz. The device is operated in the bipolar mode providing an input range of ±5V. As the power dissipation is specified at 2.3 watts maximum, a fan is included to provide cooling.

Although the ADC is designed to provide 12-bit resolution, the unit, as connected in this system, provides only 10 bits of resolution. This loss is attributed to noise in the system and, possibly, to the layout of the circuit board on which the ADC is mounted (a potential problem which Analog Devices points out in the data sheet). An IN instruction from Port 3 is used to read the external ADC.

Logic provided on the AIB greatly simplifies the interface to the ADC. The SOC signal from the AIB is tied to the Encode Command pin on the ADC. This signal is used to start the conversion process, and the EOC/signal is tied to the Data Ready/ pin on the ADC which latches the data into the input buffer. The falling edge of EOC/ also causes IORDY to be asserted which may be connected to BIO/ or INT/, as desired, by jumper E5 on the AIB.

Several data acquisition modes are available; two are discussed here. The automatic receive mode utilizes a sample rate clock on the AIB to generate the SOC. In the asynchronous receive mode the SOC is generated by reading the ADC port. The automatic receive mode simplifies the software loop timing and requires that IORDY be jumpered to BIO/ or INT/. BIO/ can then be polled to detect EOC. For the programs which operate with the subsystem, RWE, the signal to start sampling, is tied to BIO/ precluding the use of the automatic receive mode. Therefore, the asynchronous mode must be used. In this mode the software data acquisition loop length controls the sample rate and must allow sufficient time for the conversion process. For operation on the bench, the program BTEST1 (see the Reference) allows continuous operation by beginning the sampling process immediately after the computations are completed.

Since the TMS32010 has only 144 bytes of data memory, the extended memory interface provided is used. Additional memory is required for sufficient storage of the

sampled data and the coefficients used in the DFT computation. This memory is accessed as an I/O port with IN and OUT instructions. Address registers with an address counter and the necessary control logic is provided on the AIB to enable access to sequential locations with the address counter either incremented or decremented after each input or output operation as desired. This method provides faster access to sequential locations than use of the TBLW and TBLR instructions which transfer data to and from program memory. The IN and OUT instructions require 2 machine cycles while the TBLW and TBLR use 3 cycles. Two sockets are available for two HM6264-12 RAM chips allowing 8k words of extended memory. An expansion connector, with decoding in 8k blocks, is used to interface up to 64k of total memory. Two 2764 EPROMs were programmed with the Fourier coefficients and wired to this connector. Fig. 2.7-23 shows details of this connection. The extended memory address is read from, and written to, through Port 4 and the extended memory data is accessed through Port 5. The status indicator shown in Fig. 2.7-24 consists of 4 LED's that indicate which frequencies are being detected. In addition, an output to an audible beeper is included. This interface is provided through Port 3, intended primarily for an external DAC, having 16 output lines available. An oscilloscope output is generated by the onboard DAC to provide an analog indication of the computation results. A summary of the Port addresses used is given in Table 2.7-2 and Fig. 2.7-25 is a diagram of the subsystem enclosure's front and rear panels. Appendix A of the reference contains a list of the external connections to the recognition subsystem.

Software

The programs executed by the EVM were developed using a Texas Instruments Business-Pro computer with a TMS 32010 assembler. The programs, written in TMS 32010 assembly code to provide the fastest possible execution, are easily edited, assembled and stored on the Business-Pro and downloaded to the EVM through the host computer interface.
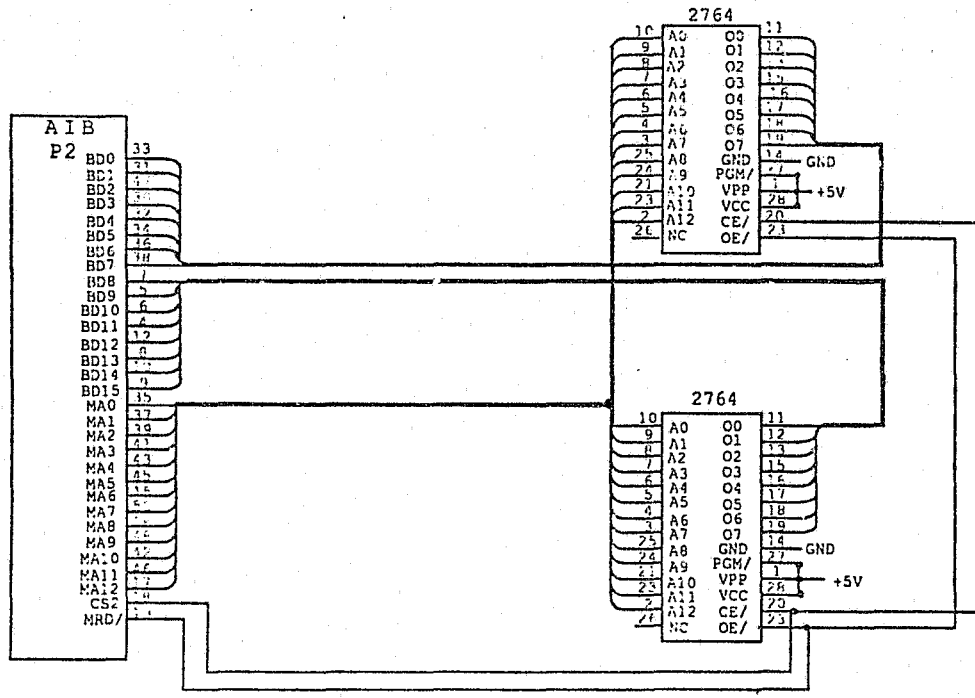
Fig. 2.7-23 AIB-to-Extended Memory Interface Schematic.
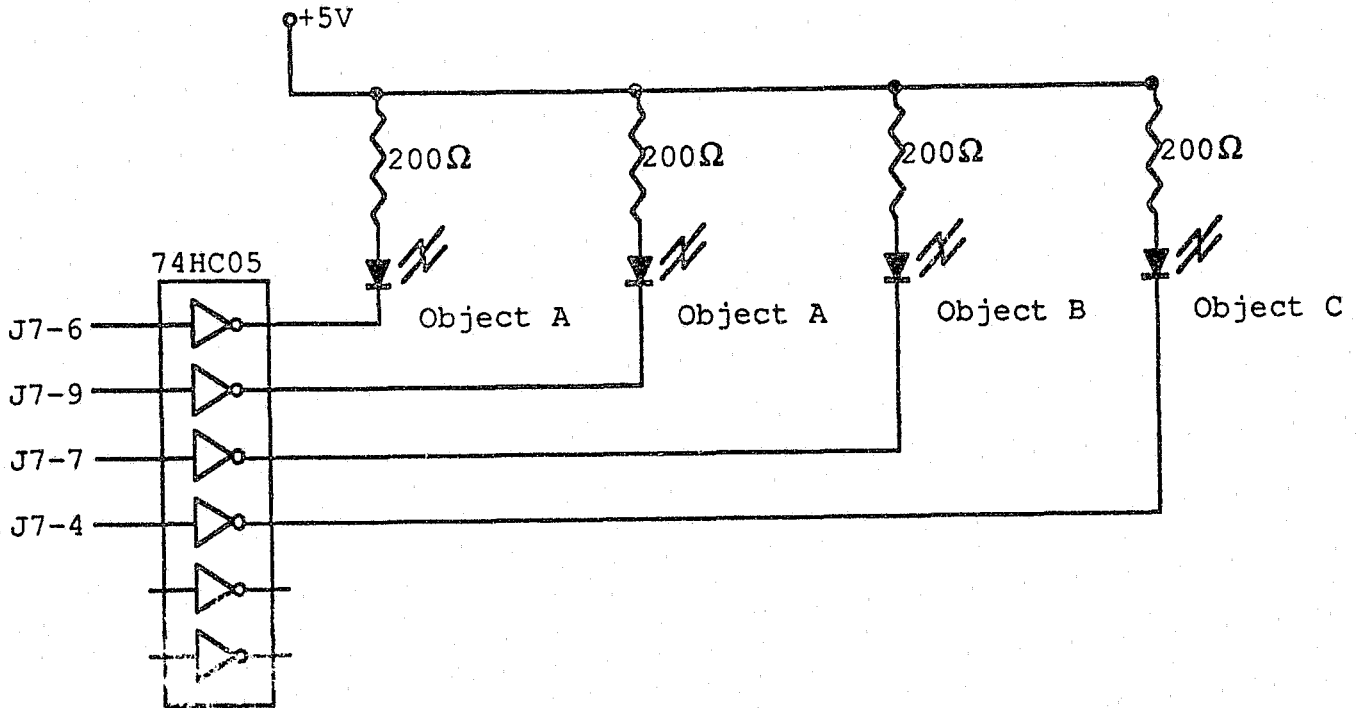
Fig. 2.7-24 Status Indicator Schematic.

93

Table 2.7-2 Port Address Summary.

PORT INPUT ADDRESS	INPUT FUNCTION	OUTPUT FUNCTION
0	Read A/D Status Register	Load AIB Control Register
2		Write D/A Converter Data
3	External ADC	Parallel Output (Status Indicatior)
4	Read Extended Memory Address	Load Extended Memory Address
5	Read Extended Memory	Load Extended Memory

EVM
RESET

AIB
RESET

POWER
INDICATOR

J3 DAC
OUT

J4 ADC
IN

J5
EXPANSION
ADC IN

FRONT PANEL

J7
PARALLEL
I/O

J8
HOST
COMPUTER
INTERFACE

J6
TERMINAL
INTERFACE

REAR PANEL

J2
POWER

J1
POWER
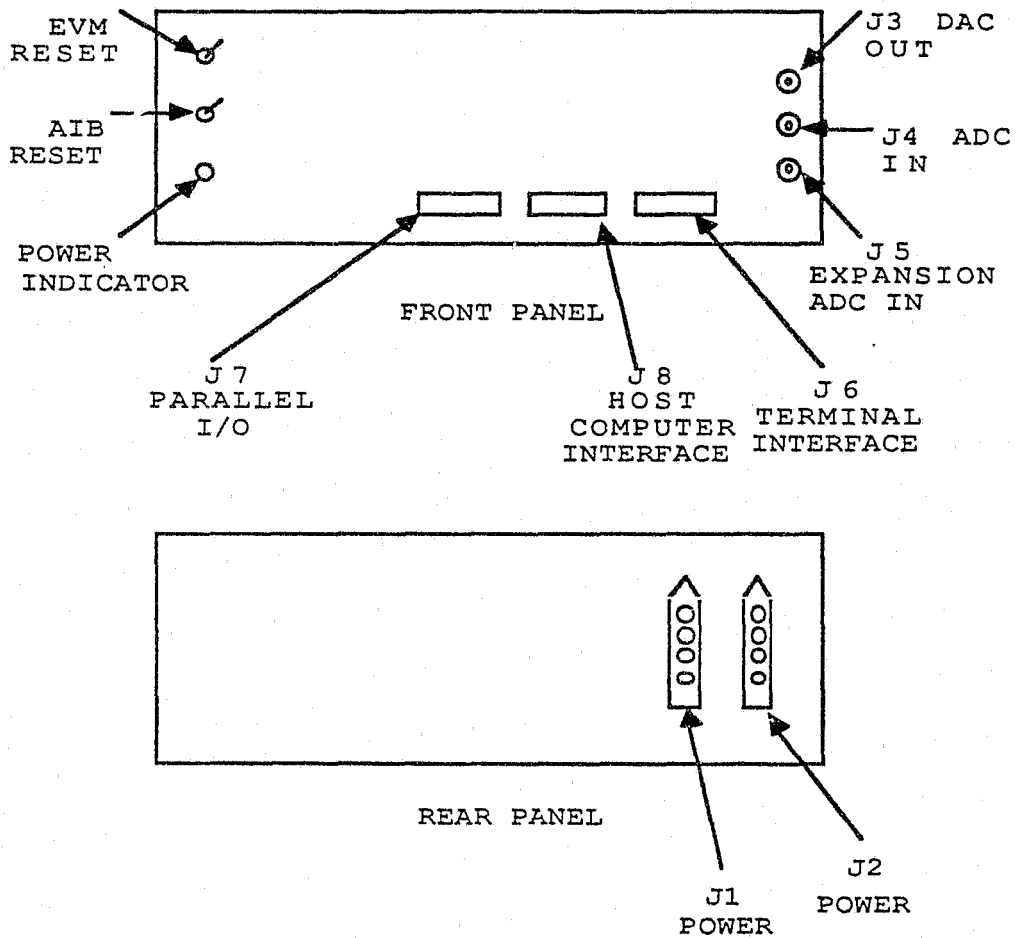
Fig. 2.7-25 Subsystem Enclosure Front and Rear Panels.

Four of the programs developed for the subsystem may be found in the Appendices of the Reference. BTEST1 is intended for operation on the bench without the RWE signal from the system controller. Many of the test results given in Chapter IV of the Reference were taken using BTEST1. The remaining programs are for use in the system and differ only in the classification routine. FAST1 is the basic program using the simplest classification algorithm. DFAST1 employs a self setting dynamic threshold which adjusts to the ambient noise level. KEYS uses the most sophisticated classification routine and is designed to ignore noise caused by rattling keys and change.

The operation of all the programs is straightforward as seen in the Program Flow Chart presented in Fig. 2.7-26. As shown in Fig. 2.7-26, the programs wait for RWE to indicate that the input signal is ready to be sampled. At that point the program takes 1024 samples at a rate of 200,000 samples per second. BTEST1 differs from the rest of the programs by ignoring RWE sampling as soon as the previous computations have been completed.

Once the data is obtained the first frequency component is computed and the results both stored and sent to the onboard DAC providing a real time oscilloscope display. This process is then repeated for the second, third, and fourth frequency components. Note that although only one resonant frequency in the target is stimulated for each measurement, the algorithm computes all four frequencies for each measurement. This allows for a simpler interface between the subsystem and controller. The subsystem does not need to know which frequency is being excited. The actual computation of each component of the spectrum is obtained from the general form of the DFT given as:

$$F(u) = 1/N \sum_{t=0}^{N-1} f(t) [cos(2\pi ut/N) - j \ sin(2\pi ut/N)] \tag{3}$$
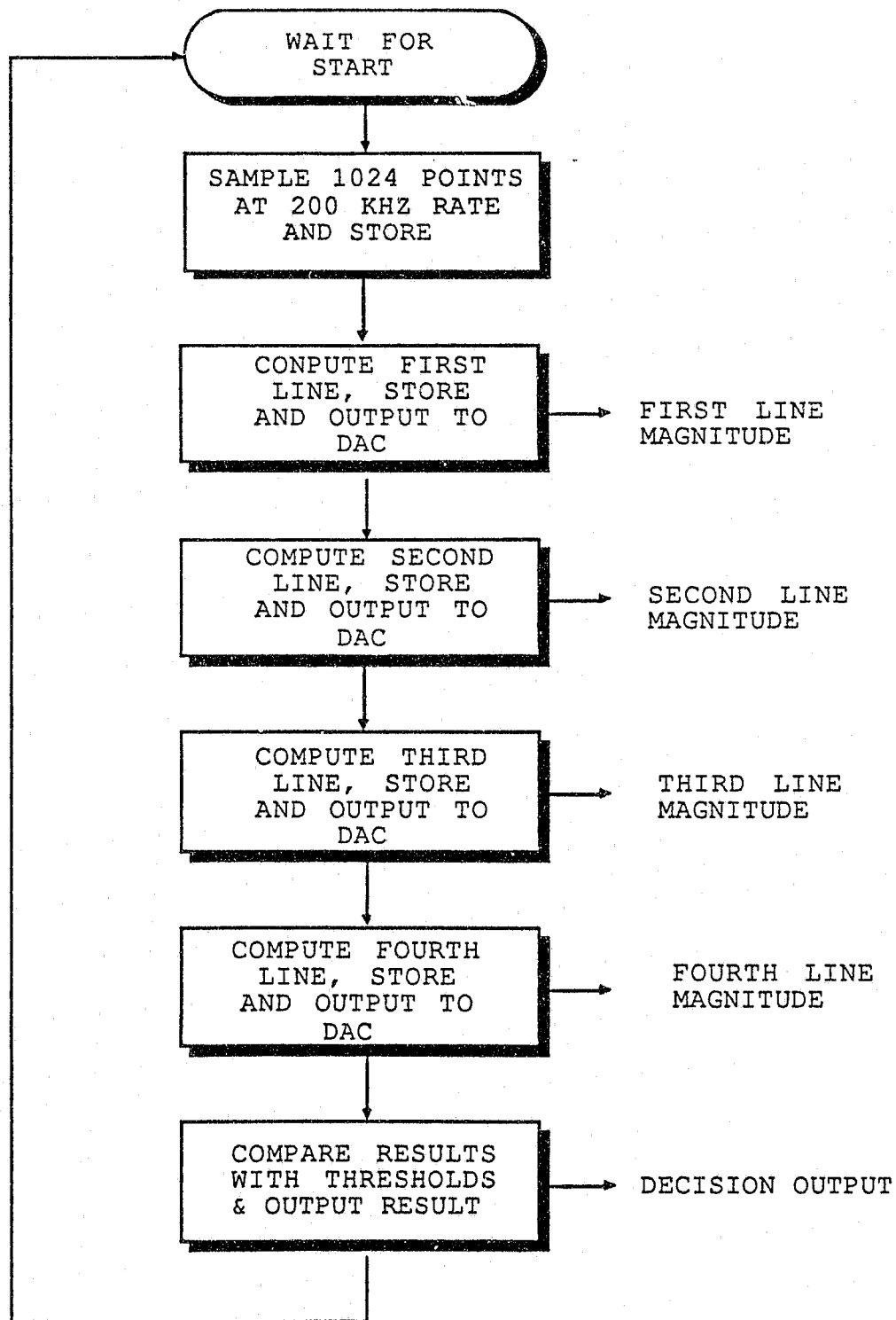
Fig. 2.7-26 Program Flow Chart.

where N is the number of samples, f(t) is the input signal, and u is the frequency of interest. This can be broken into a real part and an imaginary part. The cosine and sine terms are computed in advance for each of the four frequencies and stored in the EPROMs located in the extended memory of the AIB. The program computes the real and imaginary parts separately, squares each part and sums them to produce the square of the magnitude. This magnitude squared result is then used by the program to make the decision.

The computation of the Fourier coefficients is accomplished as shown below. Recall that the resolution of the DFT is expressed as Resolution = Sample Rate/N. The spectrum produced covers 0 Hz to the sample rate, in this case 200 kHz, and is divided into N lines. One should note that the information above one-half the sampling rate is a reflection of the information below one-half the sampling rate, for real signals. To find the line number closest to the desired resonant frequency, the following can be used:

$$\text{Line Number} = \text{INT} \left[(\text{Frequency} / \Delta u) + 0.5 \right] \tag{4}$$

This Line Number then represents u in the DFT expression given in Equation 2.7.3. The value of the coefficients are scaled to the maximum range allowed with a 16-bit representation and stored sequentially in EPROM from t=0 to t=N-1 using:

$$C_R(t) = (2^{15} - 1) \cos (2\pi u t/N) \tag{5}$$

for the real coefficients and:

$$C_I(t) = (2^{15} - 1) \sin (2\pi u t/N) \tag{6}$$

for the imaginary coefficients. For the computation used, the real coefficients are interleaved with the imaginary. There are 2N coefficients required for each line, and in this case 8k of EPROM is required for the 4 lines computed.

Finally, after all the computations have been completed, a decision is made based on these results.

Four different classifiers are presented in the programs listed in the Appendix of the Reference. Fig. 2.7-27 shows a flow chart of the classification used in BTEST1. BTEST1 computes a running average of the 8 most recent responses for each of the frequencies. If any of the preset thresholds are exceeded by the average, the audible signal and appropriate frequency indicators are turned-on. FAST1 employs the same classification except that the results of the present computation is used rather than a running average. A flow chart for the classification used in FAST1 is given in Fig. 2.7-28. For proper operation of a program which uses the classifier in BTEST1, a modified control routine must be used. As BTEST1 uses the 8 most recent measurements, each frequency must be stimulated 8 times in succession for the average to be meaningful. DFAST1 is an attempt to make the threshold self adjusting with the ambient noise level. DFAST1, as shown in Fig. 2.7-29, averages the most recent computations which results in a measurement that is representative of the background noise level. A margin is added to the average to produce the threshold and the classification is performed as in FAST1. KEYS uses a fixed set of thresholds but requires that exactly one frequency component exceeds the threshold for any measurement. Additionally, KEYS requires that a given frequency be detected twice before the audible signal is activated. Fig. 2.7-30 shows the operation of KEYS.

All programs given in the Appendices of the Reference are similar. For a thorough understanding the reader should be familiar with the TMS32010 Assembly Lanugage as specified in the TMS32010 Assembly Language Programmer's Guide (Texas Instruments, 1983). A discussion of the code is presented in Appendix B of the Reference to augment the comments given in the source code.

```
          ┌─────────────────────┐
          │      AVERAGE        │
          │  8 MOST RECENT     │
          │  MEASUREMENTS      │
          └─────────────────────┘
                    │
                    ▼
          ┌─────────────────────┐
          │     COMPARE        │
          │     AVERAGE        │
          │      WITH          │
          │   THRESHOLDS       │
          └─────────────────────┘
                    │
                    ▼
               ╱────────╲
              ╱   ARE    ╲
             ╱    ANY     ╲
            ╱  THRESHOLDS  ╲────────▶ RETURN
            ╲  EXCEEDED    ╱
             ╲     ?      ╱
              ╲──────────╱
                    │
                   YES
                    │
                    ▼
          ┌─────────────────────┐
          │     OUTPUT:         │
          │   FREQUENCIES       │
          │   PRESENT  &        │
          │  AUDIBLE SIGNAL     │
          └─────────────────────┘
                    │
                    ▼
               RETURN
```
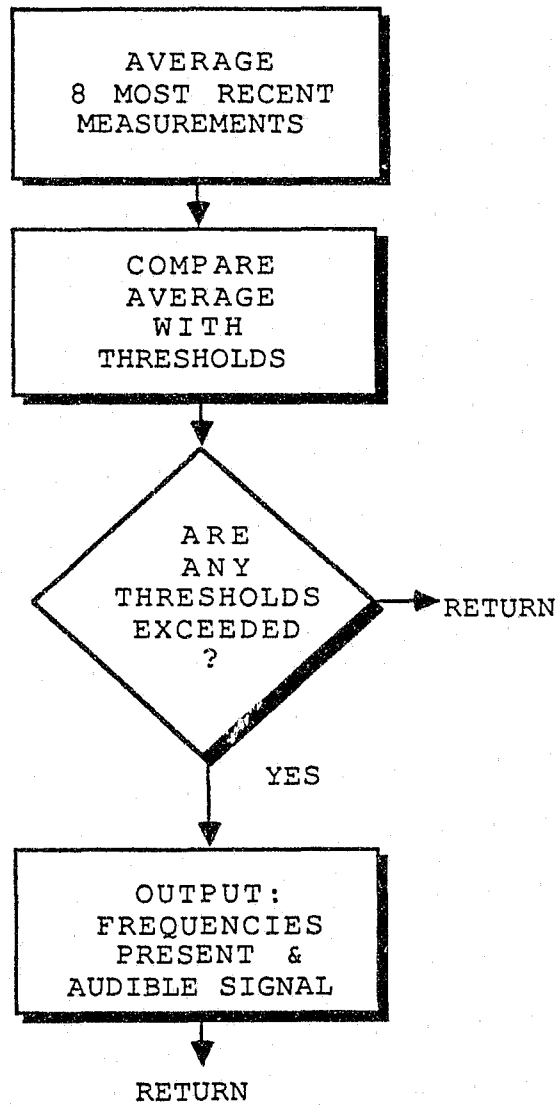
Fig. 2.7-27 BTEST1 Classification Flow Chart.
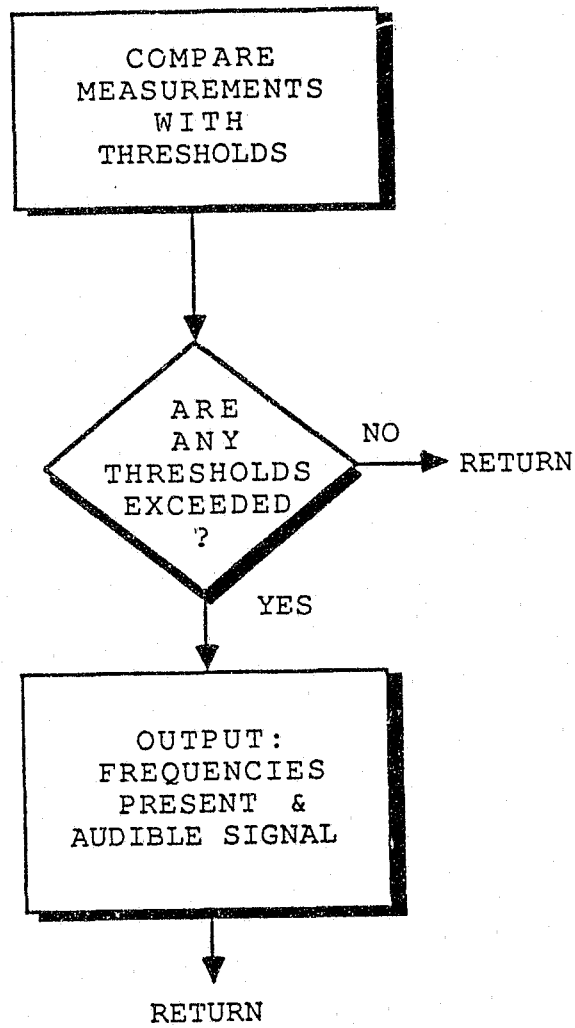
Fig. 2.7-28 FAST1 Classification Flow Chart.
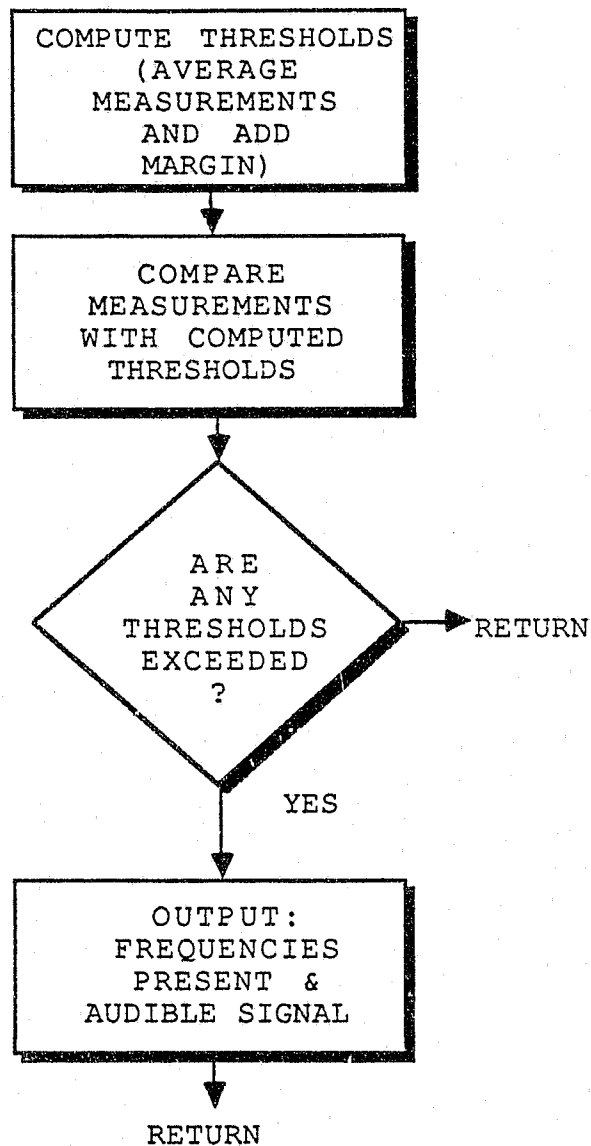
Fig. 2.7-29 DFAST1 Classification Flow Chart.
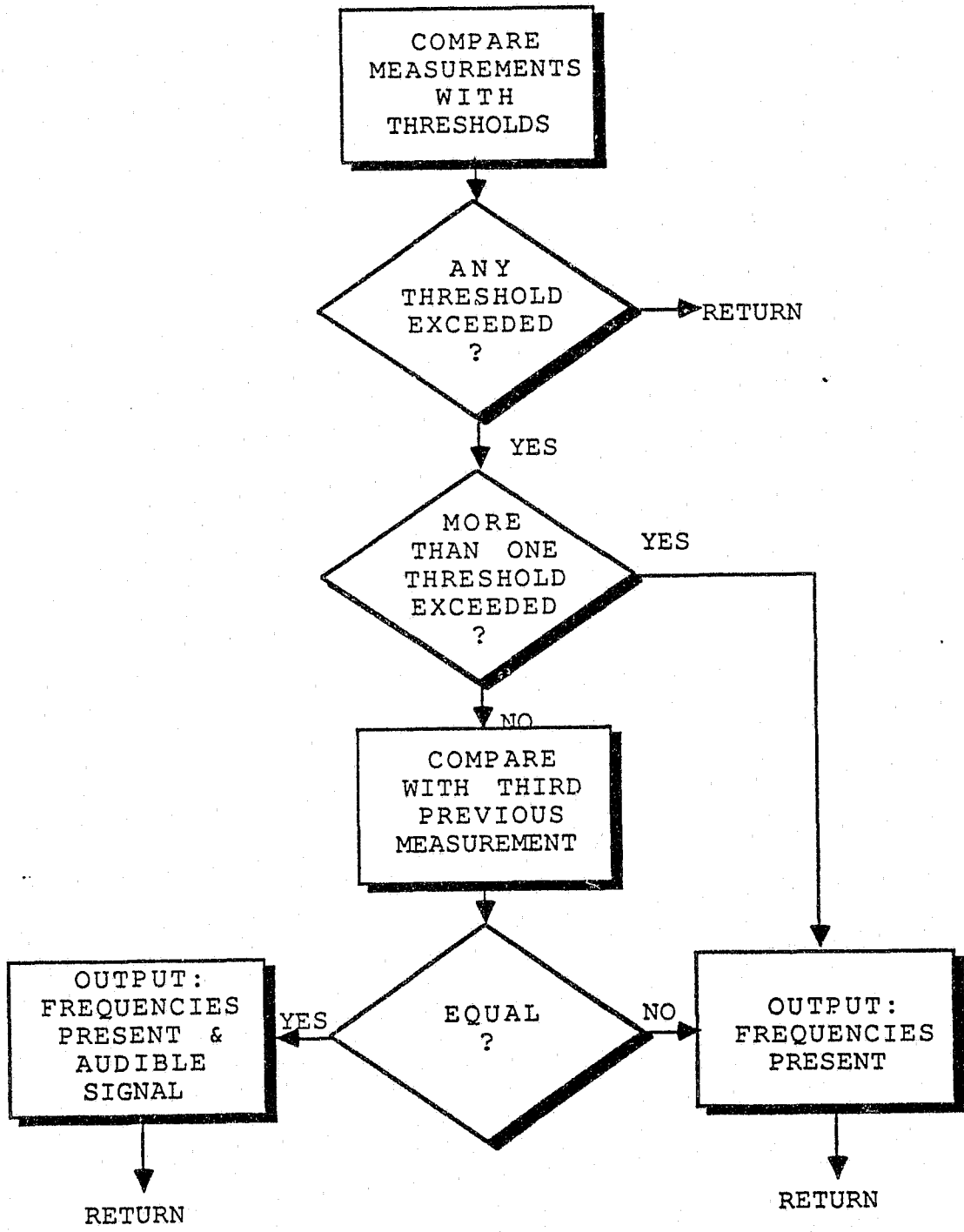
Fig. 2.7-30 KEYS Classification Flow Chart.

Operation

Operation of the digital subsystem is automatic. This is accomplished through modification of the EVM power-up routine to allow automatic loading and execution of a program. An EPROM programming utility is included in the EVM operating system. This utility allows the user to load a program into Program Memory, test it, and program an EPROM with the contents of Program Memory. The modified EVM power up routine loads program memory from the EPROM programming socket and begins execution automatically. The details of this modification and the programming of EPROMs is given in the *TMS320210 Evaluation Module User's Guide* (Texas Instruments, 1983). Following modification, the unit will begin execution, after a short delay, with no operator action required.

Further details are available in the *TMS32010 User's Guide* (Texas Instruments, 1983). Details on the AIB are available in the TMS32010 *Analog Interface Board User's Guide* (Texas Instruments, 1983).

2.8 Analog Fourier Filter (Rochelle)

According to Parseval's Theorem, the magnitude squared of the Fourier transform of any time signal is the energy density function (in J/Hz) of the signal in frequency space. For less than infinite integration time, the magnitude squared of the finite time (windowed) Fourier transform is an estimate of the energy density function, and therefore has long been used to estimate the energy density at a particular frequency or across a spectrum of frequencies for the case of the classical periodogram computed using the FFT on a digitized version of the signal.
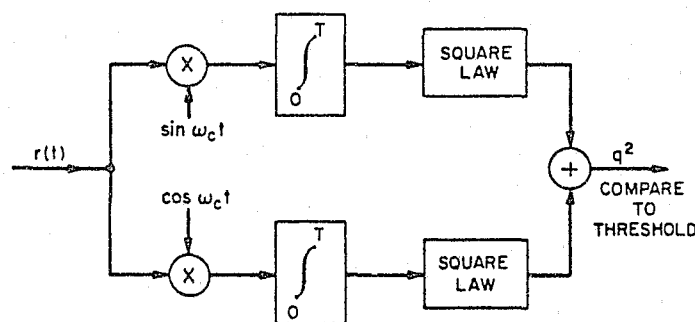
Fig. 2.8-1 Analog Fourier filter block diagram.

If one is interested only in the energy density estimate at a particular point in frequency space, then the magnitude squared computation illustrated in Fig. 2.8-1 can be properly interpreted as functioning like a filter (we have named it "Fourier filter") producing a certain output response dependent on the energy spectral density of the input data signal. Similarly a periodogram computed digitally can be interpreted as a bank of Fourier filters equally spaced in the frequency domain, and normally covering a range from 0 Hz out to the folding frequency. The -3 db bandwidth (frequency resolution) and equivalent random noise bandwidth vary inversely with T, the integration time, for computing the energy density estimate.

In addition to the usual advantages of digital versus analog computing (programmability, stability, accuracy, etc.) the digital periodogram computed via the

FFT has the great advantage of computing the entire spectrum as defined above about as quickly as it can compute any one point in the spectrum. Typically, the analog Fourier filter computes only one point in the spectrum for any one data interval. Also the analog computation requires a precision reference frequency whereas the FFT input comes from programmed constants. Paradoxially, however, the digital computation turns out to be rather inflexible when one wants to improve frequency resolution by increasing T because either the computation must be reformatted to increase the number of points in the spectrum or a complicated heterodyning process with a new antialias filter must be invoked to obtain the so-called zoomed spectrum.

On the other hand, with the analog computation, a longer integration time to improve frequency resolution and lower the noise bandwidth merely requires holding the analog integrator's gate open longer for it to process more data. Of course, the analog version also has the advantage of operating in real time and not requiring an expensive digitizer.

The analog Fourier filter was implemented with internally trimmed integrated circuit transconductance multipliers, integrated circuit operational amplifiers, and CMOS-controlled analog switches. The reference frequency was supplied from the UFS synthesizer, and the quadrature phase shifter was also implemented with integrated circuit operational amplifiers.

2.9   Transmitter Pulse Shape Optimization (Rochelle/Castillo)

Background:

The goal of this research has been to ascertain the optimum transmitter pulse shape characteristics to be used for acoustical excitation of ultrasonic mechanical vibration modes in rigid structures such as handguns. Other than frequency, the primary parameter to be optimized was the transmission pulse duration (width) which if chosen too short results in insufficient energy deposition in the vibrational mode, and if chosen too long results in wasteful time usage and unnecessary data rate limitation. The motivation for this study is traceable to the following two factors.

1.   An explanation and understanding was needed for our observations during Phase II/1 that certain widths were far more effective than others when using off-resonance excitation with rectangular windowing.

2.   Later we discovered that lower sidelobe windows such as triangular and Hanning were desirable for audible noise reduction, and so we needed a theoretical basis for selecting the optimum width of these windows as well; both for center frequency and off-resonance excitation.

Model and Analysis Methods:

Specifically we have used a series RLC electrical network to model the 36.44 kHz barrel mode of an M-10 handgun (45 cal.) which was determined from anechoic chamber measurements to have a Q of about 4900. Circuit parameters chosen for the model were R=0.7428 ohms, L=0.0159 H, and C=1.199738 nF. Energy coupling was through a direct series-connected voltage source with no attempt to set any quantitative equivalence between electrical quantities and corresponding mechanical quantities because our main intent was to study the effect of excitation pulse width on the relative energy and signal levels of the excited vibration after termination of the excitation pulse.

The transient response of our model for on and off resonance excitation using rectangular, Hanning, or triangular window modulation has been solved exactly using classical circuit analysis techniques. Also the same responses have been acquired using the SPICE computer aided circuit analysis program.

Rectangular Window Analytical Results:

Results of the exact analysis for on-resonance (Fin=Fr) and two off-resonance cases are shown in Fig. 2.9-1 in which the relative response (voltage across the resistor) is shown plotted versus the rectangular window width. The response was computed at a time corresponding to the end of the window width. Computations using SPICE produced similar results.

Note particularly the cyclical nature of the off-resonance cases showing for example that a width of 48 msec (1749 vibration cycles) produces less than half the signal strength of the shorter 22 msec width for the case of a 20 Hz difference frequency. The spacing between peaks and valleys is inversely proportional to the difference frequency, and the first peak to first valley ratio grows toward infinity as the difference frequency is increased.

Hanning Window Analytical Results:

The Hanning window is simply a raised cosine window which produces a modulated transmitter pulse as illustrated in Fig. 2.9-2 (shown for 2 msec width). The exact analytical model response results using this signal for the excitation function are shown in Fig. 2.9-3 for same frequency cases as the rectangular window shown above. Again these curves represent the vibration signal strength computed at the end of the incident excitation pulse, i.e., at the beginning of the decay interval. Computations with SPICE produced similar results.

Note that an optimum width exists for all three cases including F = Fr.
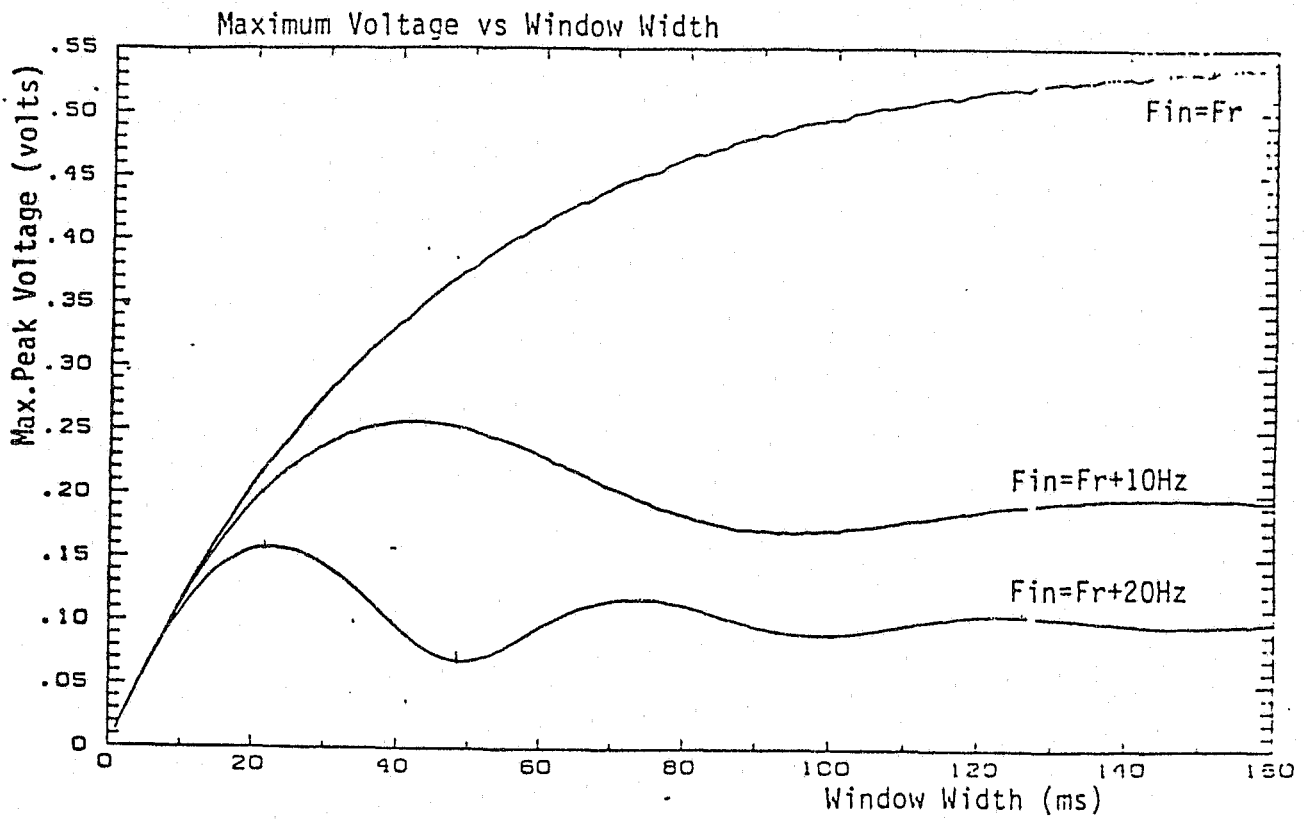
Fig. 2.9-1 Theoretical results for rectangular window Fr = 36.44 kHz and Q = 4900.
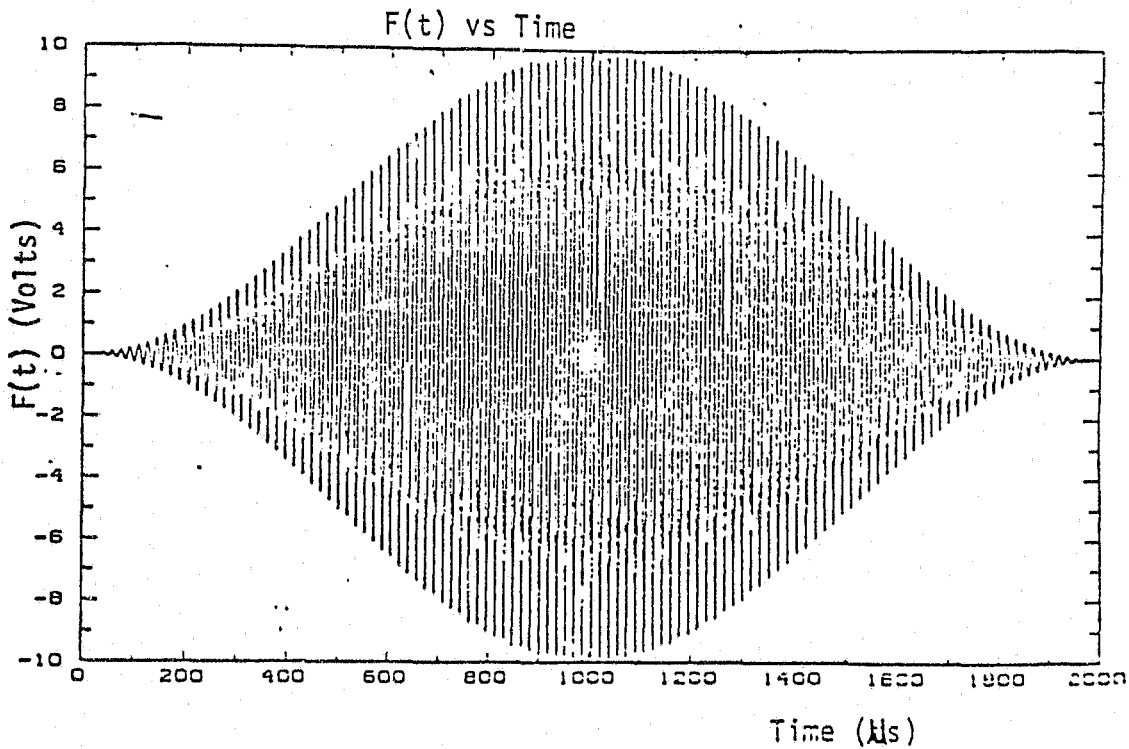
Fig. 2.9-2 Ultrasonic signal with Hanning window modulation.

109
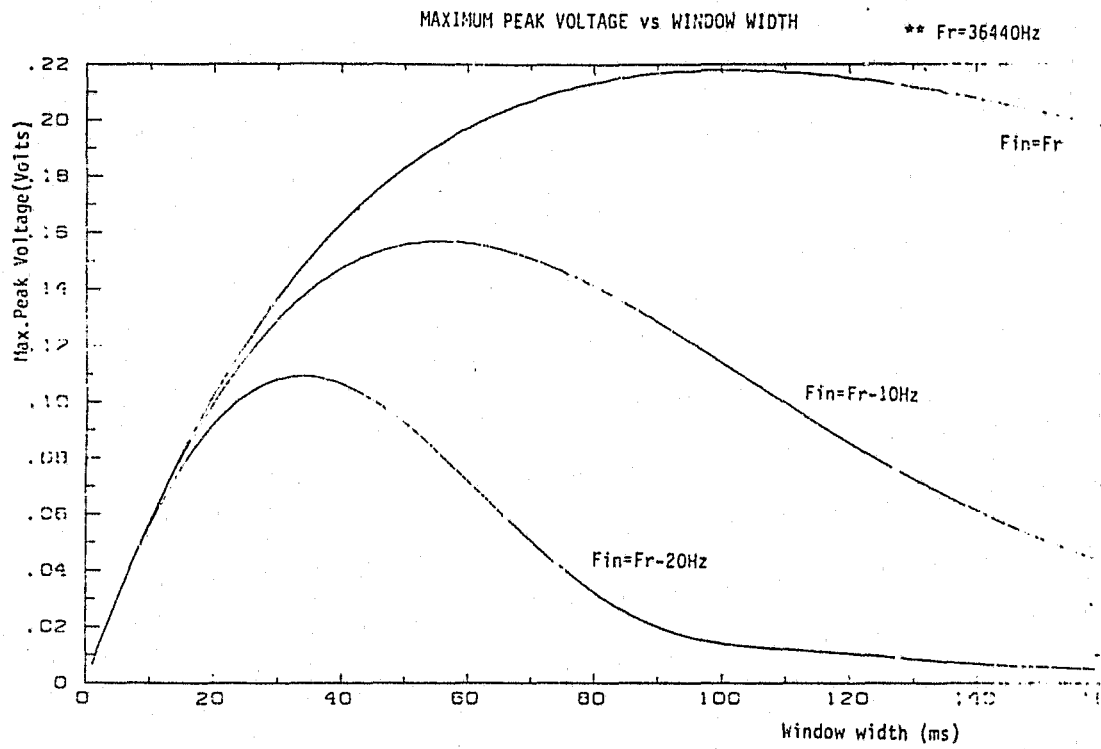
Fig. 2.9-3 Theoretical results for Hanning window with Fr=36.44 kHz and Q = 4900.

Triangular Window Analytical Results:

Analytical results for the triangular (linear ramp up and linear ramp down) are given in FIg. 2.9-4 for the same frequencies as the other two window examples. Note that the results are very similar to the Hanning window, and that an optimum width does exist for all cases including center frequency excitation.

MAXIMUM PEAK VOLTAGE VS WINDOW WIDTH
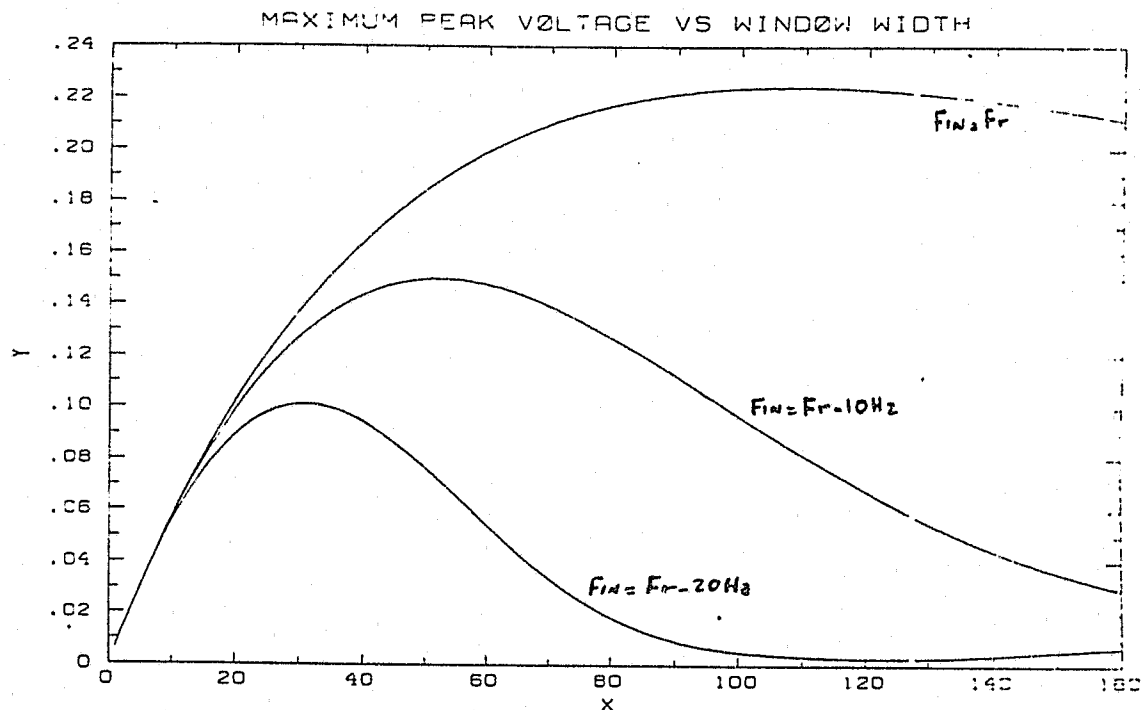
Fig. 2.9-4 Theoretical results for triangular with Fr = 36.44 kHz and Q = 4900.

Experimental Results:

Excellent agreement has been obtained between the model analysis summarized here and experimental measurements of the vibration response of an M-10 handgun.

Both the analysis and experimental portions of this research will be fully documented in Domingo Castillo's forthcoming M.S. thesis.

2.10 Experimental Vibration Studies (Rochelle)

Introduction:

The vibration spectra presented here were obtained with the targets and ultrasonic receiving system located in the anechoic chamber and using steel ball impacts as the method of excitation. The spectra were acquired with an HP3561A spectrum analyzer using the Hanning data window.

UZI Short Barrel and Long Barrel Comparison:

The 0-100 kHz spectrum is shown in Fig. 2.10-1 for the long barrel UZI and in Fig. 2.10-2 for the short barrel UZI. Zoomed 40 to 60 kHz spectrum is shown in Fig. 2.10-3 for the long barrel UZI and in Fig. 2.10-4 for the short barrel UZI.

M-10 Comparisons:

Full 0-100 kHz barrel spectra for three different M-10 handguns are presented in Figs. 2.10-5 through 2.10-7. The serial numbers and corresponding barrel outside diameters were #81-0003927 with 0.681 in o.d., #81-0003975 with 0.687 in o.d., and #81-0004920 with 0.680 in o.d.

Zoomed 30-40 kHz barrel spectra for these same handguns are presented in Figs. 2.10-8 through 2.10-10.

Full 0-100 kHz knob spectra are presented in Fig. 2.10-11 through 2.10-13, and zoomed 0-100 knob spectra are presented in Figs. 2.10-14 through 2.10-16.

Comparison of Dummy .22 Cal. Barrels:

Full 0-100 kHz spectra from three different dummy .22 cal barrels are presented in Figs. 2.10-17 through 2.10-19, and zoomed 85 to 95 kHz spectra are presented in Figs. 2.10-20 through 2.10-22. These barrels were nominally identical except for lengths which were 1 in, 2 in, and 3-3/8 in.

RANGE: 20 dBV   STATUS: PAUSED

A: MAG

0
dBV

10
dB
/DIV

-71
START: 0 Hz   BW: 375 Hz   STOP: 100 000 Hz
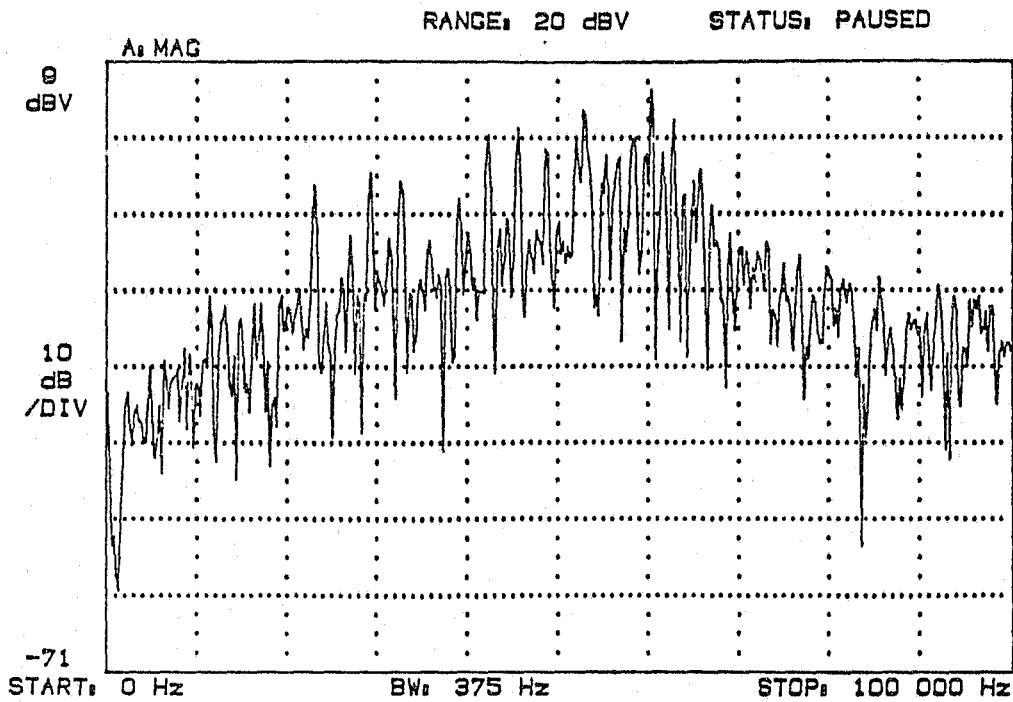
Fig. 2.10-1 Full 0-100 kHz spectrum for long-barrel UZI

RANGE: 20 dBV   STATUS: PAUSED

A: MAG

0
dBV

10
dB
/DIV

-71
START: 0 Hz   BW: 375 Hz   STOP: 100 000 Hz
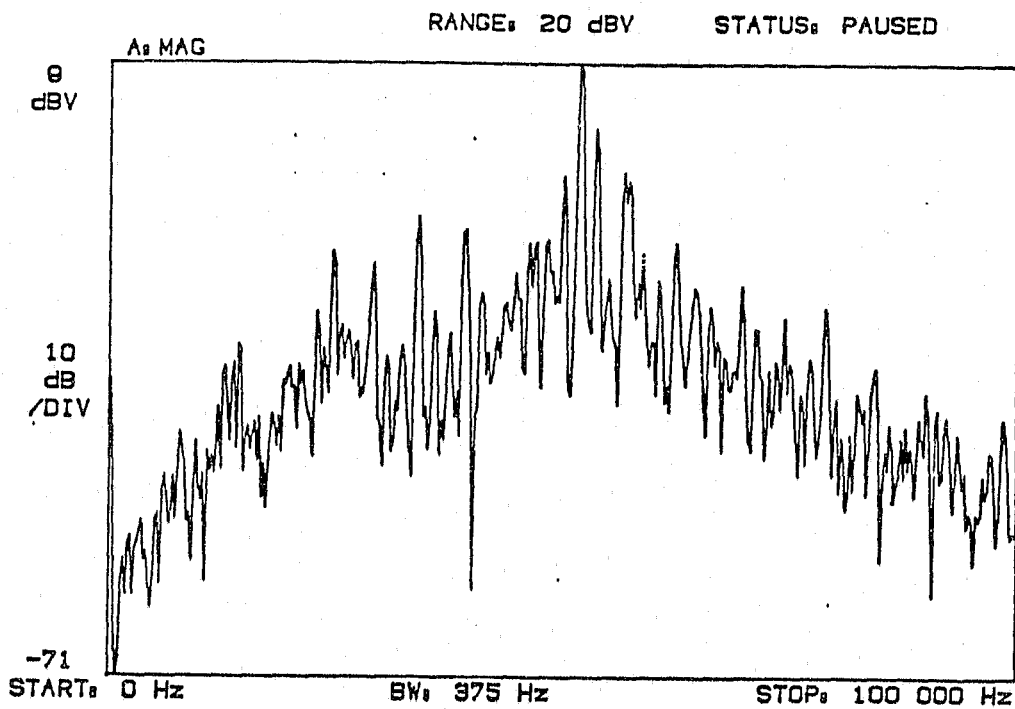
Fig. 2.10-2 Full 0-100 kHz spectrum for short-barrel UZI

113
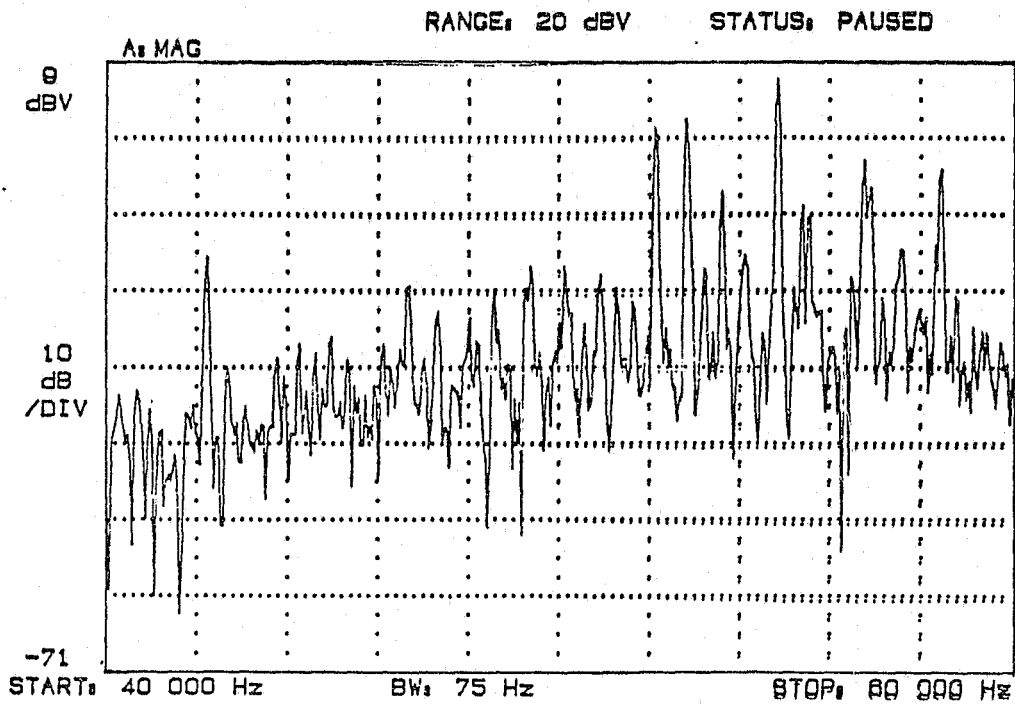
Fig. 2.10-3 Zoomed 40-60 kHz spectrum for long-barrel UZI
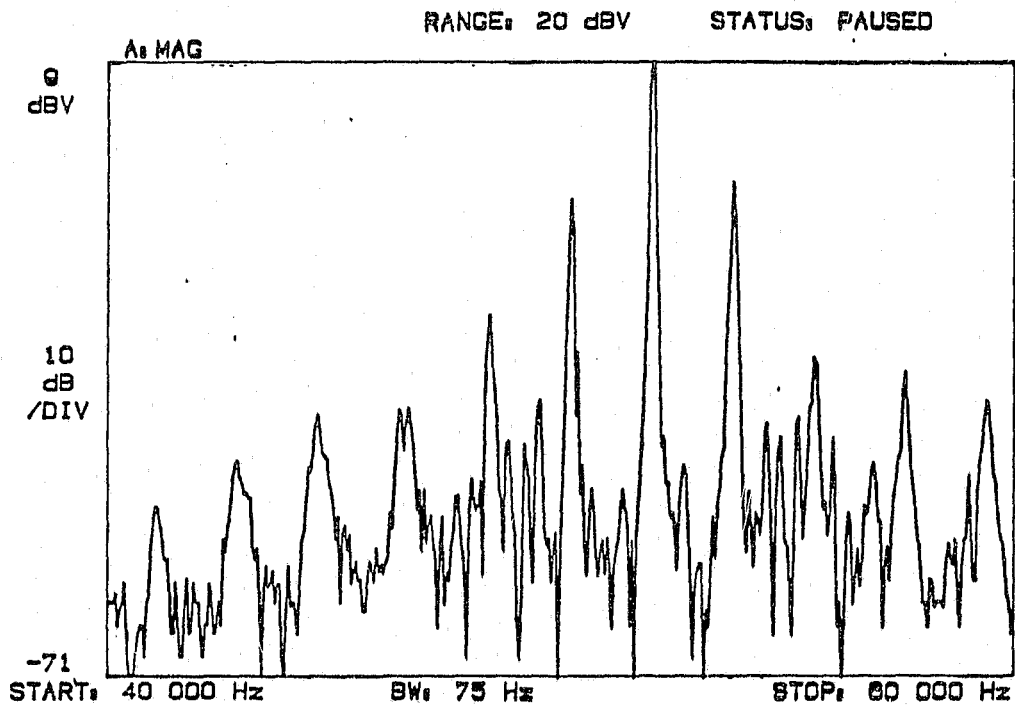
Fig. 2.10-4 Zoomed 40-60 kHz spectrum for short-barrel UZI

114

A: MAG

20
dBV

10
dB
/DIV

-80
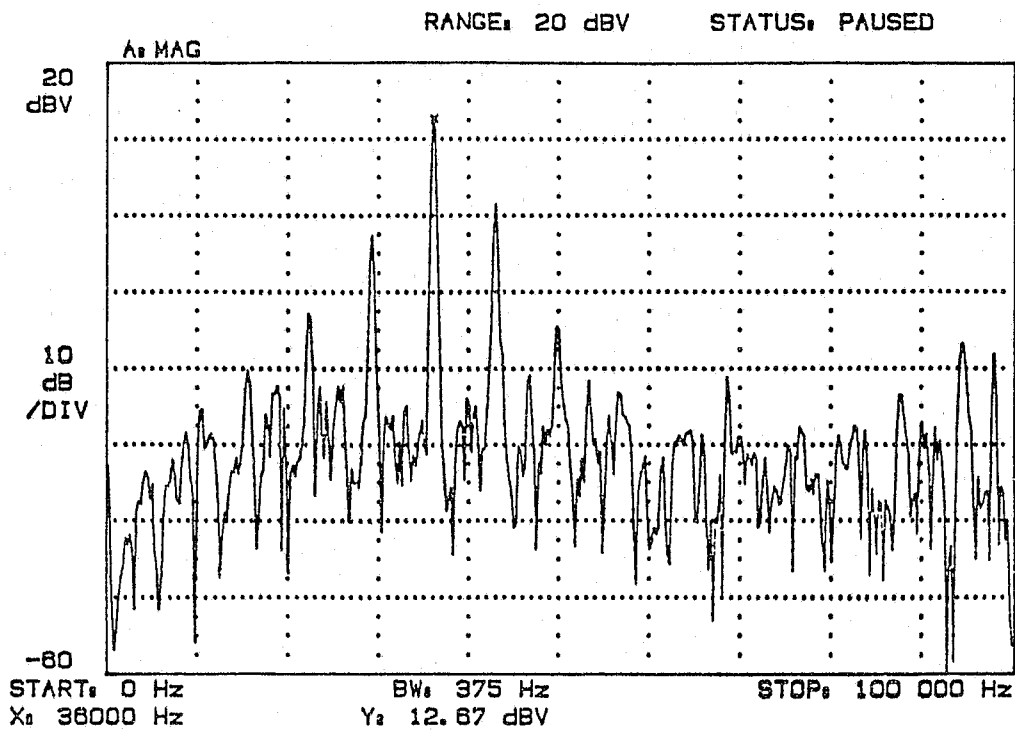
Fig. 2.10-5 Full kHz barrel spectrum for M-10 with .681 in barrel

A: MAG

20
dBV

10
dB
/DIV

-80
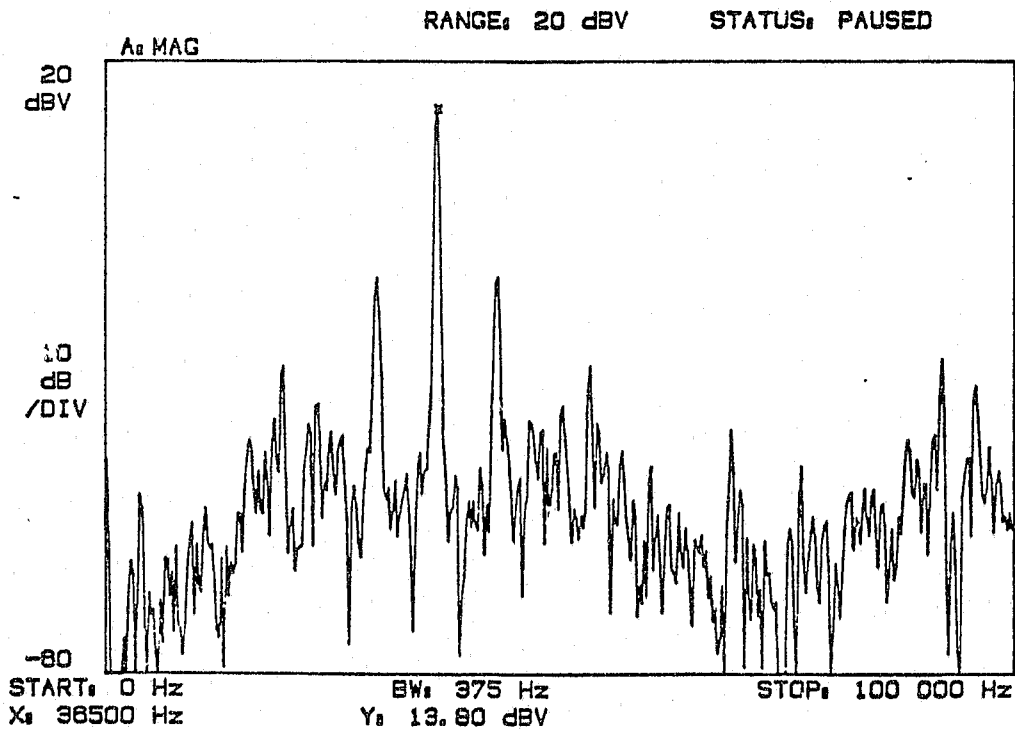
Fig. 2.10-6 Full 0-100 kHz barrel spectrum for M-10 with .687 in barrel

A: MAG

```
20
dBV




10
dB
/DIV




-80
```

START: 0 Hz   BW: 375 Hz   STOP: 100 000 Hz
X: 36000 Hz   Y: 12.68 dBV
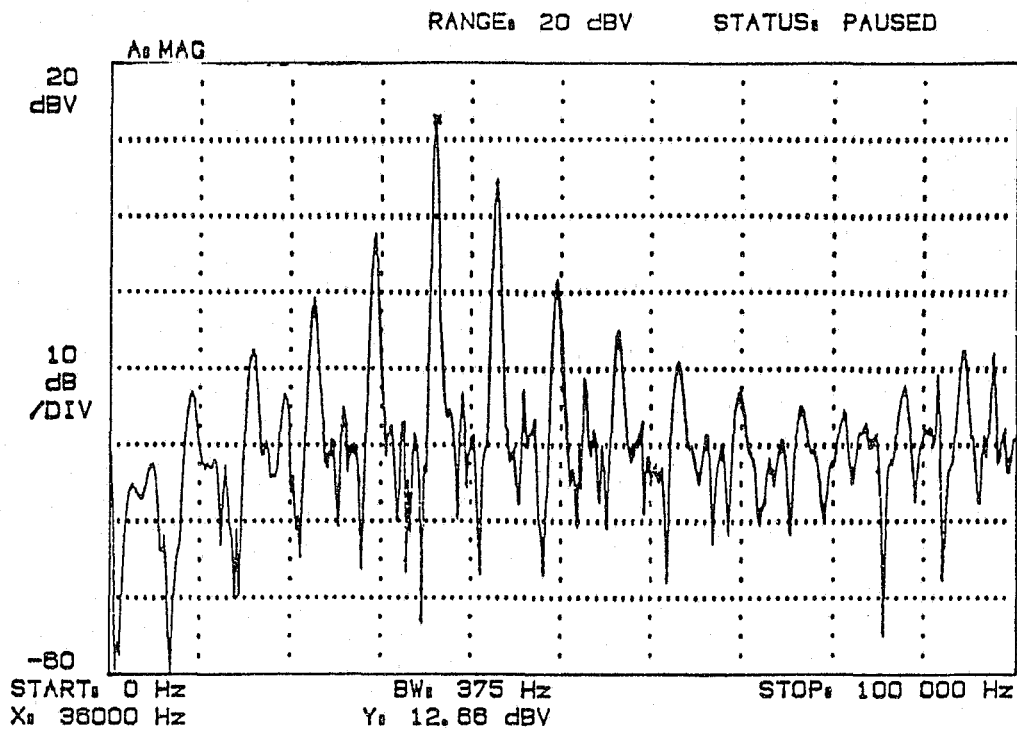
Fig. 2.10-7 Full 0-100 kHz barrel spectrum for M-10 with .680 in barrel

A: MAG

```
9
dBV




10
dB
/DIV




-71
```

START: 30 000 Hz   BW: 37.5 Hz   STOP: 40 000 Hz
X: 40000 Hz   Y: -58.85 dBV
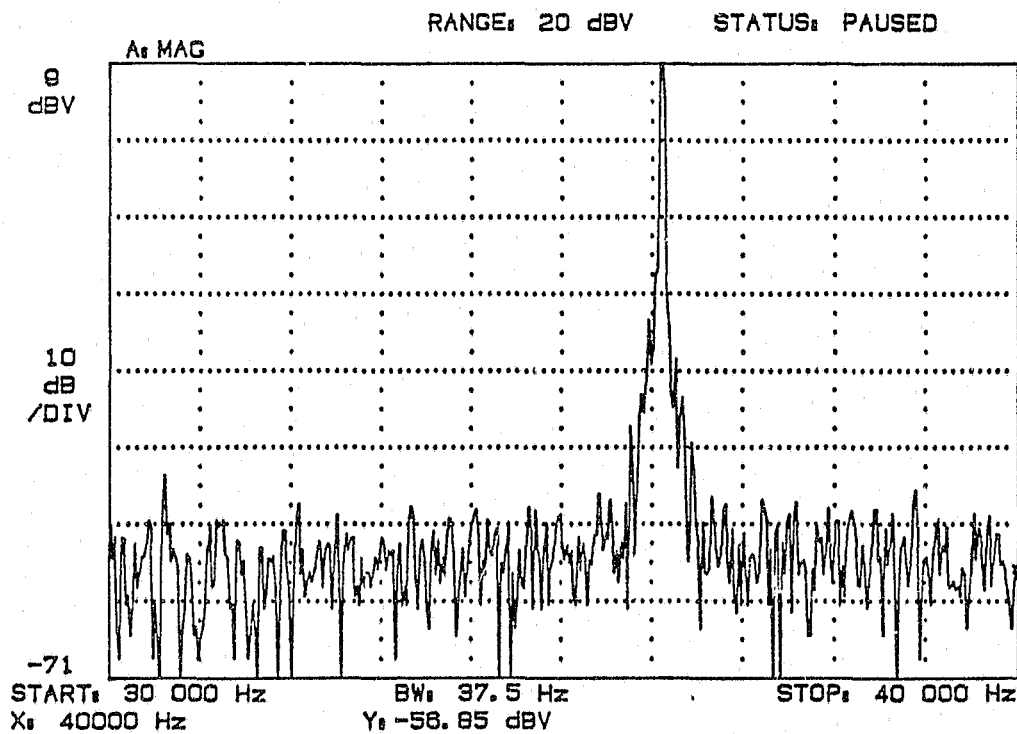
Fig. 2.10-8 Zoomed 30-40 kHz barrel spectrum for M-10 with .681 in barrel

116

A: MAG

0
dBV

10
dB
/DIV

-71
START: 30 000 Hz   BW: 37.5 Hz   STOP: 40 000 Hz
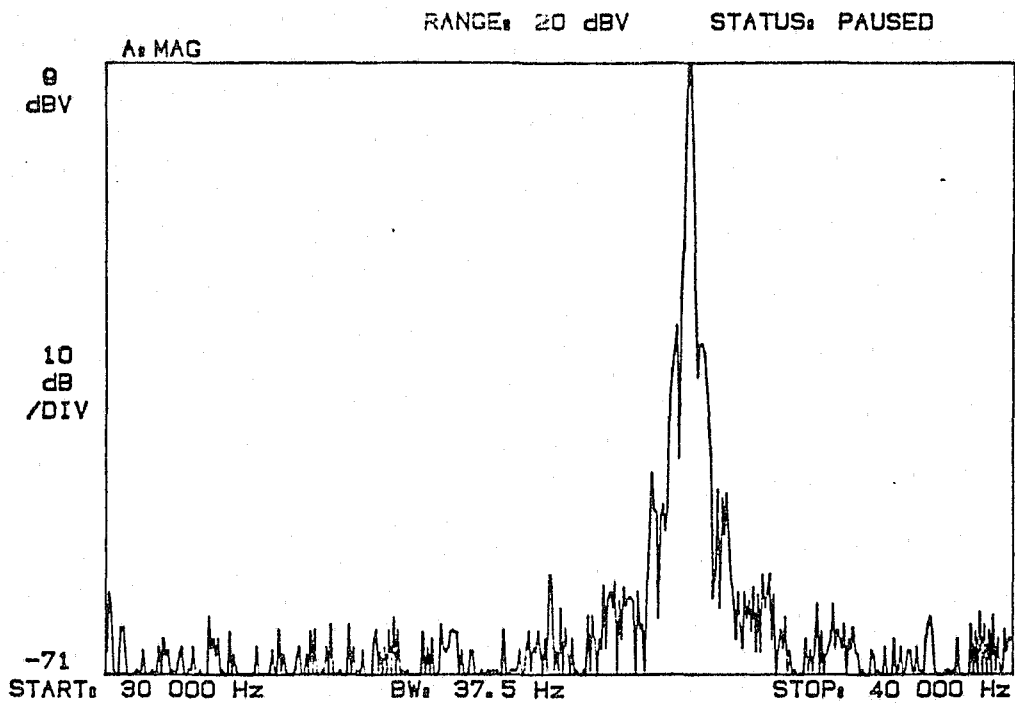
Fig. 2.10-9 Zoomed 30-40 kHz barrel spectrum for M-10 with .687 in barrel

A: MAG

0
dBV

10
dB
/DIV

-71
START: 30 000 Hz   BW: 37.5 Hz   STOP: 40 000 Hz
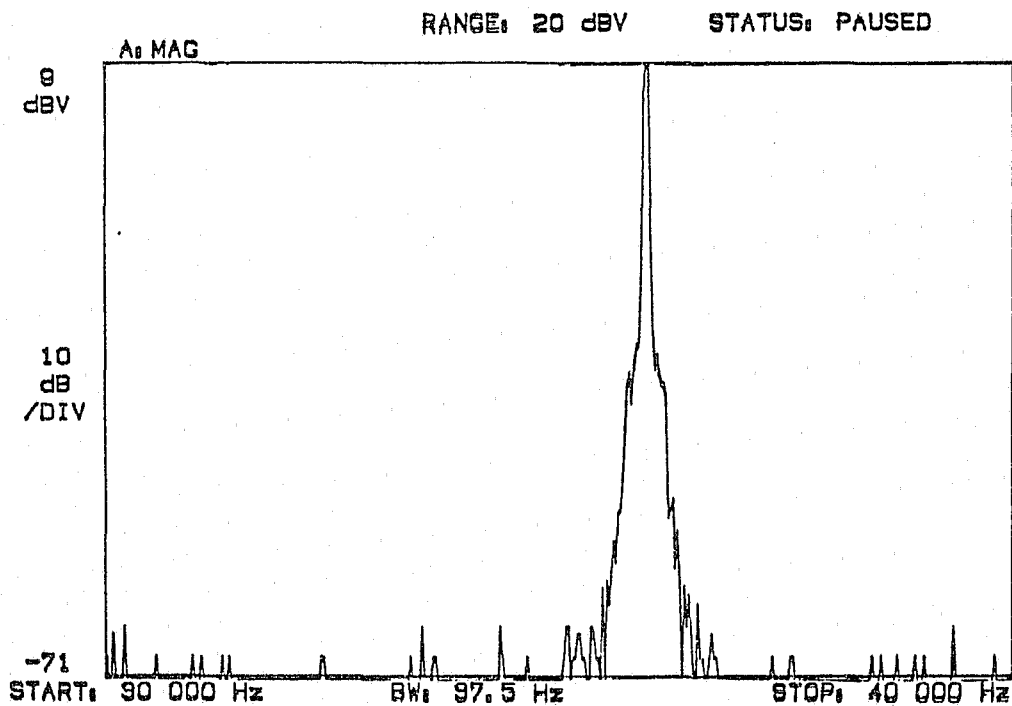
Fig. 2.10-10 Zoomed 30-40 kHz barrel spectrum for M-10 with .680 in barrel

RANGE: 20 dBV   STATUS: PAUSED

A: MAG

20 dBV

10 dB /DIV

-80

START: 0 Hz   BW: 375 Hz   STOP: 100 000 Hz
X: 41250 Hz   Y: 3.20 dBV
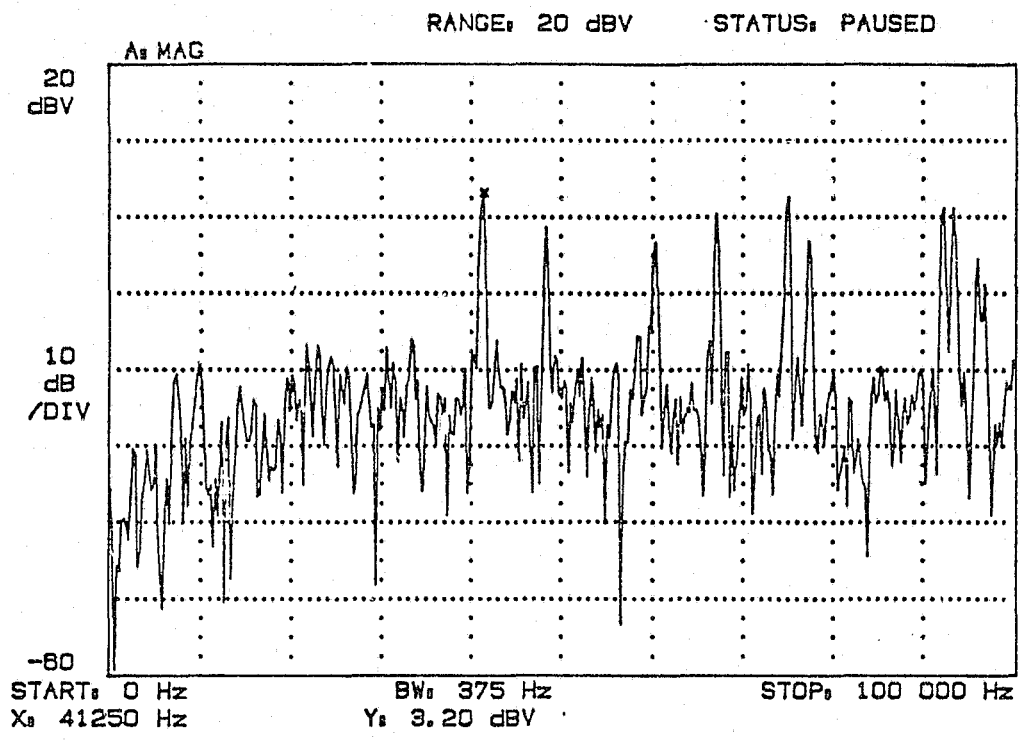
Fig. 2.10-11 Full 0-100 kHz knob spectrum for M-10 with .681 in barrel

RANGE: 20 dBV   STATUS: PAUSED

A: MAG

20 dBV

10 dB /DIV

-80

START: 0 Hz   BW: 375 Hz   STOP: 100 000 Hz
X: 41000 Hz   Y: 10.33 dBV
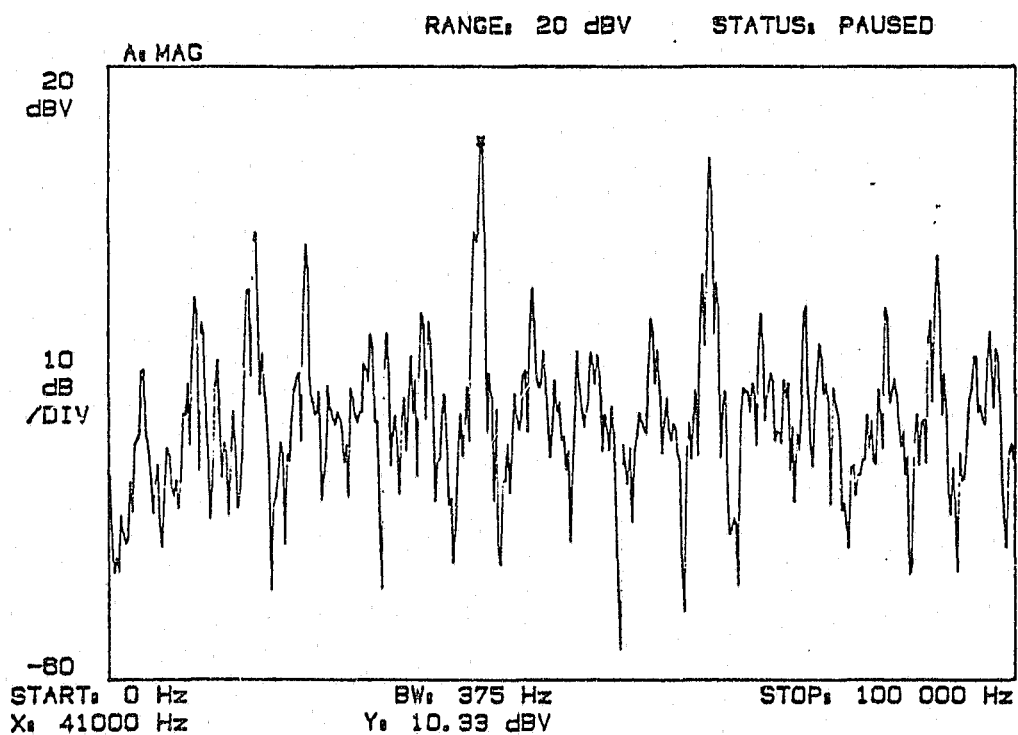
Fig. 2.10-12 Full 0-100 kHz knob spectrum for M-10 with .687 in barrel

RANGE: 20 dBV   STATUS: PAUSED

A: MAG

20
dBV

10
dB
/DIV

-80

START: 0 Hz   BW: 375 Hz   STOP: 100 000 Hz
X: 40250 Hz   Y: 13.02 dBV
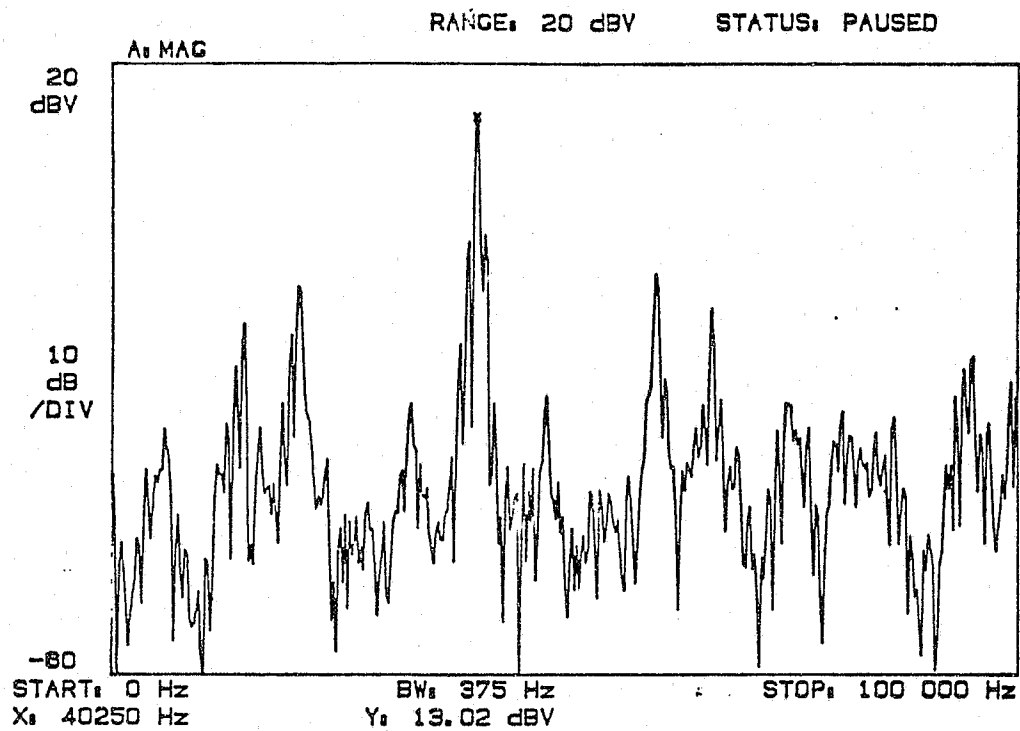
Fig. 2.10-13 Full 0-100 kHz knob spectrum for M-10 with .680 in barrel

RANGE: 20 dBV   STATUS: PAUSED

A: MAG

20
dBV

10
dB
/DIV

-80

START: 35 000 Hz   BW: 37.5 Hz   STOP: 45 000 Hz
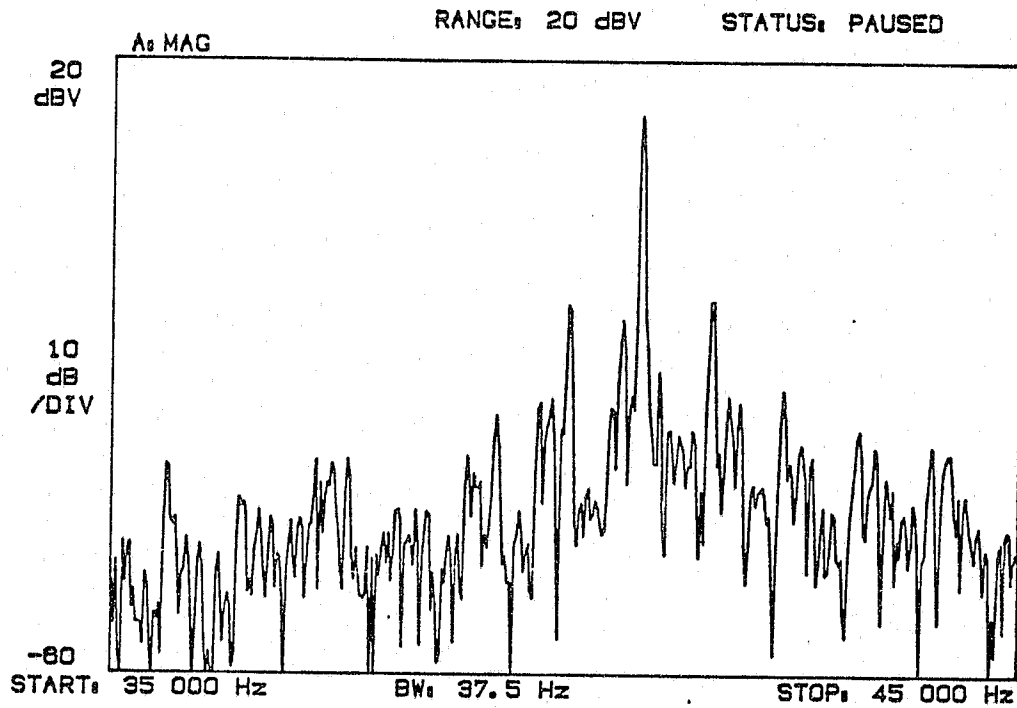
Fig. 2.10-14 Zoomed 35-45 kHz knob spectrum for M-10 with .681 in barrel

119
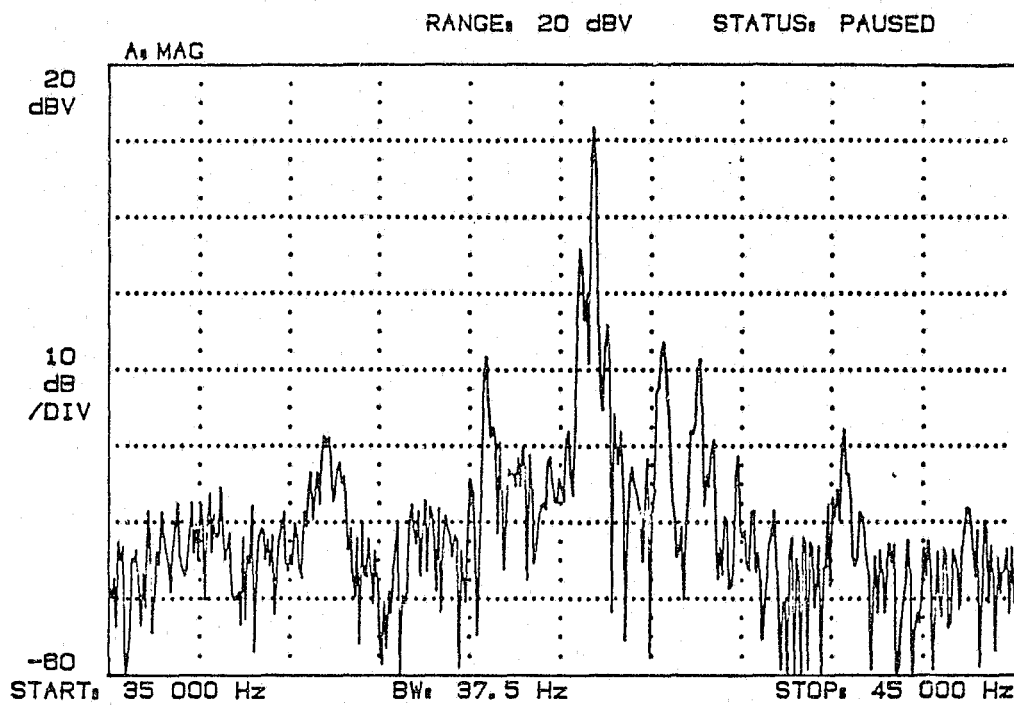
Fig. 2.10-15 Zoomed 35-45 kHz knob spectrum for M-10 with .687 in barrel
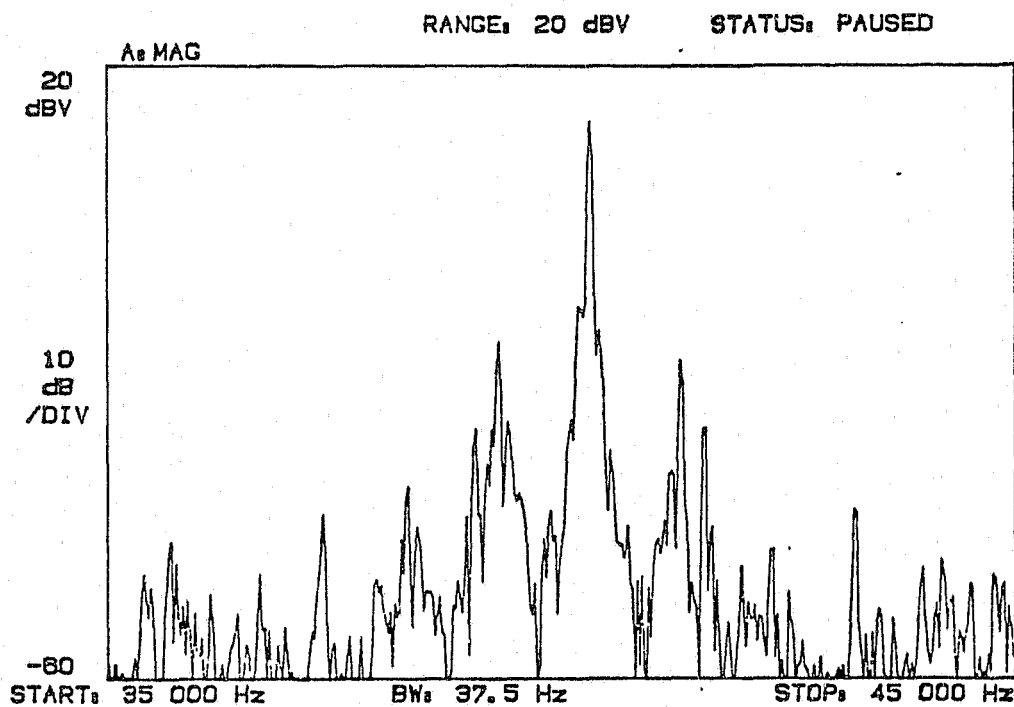
Fig. 2.10-16 Zoomed 35-45 kHz knob spectrum for M-10 with .680 in barrel

A: MAG   OVLD

10
dBV

10
dB
/DIV

-70
START: 0 Hz   BW: 375 Hz   STOP: 100 000 Hz
X: 65000 Hz   Y: -48.12 dBV
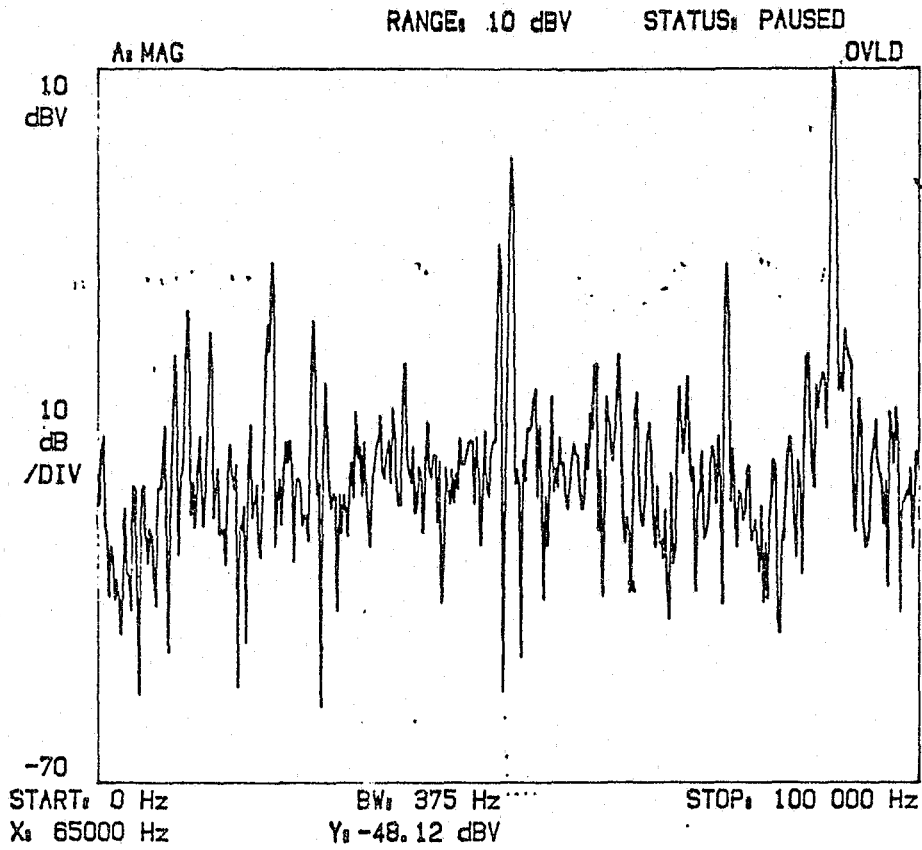
Fig. 2.10-17 Full 0-100 kHz spectrum of 1 in. dummy barrel

10
dBV

10
dB
/DIV

-70
START: 0 Hz   BW: 375 Hz   STOP: 100 000 Hz
X: 65000 Hz   Y: -26.16 dBV
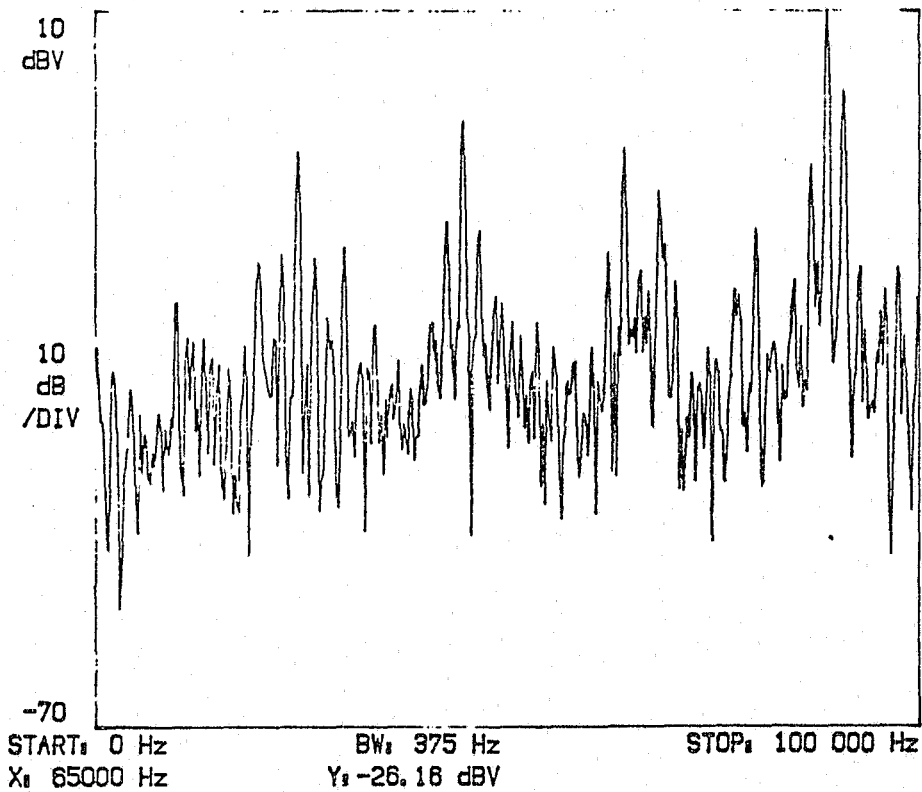
Fig. 2.10-18 Full 0-100 kHz spectrum of 2 in. dummy barrel

RANGE: 10 dBV   STATUS: PAUSED

A: MAG   OVLD

10
dBV

10
dB
/DIV

-70
START: 0 Hz   BW: 375 Hz   STOP: 100 000 Hz
X: 85000 Hz   Y: -21.86 dBV
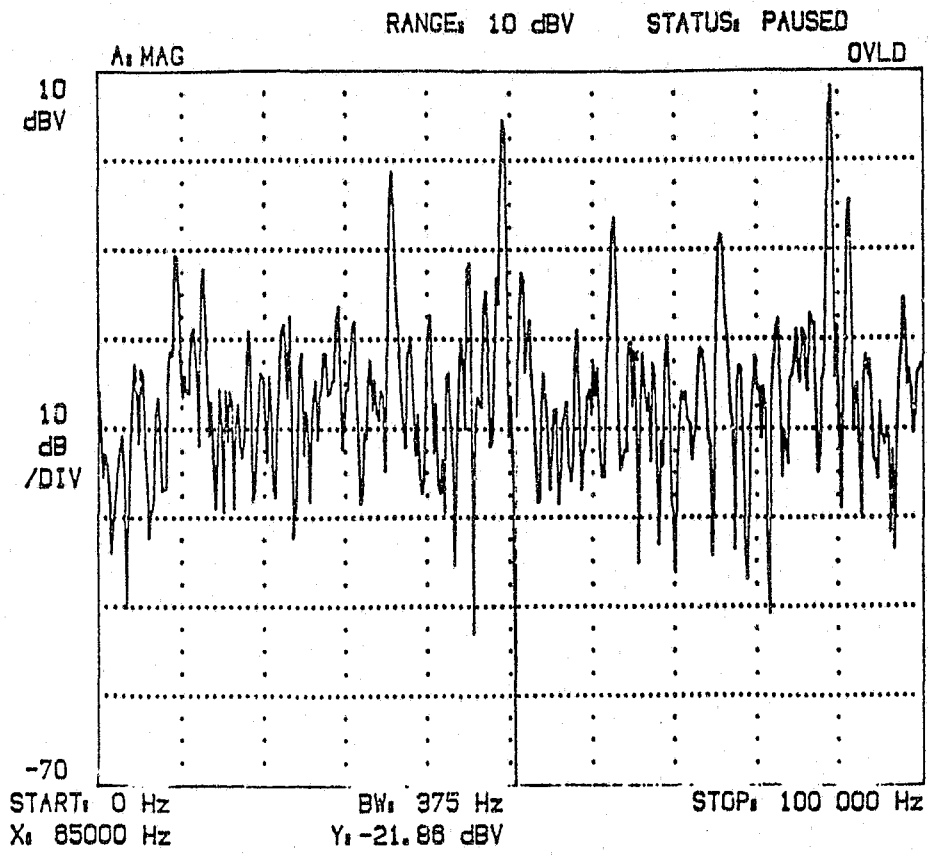
Fig. 2.10-19 Full 0-100 kHz spectrum of 3-3/8 in. dummy barrel

10
dBV

10
dB
/DIV

-70
START: 85 000 Hz   BW: 37.5 Hz   STOP: 85 000 Hz

B: TIME(R)   OVLD

8
Volt

2
Volt
/DIV

-8
START: 0 Sec   STOP: 40 mSec
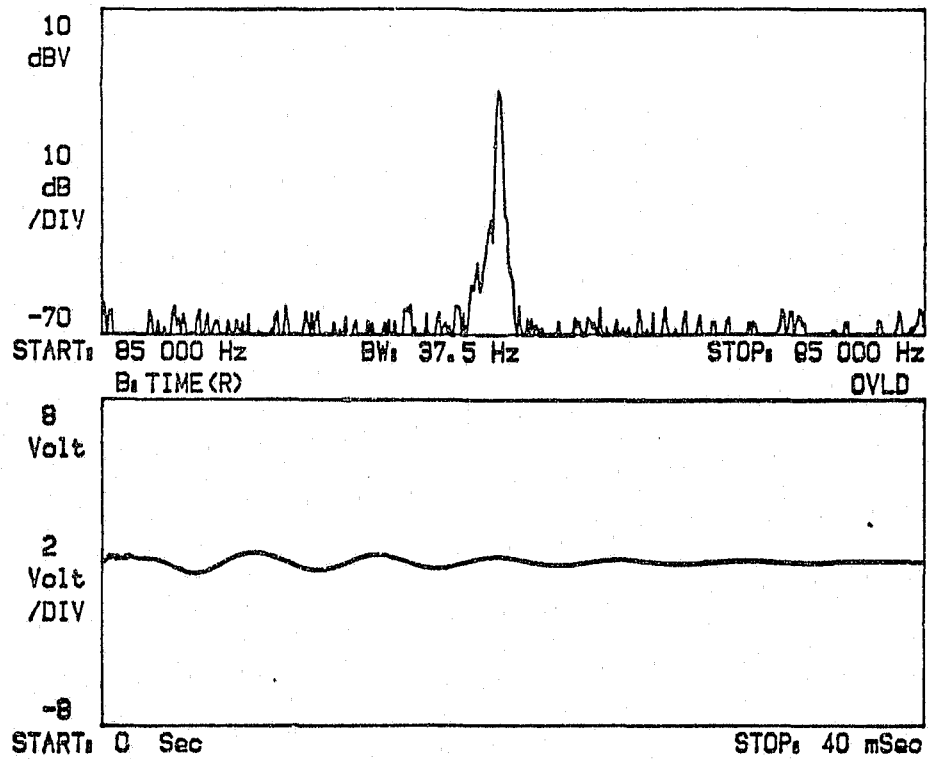
Fig. 2.10-20 Zoomed 85-95 kHz spectrum for dummy 1 in. barrel

RANGE: '10 dBV   STATUS: PAUSED

A: MAG   OVLD

10
dBV

10
dB
/DIV

-70
START: 85 000 Hz   BW: 37.5 Hz   STOP: 95 000 Hz

B: TIME(R)   OVLD

8
Volt

2
Volt
/DIV

-8
START: 0 Sec   STOP: 40 mSec
X: 89000 Hz   Y: 0.42 dBV
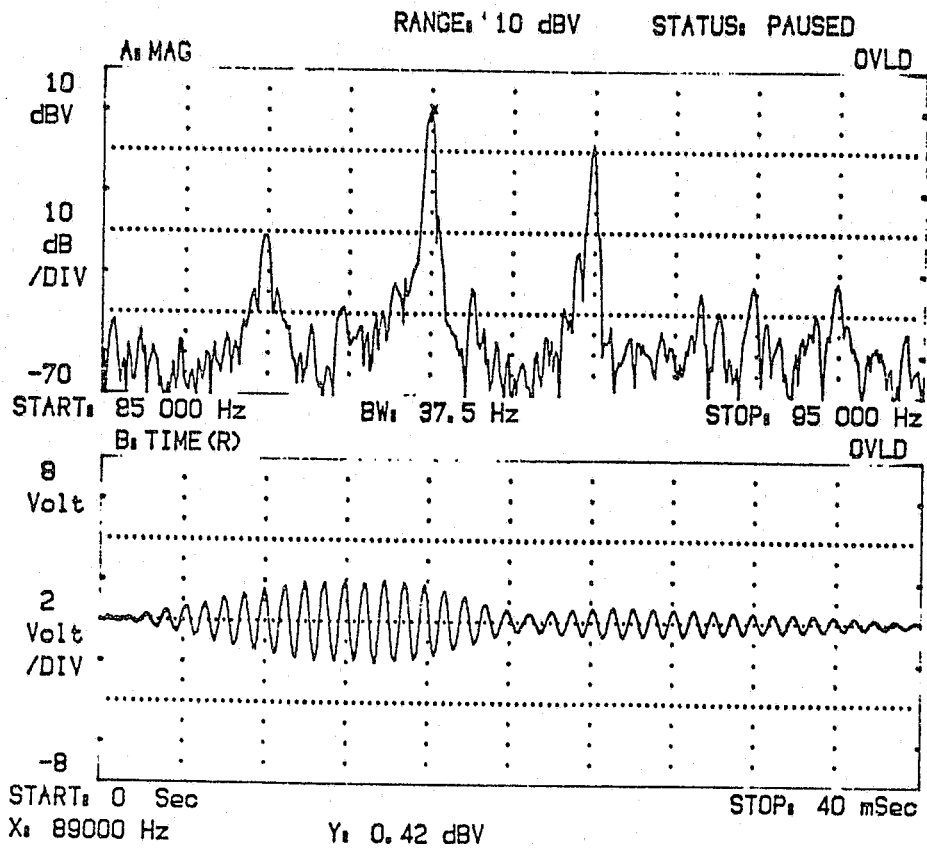
Fig. 2.10-21 Zoomed 85-95 kHz spectrum for 2 in. dummy barrel

RANGE: 10 dBV   STATUS: PAUSED

A: MAG   OVLD

10
dBV

10
dB
/DIV

-70
START: 85 000 Hz   BW: 37.5 Hz   STOP: 95 000 Hz

B: TIME(R)   OVLD

8
Volt

2
Volt
/DIV

-8
START: 0 Sec   STOP: 40 mSec
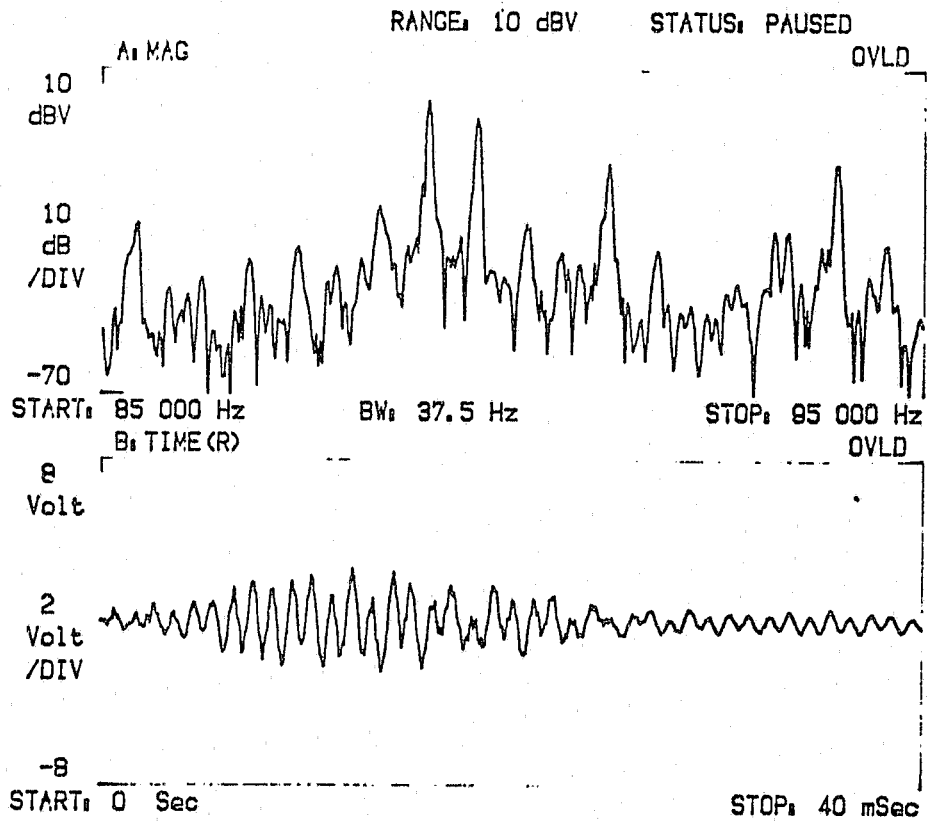
Fig. 2.10-22 Zoomed 85-95 kHz spectrum for dummy 3-3/8 in. barrel

123

Part 3 BIOHAZARDS OF AIRBORNE ULTRASOUND

Written By:

T. F. Moriarty[1]
R. E. Sotomayor[2]
J. R. Kennedy[3]
D. M. Lipscomb[4]

[1] Research Professor, Engineering Science and Mechanics Department, University of Tennessee, Knoxville
[2] Research Assistant Professor, Department of Zoology, University of Tennessee, Knoxville
[3] Professor, Department of Zoology, University of Tennessee, Knoxville
[4] Professor, Department of Audiology and Speech Pathology, University of Tennessee, Knoxville

124

3.0 <u>Biohazards of Airborne Ultrasound - Literature Search</u> (Moriarty)

To verify that the intensity, frequency range and waveforms of the transmitted ultrasound used by the Ultrasonic Handgun Detection System did not represent a biohazard to the system's developers and operators and to the general public an extensive literature search was begun on the biohazards of ultrasound in the Fall of 1985 and periodically updated thereafter. The resulting abstracts were reviewed by several investigators working on this project; key references were obtained and examined in detail. One result of this study was the selection and execution of the three animal models discussed in the following three chapters. Another result was the imposition of preliminary bounds on the intensity, frequency range and waveform of the transmitted ultrasound of the detection system.

The data bases searched were:

INSPEC	[IEEE AND IEE DATABASE]
PYSCINFO	[PSYCHOLOGICAL ABSTRACTS]
GPO	[U. S. GOVERNMENT PUBLICATIONS]
BIOSIS	[BIOLOGICAL ABSTRACTS]
NTIS	[NATIONAL TECHNICAL INFORMATION SERVICE]
EMBASE	[EXCERPTA MEDICA]
COMPENDEX	[ENGINEERING INDEX]
NIOSH	[NAT. INST. OCCUPATIONAL SAFETY & HEALTH]
MEDLINE	[INDEX MEDICUS]
HSELINE	[HEALTH & SAFETY]

The bulk of the references on the biohazards of ultrasound are concerned with <u>liquid</u> borne ultrasound used in diagnostic and therapeutic medical applications. Also the frequencies discussed in these references are often in the 1 MHz to 20 MHz range which are the frequencies used in typical pulse-echo diagnostic imaging. The handgun detection system currently uses frequencies in the 20 to 100 kHz range. The use of

higher frequencies by the detection system is presently not considered practical since the absorption of ultrasound in air increases for higher frequencies; this fact severely limits the range of the handgun detection system for frequencies much above 100 kHz. The mismatch of the delivery media and the frequency range of the majority of the ultrasound biohazards literature, on the one hand, and the Ultrasound Detection System, on the other hand, renders much of that literature not directly applicable.

A few references were found that discussed the biohazards of airborne ultrasound in the frequency range of interest. The National Council on Radiation Protection and Measurements Report No. 74 - Biological Effects of Ultrasound: Mechanisms and Clinical Implications, 1983, page 213 states that if an airborne ultrasound of intensity of 106 dB (re 1.0 (-12) W/m^2) were to propagate into the body the intensity of the ultrasound in the body would only be 77 dB. The 29 dB drop in intensity means that the intensity of the ultrasound in the body is only 1/800th that of the intensity of the ultrasound in the air; this drop in intensity is due to the mismatch of the characteristic acoustic impedance of the body versus air.

Further, they state, "Reports of fatigue, irritability and other symptoms experienced by workers near ultrasound-generating devices are often traceable to subharmonics or other audible sounds generated by the devices. The precautions advised are the same as for exposure to audible sound produced by other sources."

To avoid this latter problem altogether, the transmitter of the detection system will only use waveforms that emit no audible sound; such waveforms have no discontinuities in them to cause what radio engineers used to refer to as impulse noise (Radio Engineering Handbook, Keith Henney, Editor--in-Chief, 1959, page 19-17).

Another important reference on the biohazards of airborne ultrasound is: Environmental Health Criteria 22 - Ultrasound, by the World Health Organization, Geneva 1982 pages 115, 116. They state: "Since the ear is a sound-sensitive organ, much of the research conducted to date has been based on the likelihood that a physical

hazard resulting from airborne ultrasound will involve the ear and may result in a measurable effect on hearing sensitivity. Airborne sound or ultrasound is linked with the human body, through the ear, with an efficiency that is 2 or 3 orders of magnitude greater than that by any other route."

Further, "Studies of industrial workers exposed to levels of low-frequency ultrasound, at approximately 120 dB, failed to reveal either temporary or permanent hearing losses.... However, temporary threshold shifts were noted in the hearing activity of subjects... at subharmonics of discrete test frequencies in the range of 17-37 kHz... exposed [for] five minutes to 150 dB... It has long been assumed... that temporary threshold shifts is a necessary and sufficient condition (over an extended period of time) for permanent threshold shifts to occur."

The current detection system transmits ultrasound at about 120 dB. Clearly, the above observations place the maximum safe intensity somewhere between 120 dB and 150 dB. Further animal tests will be conducted to more closely determine the value of the maximum safe intensity. Future versions of the detection system will not transmit ultrasound above the maximum safe level.

The above comments related to the coupling of airborne ultrasound into the body through the ears has prompted us to shift the lower bound on transmitted frequencies from 20 kHz to 30 kHz to minimize such coupling of ultrasound into the body. The results of further animal model tests may prompt us to move this lower bound for transmitted frequency even higher.

3.1   Biological Effects of Airborne Ultrasound Exposure in Mice (Sotomayor)

This chapter describes the results of a preliminary study performed at the University of Tennessee, Knoxville, on the potential biological effects of airborne ultrasound in experimental animals. A review of the literature on liquidborne and airborne ultrasound revealed three possible areas of concern: (a) auditory effects; (b) cellular damage; (c) reproductive effects. This chapter is concerned with the reproductive effects.

In all the studies described below the mouse was used as the experimental animal model. The mouse has been the classical animal model for genetic toxicology studies. There is extensive information about the genetics, physiology, and structural aspects of mouse reproduction. Under the proper exposure conditions the mouse can be a useful experimental animal for studying the reproductive effects of ultrasound irradiation. The following aspects of male mouse reproduction were investigated. (1) Induction of DNA damage in early spermatid stages; (2) Induction of sperm head abnormalities; (3) Induction of chromosome aberrations (4) Loss of germ cells (germ-cell depletion) in the testis. Some of these endpoints were chosen because of previous published data indicating positive effects after in vitro or in vivo exposure to ultrasound. For instance, studies with Hela cells in vitro showed that administration of ultrasound at spacial averaged temporal averaged (SATA) intensities of $17 mW/cm^2$ and spacial peak temporal peak (SPTP) intensities of $34.5 W/cm^2$ induced unscheduled DNA synthesis (UDS), a manifestation of DNA damage and repair at the cellular level (Liebeskind et.al., 1979). Liquidborne ultrasound has been shown to induce chromosome aberrations in human lymphocytes in culture (Macintosh and Davey, 1970, 1972). However, other studies have failed to demonstrate chromosome aberration induction after in vivo or in vitro ultrasound exposures (see Stewart and Stratmeyer, 1982, for review). An important area of concern for our research project was the potential damaging effects of ultrasound on mammalian spermatogenesis. Fahim et.al. (1975) showed a marked depletion of

128

spermatogenic cells resulting in sterility in rats exposed to pulsed liquidborne ultrasound at doses of 1 or 2 W/cm^2 for 5 minutes. Similarly, Dumontier et.al. (1977) reported that rats exposed to 1W/cm^2 exhibited intense destruction of spermatocytes and spermtids after 5 to 10 minutes of exposure. O'Brien et.al. (1977) demonstrated that ultrasound is capable of markedly disrupting testicular tissue and specifically affecting spermatocytogenesis and spermiogenesis in mice. Although in all these studies ultrasound was administered in a liquid medium we thought it of importance to investigate similar effects after airborne ultrasound exposures.

Experimental Procedures

Exposure conditions:

Male mice, (C3H x B10) hybrids, about 6 months of age were used in these studies. The abdominal area including the testes were shaved before ultrasound exposure. The animals were lightly anesthesized with Metofane and plastic plugs were placed into their ears. The mice were then placed in small restrainers built in a circular plexiglass container (Fig. 3.1-1). The tails were firmly taped to the plastic and the animals were kept immobile during the exposures. In order to expose the testes only, a circular hole (1/2 inch in diameter) was made on the restrainer and the testicular area was positioned within the circular area. A maximum of 24 mice were exposed to airborne ultrasound at any given time. The container with the animals was then placed on top of a foam-insulated drum at exactly 1.5m from the ultrasonic transducer. Only the testes were directly exposed to ultrasound. Control mice were treated in the same manner but they were not exposed to ultrasound.
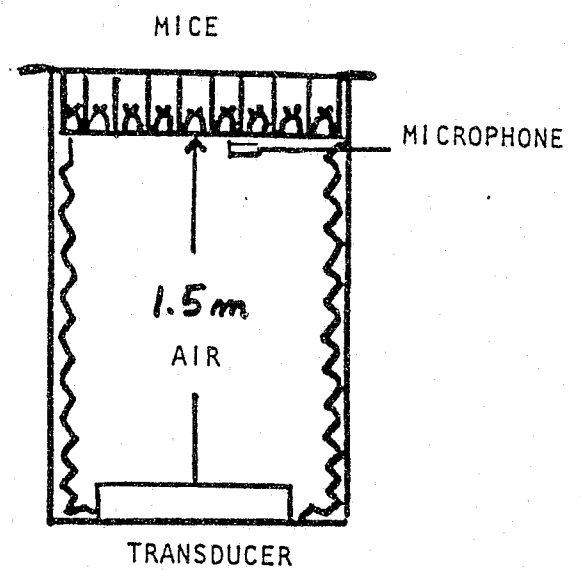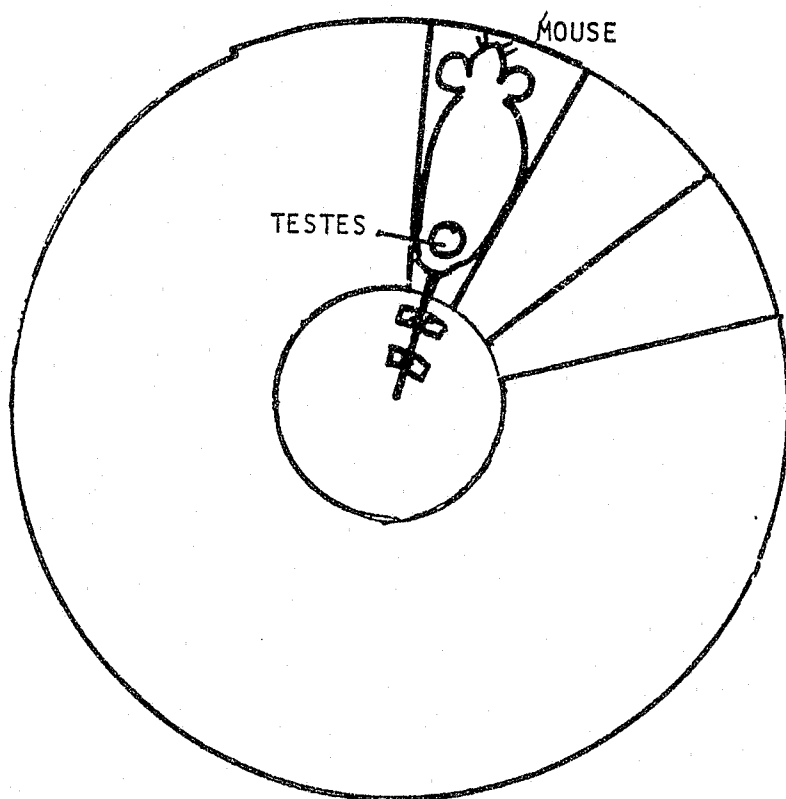
Fig. 3.1-1 Administration of ultrasound to the testes of mice. Ultrasound waves

emitted from a transducer located at the base of a foam-insulated

drum, 1.5m from the restrained animals.

<u>UDS experiments</u>:

Ten experimental and 10 control mice were used in this study. The animals were injected intratesticularly with 18 micro Ci per testis of (^{3}H)-thymidine of high specific activity. Immediately after, mice were exposed to 120± 2.0 dB* of ultrasound (maximum output) for 5 minutes. Control and treated mice were killed 17 days after the treatment and sperm from the <u>vas deferens</u> and <u>caudal epididymis</u> were collected. Sperm were then processed to obtain a purified sperm head suspension according to the procedure of Sega and Sotomayor (1982). The (^{3}H)-thymidine into the DNA of sperm nuclei (UDS) was expressed as disintegrations per minute per 10^6 sperm heads (dpm/10^6 sperm heads). If the DNA of any meiotic or postmeiotic germ-cell stage was damaged by the ultrasound treatment, a significant level of unscheduled DNA synthesis should be detected. This assay is known as the <u>in vivo</u> UDS assay in the germ cells of male mice (Sega and Sotomayor, 1982).

The results are shown in Fig. 3.1-2. The data is presented in a semilog plot. Each dot represents the level of UDS for a single mouse. It is clear from these results that the level of UDS in animals treated with ultrasound was not different from that of untreated controls. The level of UDS (average) induced by methyl-nitrosourea (MNU) is shown for comparative purposes. MNU is a powerful mutagen and carcinogen and the most potent inducer of UDS in mouse spermatids (Sega et.al., 1981). It can be concluded that airborne ultrasound at the exposure used did not induce DNA damage in early spermatid stages of mice.

*Temporal averaged intensity. The transmitted signal was a sine sweep from 45 kHz to 55 kHz in 0.1 sec with a 50% duty cycle. Peak intensity was 133 dB.
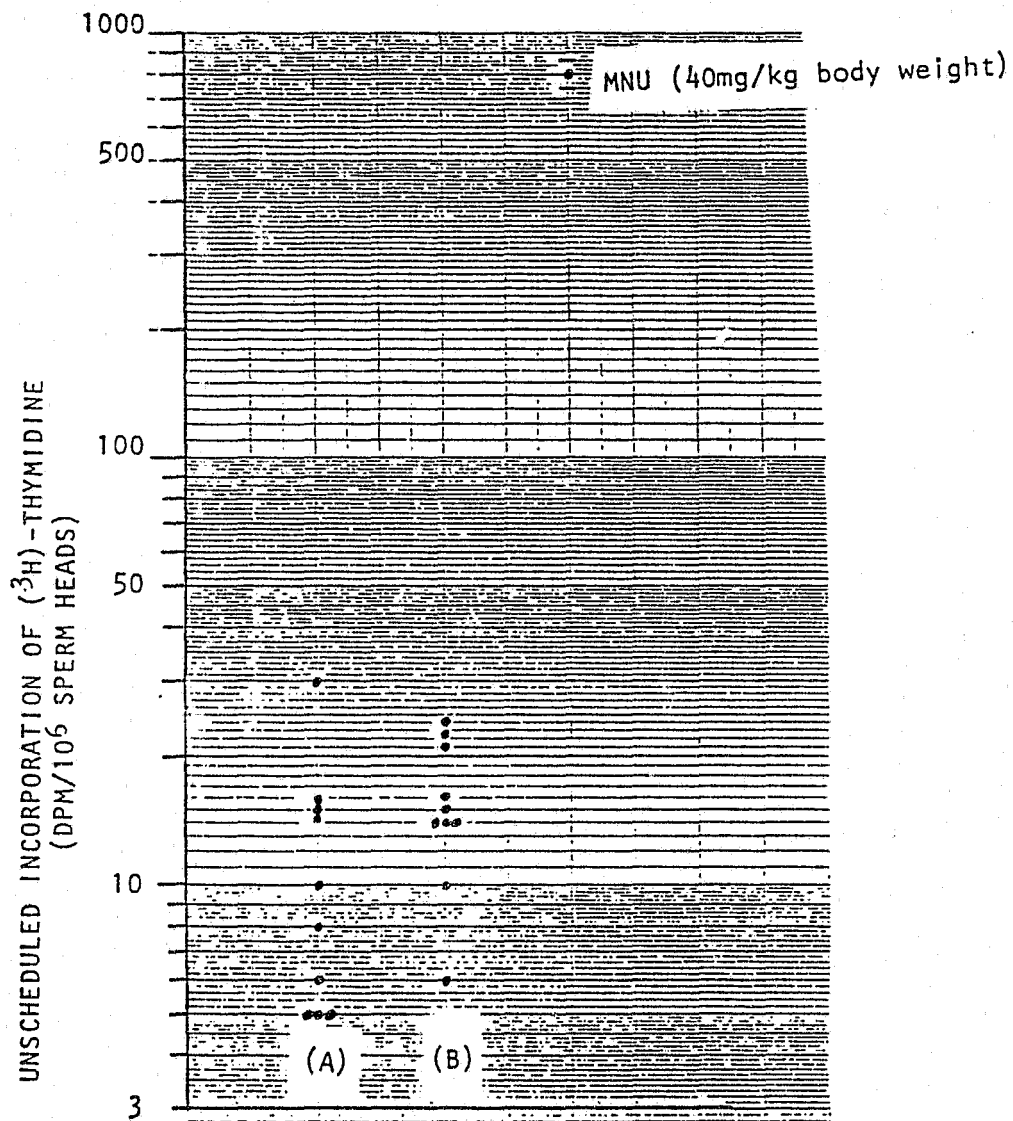
Fig. 3.1-2 Unscheduled DNA synthesis in early spermatide stages of mice after treatment with airborne ultrasound. (A) controls, (B) treated, MNU, methylnitrosourea, positive control.

132

Sperm head abnormalities:

Mice were exposed to 124± 2.0 dB of airborne ultrasound for five minutes during three consecutive days. One group of mice was killed one day after treatment. Another group was killed 22 days after the exposure. Sperm from the vas deferens were collected and suspended in phosphate buffered saline (PBS, pH 7.2). The sperm were fixed with formaldehyde (3% final concentration). Smears of the sperm suspension were prepared 2 hours after the fixation and the preparations were let dry for at least 24 hours before they were stained (Bryan, 1970). At least 1000 sperm per mouse were scored using a Zeiss microscope at 400 X. Five mice per treated and control groups were used in each case. The results are shown in Table 3.1-1. No significant differences between ultrasound exposed and control mice were found with regard to morphological sperm head abnormalities.

Chromosome aberrations:

Exposure conditions for this study were similar to those of the sperm abnormality study. Animals were killed 1 day and 22 days post-treatment, respectively. The testes were removed and processed according to the technique of Sotomayor and Cumming (1975). The preparations were scored for meiotic chromosomes at diakinesis. Spermatocytes at diakinesis in the animals killed 22 days after treatment were derived from germ cells that were in spermatogonial stages at the time of ultrasound treatment. The following types of chromosome aberrations were scored: X-Y univalency, autosomal univalency, chromosome fragments and translocations. The results are shown in Table 2. No signiicant differences between treated and control mice were detected.

Table 3.1-1 Incidence of Abnormal Sperm Heads in Mice Treated with Ultrasound and Killed 1 Day or 22 Days After Treatment. Classes of Abnormal Sperm: (a) Broad-Acrosomal Area, Spatulate Head; (b) Mitochondrial Blob; (c) Dislocated Head.

		PERCENTAGE					
		ABNORMAL			NORMAL	NUMBER SPERM SCORED	NUMBER OF MICE
		A	B	C			
1 DAY	TREATED	.3	1.4	.3	98.0	5000	5
	CONTROLS	.2	1.0	.5	98.3	5000	5
22 DAYS	TREATED						
			IN PROGRESS				
	CONTROLS						

Table 3.1-2 Induction of Chromosome Aberrations by Ultrasound in Meiotic Spermatocytes (1 Day After Treatment) and Spermatogonia (22 Days After Treatment). Chromosomes Were Scored in Diakinesis-Metaphase 1.

| | ULTRASOUND TREATED | | CONTROLS | |
| | TIME AFTER TREATMENT | | TIME AFTER SHAM TREATMENT | |
TYPE OF ABERRATION	1 DAY	22 DAYS	1 DAY	22 DAYS
X-Y UNIVALENCY (%)	5.7	7.0	6.0	9.0
AUTOSOMAL UNIVAL. (%)	1.9	2.0	2.0	3.0
FRAGMENTS (%)	0	0	0	0
TRANSLOCATIONS (%)	0	0	0	0
NUMBER OF CELLS SCORED	105	200	200	200
NUMBER OF MICE	4	4	4	4

134

Germ-cell depletion:

Ultrasound exposure conditions were similar to those previously described. Mice were killed 1 day and 22 days after the treatment. The testes were removed, weighed, fixed in Zenker-formol, embedded in paraffin, sectioned at 5 um, stained with periodic acid-Schiff (PAS) and counterstained with Ehrlich's hematoxylin (Leblond and Clermont, 1952). Cross-sections of seminiferous tubules were scored for gross depletion of germinal cells as manifested by disorganized and complete absence of germ cells in the tubules. No attempt to characterize depletion of specific germ-cell stages was made. In order to have additional indicators of germ-cell depletion, the perimeters and diameters of seminiferous tubules were determined by digitizing morphometry using a Bioquant II system with an Apple II microcomputer. The results are shown in Tables 3.1-3 and 3.1-4. Similar levels of germ-cell depletion were detected in treated and control testes. No reduction in the diameter of the seminiferous tubules or in the weight of the testis was observed in any of the animals tested (Table 3.1-4). The testis weights were corrected for differences in body weight and are expressed as the ratio of the testis weight/body weight x 100.

Conclusions

The present results indicate that under the experimental conditions used in these studies ultrasound did not produce any detrimental effect on mammalian spermatogenesis.

Work in Progress

Additional studies on the induction of sperm head abnormalities and germ cell depletion are in progress.

Table 3.1-3   Induction of Germ Cell Depletion by Ultrasound.   Diameters and
Perimeters of the Seminiferous Tubules are Also Shown.

	PERCENTAGE TUBULE CROSS-SECTIONS			NUMBER TUBULE CROSS-SECTIONS SCORED	TUBULE DIAMETER, um MEAN ± S.D.	TUBULE PERIMETER, um MEAN ± S.D.	NUMBER OF MICE
	NORMAL	DEPLETED	OTHER				
TREATED	98	1	1	613	107 ± 14	498 ± 35	5
1 DAY							
CONTROLS	97	1	2	380	108 ± 17	510 ± 47	4
TREATED	99	1	0	458	109 ± 17	508 ± 44	5
22 DAYS							
CONTROLS	100	0	0	457	110 ± 12	508 ± 29	5

Table 3.1-4   A Comparison of the Testis Weights in Ultrasound Treated and
Untreated Mice (Controls). The Testis Weights Were Corrected for
Body Weight Differences and Are Expressed as the Ratio Testis
Weight/Body Weight x 100. N = Number of Mice.

	TIME AFTER TREATMENT	
	1 DAY	22 DAYS
	MEAN ± S.D.	MEAN ± S.D.
TREATED	.364 ± .05	.295 ± .03
N	10	10
CONTROLS	.347 ± .07	.301 ± .03
N	8	9

136

References

1. Bryan, J. H. D. (1970). An eosin-fast green-naphtol yellow mixture for differential staining of the cytological components in mammalian spermatozoa. Stain Technol. <u>45</u>: 231-236.

2. Dumontier, A., A. Burdick, B. Ewigman, and M. S. Fahim, (1977). Effects of sonication on mature rat testes. Fertility and Sterility, <u>28</u>: 195-204.

3. Fahim. M. S., Z. Fahim, R. Der, D. G. Hall, and J. Harman, (1975). Heat in male contraception (hot water 60°C, infrared, microwave, and ultrasound). Contraception, <u>11</u>(5): 549-562.

4. Leblond, C. P. and Y. Clermont, (1952). Spermiogenesis of rat, mouse, hamster, and guinea pig as revealed by the "periodic acid-fuchsin sulfurous acid" technique. Am. J. Anat., <u>90</u>: 167-216.

5. Liebeskind, D., R. Bases, F. Elequin, S. Neubort, R. Leifer, R. Goldberg, and M. Koenisberg, (1979). Diagnostic ultrasound: effects on the DNA and growth patterns of animal cells. Radiology, <u>131</u>: 177-184.

6. Macintosh, I. J. C. and D. A. Davey, (1970). Chromosome aberrations induced by an ultrasonic fetal pulse detector. Brit. Med. J. <u>4</u>: 92-93.

7. Macintosh, I. J. C. and D. A. Davey, (1972). Relationship between intensity of ultrasound and induction of chromosome aberrations. Brit. J. Radiol., <u>45</u>: 320-327.

8. O'Brien, W. D. Jr., J. K. Brady, C. N. Graves, and F. Dunn, (1977). Preliminary report on morphological changes to mouse testicular tissue from <u>in vivo</u> ultrasonic irradiation. HEW Publication (FDA) 78-8048, pp. 182-191.

9. Sega, G. A., K. W. Wolfe, and J. G. Owens, (1981). A comparison of the molecular action of an S_N1-type methylating agent, methyl nitrosourea and an S_N2-type methylating agent, methyl methanesulfonate, in the germ cells of male mice. Chem. Biol. Interact., <u>33</u>: 253-269.

10. Sega, G. A., and R. E. Sotomayor, (1982). Unscheduled DNA synthesis in mammalian germ cells, - Its potential use in mutagenicity testing, in: F. J. de Serres and A. Hollaender (Eds.), Chemical Mutagens: Principles and Methods for their Detection, Vol. 7, Plenum Press, New York, pp. 421-445.

11. Sotomayor, R. E., and R. B. Cumming, (1975). Induction of translocations by cyclophosphamide in different germ-cell stages of male mice: cytological characterization and transmission. Mutation Res., <u>27</u>: 375-388.

12. Stewart, H. F., and M. E. Stratmeyer, (Eds.) (1982). An Overview of Ultrasound: Theory, Measurement, Medical Applications, and Biological Effects. HHS Publication (FDA) 82-8190 p. 1-134.

3.2 Effects of Airborne Ultrasound on the Function of Tracheal Cilia (Kennedy)

Introduction

Ciliated epithelium lines the tracheal connection from the mouth to the lungs. The role of this tissue is to trap particulate matter in mucus secreted from the goblet cells and move that material in a posterior-anterior direction from the lungs. In effect it is the primary defense mechanism for keeping foreign materials from depositing in the lungs. It is the responsibility of the ciliated cells to move the mucus and particulate matter away from the lungs. It is not likely that the ciliated cells of the trachea would normally be exposed to airborne ultrasound. However, these cells are sensitive to a variety of physiological conditions. Thus, by changing the cellular concentration of Calcium, ciliary frequency can be either increased or decreased. The ciliated cells are also sensitive to bacterial infection, viral infection or to a whole host of environmental pollutants. Thus, exposure to any of these agents has previously been shown to cause a reduction in ciliary frequency. The more toxic the agent the greater is the drop in frequency. Toxicity can be shown to be both concentration and time dependent. For these reasons ciliated cells were employed to test for the possibility of damage by airborne ultrasound at the cellular level. Ciliated cells in culture were exposed to airborne ultrasound and examined for change in ciliary frequency when compared with their control values.

Materials and Methods

Adult dog tracheal epithelium was cultured to produce ciliated outgrowths as previously described for rabbit trachea (Kennedy and Ranyard, 1983). Tracheas were removed from euthanised dogs from the cricoid cartilage to the bifurcation to the lungs. The tracheas were then cut into longitudinal strips and placed in Waymouths MB752/1 medium containing 100 units/ml penicillin and 100 microgm./ml streptomycin. Explants were grown in plastic culture dishes. Several explants were added to each dish and covered with Waymouths medium containing 10% NuSerum. Medium also contained 50

138

units/ml penicillin and 50 microgm./ml streptomycin. The explants were cultured in a water saturated 5% CO_2 in air atmosphere at 37C.

Ciliated outgrowth cells were exposed to airborne ultrasound as follows. Cultures were layered with 1.0 ml of culture media in 35mm diameter culture dishes and exposed to ultrasound with lids removed or with a modified lid to allow direct exposure of cells to ultrasound. Twelve cultures from two different dogs were exposed to ultrasound with exposure to 45-55 kHz sine sweep, 5 sweeps/sec, 50% duty cycle (122-140 dB peak intensity). Exposures were for 5 min intervals at either 25 or 37C. Two cultures were subjected to repeated exposure of 4 five minute intervals followed by 5 minute recovery periods. Cultures provided their own initial controls and were examined from immediately after exposure to 24 hours post exposure for change in frequency. Means (± standard error) were calculated for 10 cells from each exposure and recovery period.

Ciliary frequencies were measured using the method of Duckett et.al. (1986). A video camera was attached to the side tube of a Nikon phase-contrast inverted microscope. The phase image of the ciliated cells was then displayed on a television monitor where a series of individual cells could be viewed for analysis. Ciliary beat frequencies were quantitatively followed using an Oriel photomultiplier detection system (Kennedy and Duckett, 1981). The photomultiplier tube housing is fitted with an aperture that limits the light projected onto the sensor surface to only that light whose source is the area of video screen displaying a coherently beating tuft of cilia from a single cell. Physically, the lens on the photomultiplier housing is placed immediately before the area of cilia to be observed. Adjustment of photomultiplier current level provides the necessary sensitivity attenuation and ambient/dark current suppression. The photometric response is to produce an analog voltage signal proportional to the light level and with a frequency equal to that of the beating cilia. This analog signal is fed directly to the input of a spectrum analyzer. Spectral analysis provides a frequency characterization of ciliary beat. The analog signal, similar to that of a sinusoidal wave,

139

is converted by Fast Fourier transform (FFT) into a frequency spectrum with a Hewlett-Packard spectrum analyzer (Model 358A). From this transform the major ciliary frequency can be selected with an instrument output precision of 0.1 beats/sec.

Results

When individual ciliated cells are exposed to airborne ultrasound and their ciliary frequencies are monitored second by second, they show a frequency drop of between 0.5 and 1.0 Hertz. This drop in frequency begins immediately after the ultrasound is applied to the culture and persists, at the same level of frequency reduction, until exposure to ultrasound is terminated. If a particular exposure regime shows a 0.5 Hz drop, that drop in frequency remains at 0.5 Hz during the entire exposure period. No cells showed more than a 1.0 Hz decrease in frequency. Once ultrasound exposure was terminated, frequencies slowly returned to the control level over a 30 second to one minute time period. All cells analyzed recovered to normal frequency levels within one minute of termination of ultrasound. Intensity of exposure (dB peak intensity) did not affect the level of frequency drop.

When the means ($\pm$ SE) of ten cells in a culture are plotted against time, the 0.5-1.0 Hz frequency drop may disappear in the mean. In Fig. 3.2-1 the mean ($\pm$ SE) of 10 cells in each of four cultures are plotted. Values for controls immediately after removal from a CO_2 incubator and five minutes later are shown. During the first five minutes the untreated (control) cultures show a frequency drop of 0.3-1.3 Hz. (Table 3.2-1). This drop in frequency is no doubt related to a thermal drop in the culture even though the cultures were exposed in a thermal air curtain at 37C. At five minutes (Fig. 3.2-1, arrow) these cultures were exposed to ultrasound and frequencies recorded after two and five minutes exposure. In none of these cultures was the frequency drop after either two or five minutes exposure significantly different from the five minute control value.
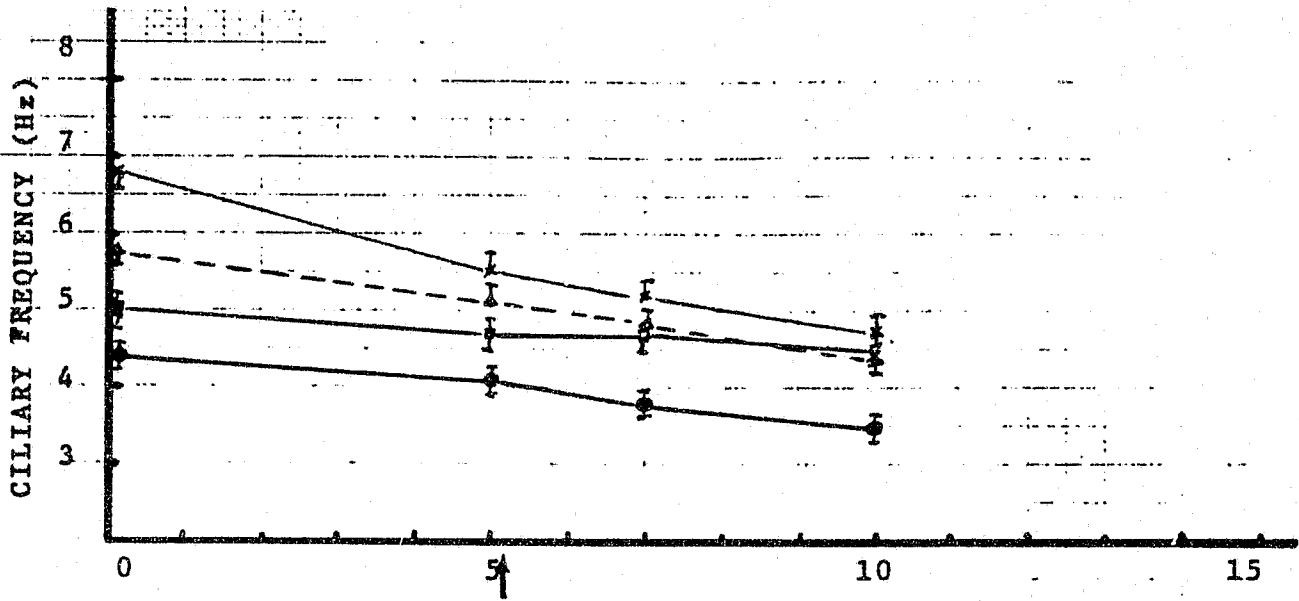
Fig. 3.2-1 A plot of ciliary frequency in hertz against time in minutes. Control
values at 0 and 5 minutes. The arrow indicates the time at which
ultrasound was applied to the cultures. Values at 7 and 10 minutes
represent 2 and 5 minutes after exposure to ultrasound.
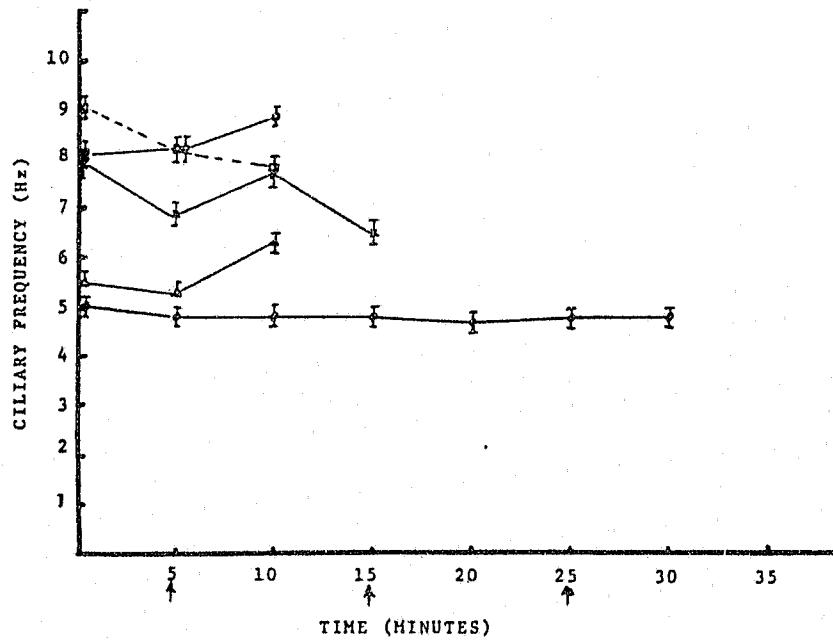
Fig. 3.2-2 A plot of values as in Fig. 3.2-1. Control value is at 0 minutes. Arrow
at 5 minutes indicates an ultrasound exposed value for all cultures.
Arrows at 15 and 25 minutes indicate ultrasound exposure for bottom
curve only. The 15 minute point in the curve designated (x) represents
a 10 minute recovery value.

Table 3.2-1 Ciliary Frequency versus Time

Frequency in Hertz (+/- standard error)

Control		Exposure		Recovery	
0 min.	5 min.	2 min.	5 min.	5 min.	10 min.
4.4 (0.1)	4.1 (0.1)	3.8 (0.1)	3.5 (0.1)		
5.0 (0.1)	4.7 (0.1)	4.7 (0.1)	4.5 (0.1)		
5.8 (0.1)	5.1 (0.1)	4.7 (0.1)	4.4 (0.1)		
6.8 (0.1)	5.5 (0.1)	5.2 (0.1)	4.7 (0.1)		
5.5 (0.1)			5.3 (0.1)	6.3 (0.1)	
7.9 (0.2)			6.9 (0.2)	7.7 (0.2)	6.5 (0.1)
9.0 (0.1)			8.2 (0.1)	7.7 (0.1)	
8.2 (0.1)			8.2 (0.1)	8.9 (0.1)	
5.0 (0.1)*			4.8 (0.1)*	4.8 (0.1)*	
			4.8 (0.1)*	4.7 (0.1)*	
			4.7 (0.1)*	4.8 (0.1)*	

* These values represent repeat exposures to the same culture.

In order to eliminate the problems associated with temperature drop during the first five minutes after removal of cultures from the CO_2 incubator, no control values were taken until temperature equilibration. Once equilibrated, control (0-min.) values were taken and the cultures were then exposed to airborne ultrasound. Exposure values were taken at five minutes followed by a five minute recovery. The results of this series of experiments is plotted in Fig. 3.2-2 and the values are shown in Table 3.2-1 (bottom). Of the five cultures plotted (Fig. 3.2-2) three showed no significant change in frequency after five minutes ultrasound exposure when compared with the control values. Two cultures showed a drop in frequency of up to 1.0 Hz and in one case the recovery period resulted in a return to control values. The other culture dropped in frequency during recovery but that decrease was not significantly different from the ultrasound exposure value. The remaining three cultures either increased above control values or remained the same after recovery. One culture (x) which was followed for 10 minutes post recovery returned to control values after five minutes but by 10 minutes post exposure had dropped to exposure values. The one culture which was subjected to a

repeated five minute exposure / five minute recovery regime (solid circles) showed no increase or decrease over the 30 minute treatment when compared to controls. Examination of cultures 24 and 48 hours after termination of treatment indicated no detrimental long term effect of airborne ultrasound on ciliary function.

Discussion

The exposure of ciliated cells in culture to airborne ultrasound appears to have no detrimental effect on cellular function. The 0.5-1.0 Hz decrease in frequency observed in individual cells during the exposure period does not persist beyond the exposure interval. Furthermore, it seems to have no permanent effect on the cells. The frequency drop may be the result of a slight temperature drop due to possible ultrasound induced surface evaporation. The 0.5-1.0 Hz shift disappears statistically when the mean ($\pm$ SE) of ten cells in a culture is calculated. The fluctuations up and down around the control values seen in Fig. 3.2-2 are not very great. The greatest fluctuation is no greater than 1.0 Hz. Kennedy and Ranyard (1983) have shown that some cells in culture fluctuate by as much as several Hertz. Many cultures on the other hand contain cells whose frequencies are very stable. If one analyzes a culture where a few cells are undergoing rapid fluctuation this can account for the increase or decrease seen in some cultures. Thus, since no specific pattern of consistent decrease or increase can be seen in cultures exposed to airborne ultrasound in the ranges employed we feel that the variation observed is due to random fluctuation in normal cell function and is not due to ultrasound. Furthermore, since no long term changes in frequency was observed, it is our opinion that airborne ultrasound has no effect on ciliated cells in culture at the levels employed in this study.

References

1. Duckett, K. E., Schiller, S. L., Girard, P. R., and Kennedy, J. R. (1986). The effects of gossypol on the ultrastructure and function of tracheal ciliated cells. J. Submicroscopic Cytology 18:117-125.

2. Kennedy, J. R. and Ranyard, J. R. (1983). Morphology and quantitation of ciliated outgrowths from cultured rabbit tracheal explants. European Journal of Cell Biology 29:200-208.

3. Kennedy, J. R. and Duckett, K. E. (1981). The study of ciliary frequencies with an optical spectrum analysis system. Experimental Cell Research 135:147-156.

3.3 Effect of Airborne Ultrasound on Chinchilla Ears (Lipscomb)

Male chinchillas (species - Laningera) were exposed to ultrasound to determine what ear damage, if any, could be caused by the ultrasound signals used for the detection of concealed handguns. Two animals have been tested to date.

The ultrasound exposure used was a sine sweep from 45 kHz to 55 kHz at a sweep rate of five per second at a duty cycle of 50 percent for a five minute duration. The temporal averaged intensity was measured to be 115 to 120 dB rms with 133 dB peak.

The left ears of the animals was blocked for control. The animals were terminated six weeks after exposure and a freehand half turn section was made on both ears to see the sensory cell condition. Five percent gluterialdehyde was used as a fix and 0.5% ozmiumtetroxide was used for a post fix/stain. For more detail on the techniques used, see: D. Lipscomb, *An Introduction to Laboratory Methods for the Study of the Ear*, Charles C. Thomas Publishers, Springfield, IL, 1974.

Only spontaneous cell damage was observed.

4.0 CONCLUSIONS AND RECOMMENDATIONS

Written By:

T. F. Moriarty[a]

4.0   Conclusions and Recommendations

[a] Research Professor, Engineering Science and Mechanics Department, University of Tennessee, Knoxville

4.0 Conclusions and Recommendations

In Phase II/2 of this research program:

- the design of the digital electronics of the Field Test Unit was shifted to an IBM AT compatible base,

- special digital-to-analog and analog-to-digital boards for the Field Test Unit were designed and their construction begun,

- alternate technologies for airborne ultrasound transmitters and receivers for the Field Test Unit were identified and their incorporation into the Detection System begun,

- a Demonstration Unit was designed and built which detected four Natural Frequencies among three known handguns, automatically, in less than one second,

- a literature search and studies with three animal models were made that showed that the ultrasound used by the Detection System does not represent a biohazard.

It is recommended that a Phase III effort be made which will complete the development of the Hallway Version of the Field Test Unit and start field testing the unit. To accomplish this:

- the construction of the digital-to-analog and analog-to-digital boards for the Field Test Unit must be completed,

- the implementation of the new technologies for an airborne ultrasound transmitter and receiver must be completed and incorporated into the Field Test Unit,

- an acoustic hallway must be designed and built to provide optimum detection space for the Field Test Unit,

147

- development testing of the Field Test Unit must be made with a dozen or more common revolvers and automatics, under a variety of clothing, so that an appropriate pattern recognition algorithm can be developed, and finally,

- further animal model tests must be run to determine if the intensity of the transmitted ultrasound can be raised without causing a biohazard.